Experimental Investigation of Plumes of Soluble Particles

Yutong Cui

SORBONNE UNIVERSITÉ

cnrs

ESPCI PARIS
EDUCATION SCIENCE INNOVATION

THÈSE DE DOCTORAT
DE SORBONNE UNIVERSITÉ

Spécialité : Physique

École doctorale nº564: Physique en Île-de-France

réalisée au laboratoire

Physique et Mécanique des Milieux Hétérogènes

sous la direction de Philippe Claudin

présentée par

Yutong CUI

pour obtenir le grade de :

DOCTEUR DE SORBONNE UNIVERSITÉ

Sujet de la thèse :

Étude expérimentale des panaches de particules solubles

soutenue le 19 décembre 2022

devant le jury composé de :

M.	Philippe CLAUDIN	Directeur de thèse
M.	Benoît SEMIN	Co-directeur de thèse
M.	Sylvain JOUBAUD	Rapporteur
M.	Christophe RAUFASTE	Rapporteur
M.	Thomas SÉON	Examinateur
Mme	Anne DAVAILLE	Examinatrice
M.	Édouard KAMINSKI	Président de jury

Yutong CUI **19 décembre 2022**

Sujet : Étude expérimentale des panaches de particules solubles

Résumé : Nous avons étudié la sédimentation d'une suspension de particules solides solubles à partir d'un point localisé en haut d'un réservoir d'eau. Ces expériences sont partiellement analogues à la pluie localisée, où, dans l'air, les gouttelettes d'eau s'évaporent en tombant. Le cas des panaches générés par un fluide homogène lourd fournit une situation de référence bien étudiée, pour laquelle les profils transversaux de concentration et de vitesse montrent typiquement une forme gaussienne, avec une largeur augmentant linéairement avec la distance à la source. Dans ce travail, nous étudions le cas de panaches composés de particules constituées de produits chimiques solubles. Si le réservoir est rempli d'eau non saturée, les particules injectées se dissolvent progressivement au cours de leur sédimentation, ce qui affecte les caractéristiques du panache. Nous mesurons la concentration des particules par absorption de lumière, et les champs de vitesse au moyen de la PIV, ce qui nous permet d'estimer la vitesse d'entraînement en fonction du taux d'injection des particules. La forme des panaches, définie à partir des champs de concentration et de vitesse, est également discutée. Pour évaluer l'effet de la solubilité, nous comparons deux types de particules de densité similaire : des billes de plastique (polystyrène), qui ne sont pas solubles, et des particules de butyramide, qui sont très solubles dans l'eau. Ce dernier produit chimique a également été choisi parce qu'il ne modifie pas la densité de la solution aqueuse lorsqu'il se dissout, de sorte que les effets de flottabilité ne sont dus qu'aux particules solides. Nous avons montré que la forme du panache dépend fortement de la solubilité des particules, et que la vitesse d'entraînement des particules solubles varie pour différentes propriétés des particules.

Mots clés : pluie, panache, butyramide, gouttelette, sédimentation des particules

Subject : Experimental investigation of plumes of soluble particles

Abstract: We have investigated the sedimentation of a suspension of soluble solid particles from a localized point at the top of a water tank. These experiments are partially analog with a localized rain, where, in the air, water droplets evaporate while falling down. The case of plumes generated by heavy homogeneous fluid provides a well-studied reference situation, for which concentration and velocity transverse profiles typically show a Gaussian shape, with a width increasing linearly with the distance to the source. In this work, we study the case of plumes composed of particles consisting of soluble chemicals. If the tank is filled with non-saturated water, the injected particles progressively dissolve on the course of their sedimentation, which affects the plume characteristics. We measure the particle concentration by light absorption, and velocity fields by means of PIV, allowing us to estimate the entrainment velocity as a function of the particle injection rate. The shape of the plumes, defined from the concentration and velocity fields, is also discussed. To assess the effect of solubility, we compare two types of particles of similar densities: plastic (polystyrene) beads, which are not soluble, and butyramide particles, which are highly soluble in water. The latter chemical has been also chosen because it does not change the density of the aqueous solution when it dissolves in it, so that buoyancy effects only occur due to solid particles. We have shown that the shape of the plume highly depends on the solubility of the particles, and that the entrainment velocity of soluble particles varies for different particle properties.

Keywords : rain, plume, butyramide, droplet, particle sedimentation

Acknowledgements

I would like to express my deepest gratitude to my supervisors, Philippe Claudin and Benoît Semin, for their invaluable guidance, encouragement, and support throughout my research. Their insightful feedback and constructive criticism have been instrumental in shaping the direction and quality of this work.

I would also like to thank the members of my thesis committee, Sylvain Joubaud, Christophe Raufaste, Anne Davaille, Édouard Kaminski, Thomas Séon, for their time and efforts in reviewing my work and providing valuable feedback and suggestions. Their deep knowledge of analogue experiments and plume dynamics, as well as their intellectual rigor and attention to detail, have challenged me to think more deeply and to produce work of the highest quality.

I am grateful to the staff and faculty at PMMH, who have provided a stimulating and supportive academic environment that has helped me develop my research skills and intellectual curiosity. I am especially grateful to the engineers who have provided technical support throughout my research, Xavier, Thierry, and Amaury. Also, I would like to thank the directors and secretaries of the lab, Damien, Philippe, Frédérique, and Claudette. Without them, I cannot handle the complicated administrative issues in France.

I would like to extend my appreciation to my parents and my friends, who have provided emotional support and encouragement during the ups and downs of my research journey. Their belief in me and my abilities has been a source of inspiration and motivation. Because of Covid, I did not see my parents for more than three years. I long for their understanding and feel my guilt.

With my friends, we explored plenty of restaurants and landscapes in Paris and other European cities.

I express my deepest gratitude to my girlfriend, Shuyang, for her unwavering love and support throughout my research journey. She has been a constant source of encouragement, understanding, and inspiration, and she has always believed in me, even when I doubted myself. Her patience, kindness, and generosity have been a blessing, and I am so grateful to have her in my life. I look forward to all the adventures that lie ahead, and I am grateful to have you by my side.

Thank you all for your support and encouragement. This thesis would not have been possible without you.

Contents

List of Figures

List of Tables

1 Introduction

1.1 Climate change context

Each of us lives in our own body, but everyone lives on the same Earth. As a unique system that interacts with human beings and all living creatures, the Earth is crucial. The scale of recent changes across the climate system are unprecedented over the past centuries and thousands of years (Arias et al., 2021). Specifically, the global surface temperature has increased faster since 1970 than in any other 50-year period over at least the last 2000 years (Figure 1.1).

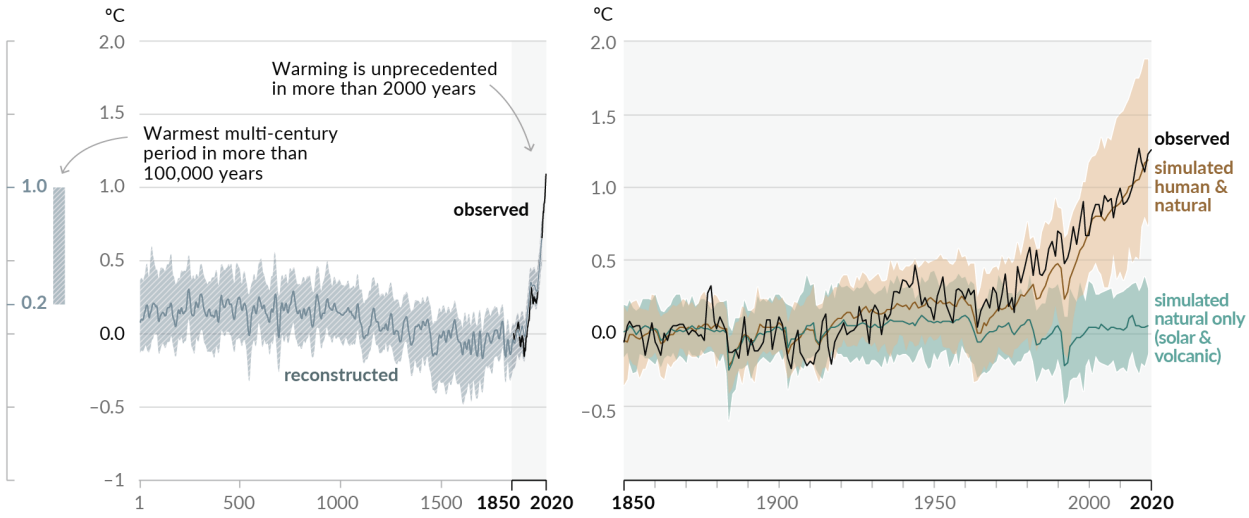

Figure 1.1: Changes in global surface temperature relative to 1850-1900 (Arias et al., 2021). (a) Change in global surface temperature (decadal average) as reconstructed (1-2000, grey) and observed (1850-2020, black); (b) Change in global surface temperature (annual average) as observed (black) and simulated using human & natural (earthy yellow) and only nature factors (light sea green), both from 1850 to 2020).

Human-induced climate change has affected many regions across the globe. It has resulted in an increased frequency and intensity of climate extremes, including temperature extremes (Buttlar et al., 2018), heavy precipitation and fluvial floods (Li et al., 2019, Lopez-Cantu, Prein, and Samaras, 2020), droughts (West, Quinn, and Horswell, 2019), hurricanes (Hosannah et al., 2019), and many more. As a result, the living and working environments of millions of people (Yu et al., 2019) are impacted, and a huge number of casualties (Mitchell et al., 2016) and economic losses were reported (Frame et al., 2020).

Stevens and Bony, 2013 indicated that the Earth's climate and its propensity to change is rooted in the interplay between water, air circulation, temperature, and greenhouse gases. Several generations of scientists worked on the modeling of the climate system. Some 1D models by the pioneers have good estimations of the temperature change with the CO_2 concentration. For simplicity, in the model by Manabe and Wetherald, 1967, the effect of clouds is only taken into account by a fixed albedo. This simplicity at that time might be due to the limitation of measurements or calculation capabilities, but after 50 years, many fundamental puzzles of climate science remain unsolved because of our limited understanding of how clouds, circulation, and climate interact (Schiermeier, 2015, Stevens and Bony, 2013).

1.2 Cloud and rain

With the rising of interdisciplinary research on climate (Weart, 2013), different kinds of cloud modeling thrive. The importance of lower clouds has appeared. Lower clouds are a leading cause of uncertainty in future climate prediction because even small changes in cloud coverage and thickness have a major impact on the radiation budget (Wood, 2012). The feedback of lower clouds is considered to act againist global warming (Brient and Bony, 2013, Zelinka, Randall, et al., 2017, Needham and Randall, 2021). On the other hand, some observations provided more evidence for the positive feedback of lower clouds to the climate system (Clement, Burgman, and Joel R Norris,

2009, Joel R. Norris et al., 2016). Moreover, with the development of computational fluid dynamics, the lower clouds feed-backs are quantified with simulation methods (Muller et al., 2021), such as large eddy simulations (Rieck, Nuijens, and Stevens, 2012, Bretherton and Blossey, 2014). In all, the efforts above aim to solve this important question in climate science: to predict the role of clouds in a warming world and to test whether those changes will amplify or partially offset the warming due to increased greenhouse gases and human activities (Hartmann and Larson, 2002, Brient and Bony, 2013, Zhao, 2014). For the comprehensive consideration, the global cloud feedback is likely positive to equilibrium climate warming (Zelinka, Randall, et al., 2017), but there are still uncertainties in the quantification of the effect (Arias et al., 2021).

More specifically, the overall cloud feedback loop is commonly separated into three components: cloud amount, cloud altitude, and cloud opacity feedback (Zelinka, Grise, et al., 2018). For a cloud, near the cloud boundaries, meter- and submeter-scale phenomena regulate cloud entrainment rates, which further control the cloud lifetimes and the evolution of cloud systems (Mellado, 2017). The submeter-scale phenomenas challenge the traditional measurement approach. Some interesting but limited measurements have been done (Siebert et al., 2015) to measure the turbulence properties in a cloud at a mountain station. Beals et al., 2015 used airborne holographic imaging to visualize the spatial structure and droplet size distribution. These measurements are time-consuming and the data collected may not represent the cloud size.

The precipitation investigation from meteorologists is usually focused on weather forecasts (Hosannah et al., 2019, Lopez-Cantu, Prein, and Samaras, 2020). There is a strong coupling between clouds' lifetime and rain rate (Smalley and Rapp, 2021). Based on the causes of formation, the types of rain can be divided into frontal rain with melting band, thunderstorm, and coalescence shower (Mason and Andrews, 1960). The frontal rain and thunderstorm are due to the interaction between cold air & warm moist air, and droplets & thunder, which mechanism of rain is relatively clear. For coalescence shower (Figure 1.2), it occurs within self-limiting isolate clouds. The conversion process of cloud water to rainwater tends to be influenced by aerosols (K.

Figure 1.2: Rain showers on the sea (local heavy rain), Eunsuk Hwang filmed at Saipan Island, August 19, 2011.

Suzuki, Stephens, and Lebsock, 2013). This localized raining process looks similar to a downward two-phase plume.

1.3 Analogue experiments

There are several approaches to investigating the climate system. The most traditional one is observation. Climate models are partially derived from the generalization of previous observations. Observations are time-consuming and limited to the condition of the current atmosphere with limited insight into the past atmosphere.

With the development of computer science, numerical simulations have become a powerful tool for weather forecasts, climate attribution, etc. Of course, simulations cannot resolve phenomena at all relevant scales, which span from the droplet size to the planetary scale, and parametrization of some processes must be included.

Developing analogue experiments is another useful approach in many areas, especially when the typical sizes of the research objects are much larger than the lab scale. With ingenious design of experimental setups, some main features or processes can be mimicked at the lab scale. There are many analogue experiments for geology investigation, such as the sand ripple and dune (Charru, Andreotti, and Claudin, 2013), the lower mantle on Earth (Fourel et al., 2017), internal gravity waves (Semin et al., 2018), the reversals of the Earth magnetic field (Berhanu et al., 2007), tornado-like plumes (Sutherland et al., 2021), etc.

In the context of atmospheric sciences, there are also several analogue experiments about cloud and rain processes. Sayler and Breidenthal, 1998 investigated the mixing at the top of stratocumulus clouds (typical clouds above ocean) with two aqueous solutions of different densities, and different colors, allowing for heat absorption at their interface by light illumination. Narasimha et al., 2011 heated a thermal water plume with several resistors to mimic the heating in the bulk of cumulus clouds due to the phase change of water. By adjusting the heating time and order, they could observe different shapes of 'clouds'. The injection of a negatively buoyant jet in a miscible surrounding liquid refers to the motion of plumes and clouds in the atmosphere (Philippe et al., 2005).

1.4 Jet and plume

Turbulent jets are fluid flows produced by a pressure drop through an orifice. Turbulent plumes are fluid motions whose primary source of kinetic energy and momentum flux are the body forces derived from density inhomogeneities (Fischer et al., 1979). For buoyancy-driven plumes, B R Morton et al., 1956 provided a general framework to calculate their general scaling behaviors with a simple entrainment assumption. This framework has been adjusted and developed by many others, and more details about theory works are discussed in Chapter 4.

The concepts about plumes are simple and have plenty of applications in both industry and

nature (G. R. Hunt and H. C. Burridge, 2015). The plume is observed in tomographic images of mantle upwellings (Davaille and Vatteville, 2005). Some ocean sprays are similar to jets and plumes, which exchange between the ocean and atmosphere by transporting water, heat, dissolved gases, salts, surfactants, and biological materials (Deike et al., 2018). Plumes have been investigated with different approaches, such as modeling (Carazzo, Kaminski, and Tait, 2008), experiments (Dai, Tseng, and Faeth, 1994, Ezzamel, Salizzoni, and G. R. Hunt, 2015), numerical simulations (Bhaganagar and Bhimireddy, 2020), and many more. For experiments, salty water is used as the usual source of buoyancy, with fluorescence dye to show the plume shape (H. Burridge, Partridge, and Linden, 2016). Refractive-index-matched PIV is used to measure the velocity field (Richardson and Gary R. Hunt, 2022). The volume of fluid (VOF) methods (Dutta et al., 2014), and large eddy simulations Y. J. Suzuki, 2005 are used for compressible plumes. For buoyancy plumes, a key concept is the entrainment coefficient α (a proportionality constant relating the inflow velocity at the edge of the flow to the middle-line vertical velocity) which has been measured in many works, but with large uncertainty. Recently, Richardson and Gary R. Hunt, 2022 investigated this uncertainty issue on the entrainment coefficient α, which indicated $0.095 < \alpha < 0.130$.

Besides one-phase buoyancy plumes, plumes using suspensions of particles as buoyancy source has been investigated in recent years (Bordoloi et al., 2020). McConnochie, Cenedese, and McElwaine, 2021 defined particle-laden plumes, where both the suspended particles and the bulk play a role in the buoyancy (if only the particles play a role, it is called particle plume). In order to build an experimental analogure of rain, we are specifically interested in particle plumes, which is discussed in Section 5.2. Furthermore, to mimic droplet evaporation during their falling, we also used salt as particle. The salt dissolves while sedimenting, which changes the dynamic behaviors of the plume.

1.5 Thesis outline

In this thesis, I would like to present some investigations of plumes of soluble particles and understand how dissolution changes the entrainment process. A special chemical, butyramide is used. The density of butyramide saturated solution is close to the one of water, which means that butyramide particles do not change much the density of the surrounding solution after dissolving. We performed experiments where butyramide is injected at the top of a water tank, and then dissolves partially, to mimic a 'rain' in the laboratory.

In Chapter 2, we present the experimental setup we have built to catch the dissolving process of a single butyramide particle during its falling. A diffusion model and the measurement of the particle diameter reduction rate are used to interpret the dynamic behavior of a single soluble particle.

Chapter 3 introduces the experimental setup we have built to investigate the continuous sedimentation of soluble particles in quiescent water. The experimental processes for different particles are discussed in detail.

In Chapter 4, we introduce the classical buoyancy plume framework by B R Morton et al., 1956. Starting from Reynolds-average Navier-Stokes equations with a mixing length approach, we are able to find self-similar solutions in the two-dimension case (similar to our experimental setup), relating Morton's entrainment coefficient to the momentum and buoyancy mixing closures.

Chapter 5 presents the measurement results of different particle plumes, about the velocity field, and particle concentration. The case of a non-dissolved particle plume is compared with a one-phase buoyancy plume. The differences between butyramide, KNO_3 particles, and plastic beads are discussed and quantified.

Chapter 6 is the conclusion for the whole thesis and some perspectives are drawn.

2 Single particle falling

In this chapter, we present the experiments about a single particle falling in quiescent water. Most of the experimental work in this chapter was done by David Wai-Quan-Chin during his internship, which I supervised with my PhD advisors. The experimental setup was built by two engineers of the lab, Thierry Darnige, and Xavier Benoit-Gonin. In Section 2.1, we introduce the experimental setup and the particle used in the experiment. Then in Section 2.2, we discuss the theory for a single particle sedimenting in the Stokes regime, both for non-dissolving and dissolving particles. Then I present the experimental results in Section 2.3 and 2.3.

2.1 Experimental setup

In order to study the soluble particle plume (Chapter 5), we first investigate the sedimentation and dissolution of isolated particles. We have designed an experimental setup to monitor the falling of a single particle in quiescent water. In order to reach an optimum resolution in the detection of the particle during its dissolution process, the camera and a large magnification objective are fixed on a platform that moves vertically by a stepper motor, at a speed that corresponds to the particle falling velocity. The camera tracks the particle during falling.

2.1.1 Particles used

As shown in Table 2.1, three kinds of particles are used in the experiment. Two of them are plastic beads with different sizes and densities. They are non-soluble, and are used to verify the experimental system. The other one is butyramide, which is a soluble chemical. The density of its saturated solution is almost equal to the one of water, which means that it does not change the density of water after dissolving. Butyramide is also used in the following plume experiments (Chapter 5). Two snapshots of the particles are shown in Figure 2.1.

Particle	Unit	Plastic bead 1	Plastic bead 2	Butyramide
Density	$g\,cm^{-3}$	1.050	1.066	1.030
Particle size	µm	~ 230	~ 140	~ 1000
Sedimentation velocity	$mm\,s^{-1}$	~ 0.7	~ 1.5	~ 1.5
Reynolds number Re	1	0.16	0.21	1.5

Table 2.1: Characteristic of the particles used in single particle falling experiments.

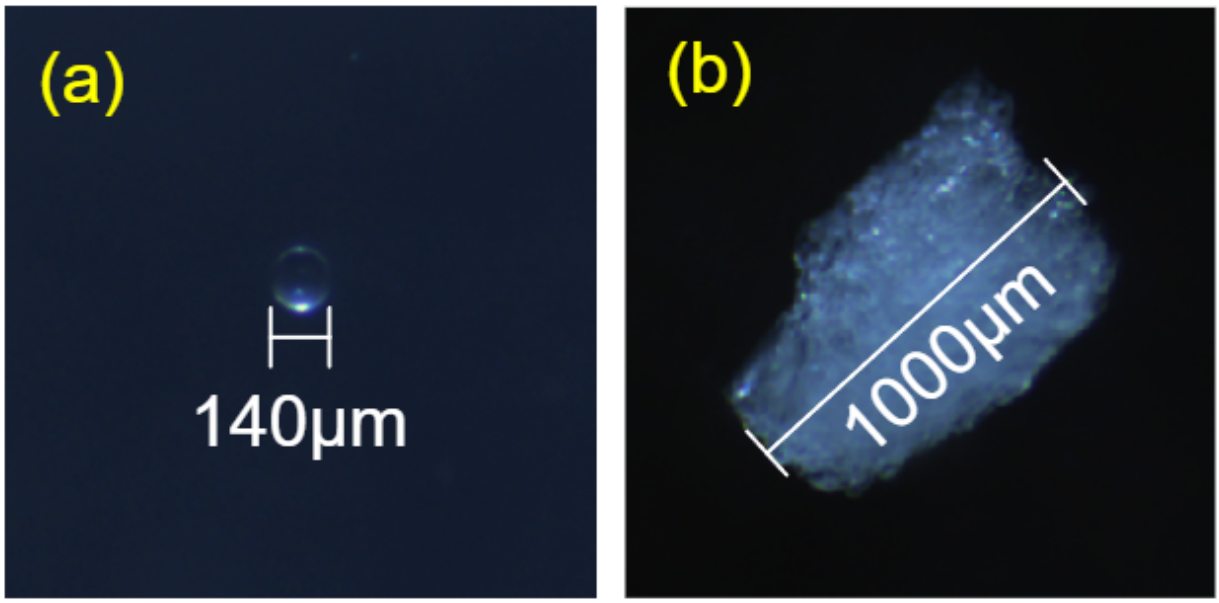

Figure 2.1: The pictures of the particles used in the experiment. (a) Plastic bead; (b) Butyramide.

Since the density of the particles used is close to the one of water, the sedimentation velocity is relatively small, which allows us to monitor the particle for a long period of time, about 100 s. The

Reynolds number is small enough, which means the flow is in the Stokes regime. The Reynolds number Re is defined as:

$$\mathrm{Re} = \frac{\rho_a U d}{\eta} \tag{2.1}$$

where ρ_a is the density of ambient fluid, U is the sedimentation velocity, d is the diameter of the particle (Table 2.1), η is the dynamic viscosity of water.

2.1.2 Setup

We have built an experimental setup to investigate the sedimentation of single soluble particles inside water at rest. The setup schematic is shown in Figure 2.2. On the right side is represented the tank in which the particles sediment. The tank is a 15 cm high transparent acrylic square tank. The cross-section of the tank is a 1.5 cm$\times$1.5 cm square. It is at least 100 times larger than the particle diameter. The particles are released with a syringe at the center of the tank, so that the boundary effect of the tank on the particle sedimentation can be ignored. The tank itself is placed in a water bath, which ensures that there is no convection inside due to temperature differences. The illumination of the particle is performed by a constant LED point source on the oblique top of the water bath.

On the left side of Figure 2.2, we see the camera fixed on a lifting platform to trace the particle during its falling. The camera is fixed on a rail on the platform. The rail allows the camera to move within 20 mm in X direction, which is designed for adjusting the focus. The platform is fixed on a screw rod, which controls its height with a stepper motor (accuracy within 0.1 mm). The camera has a view of 1936 $\times$ 1216 pixels (UI-3060CP-C-HQ Rev.2). The camera lens (VTL0513) is chosen with a fairly large magnification to measure the particle diameter changing during dissolving.

The platform and the camera are both controlled with a LabView program on the computer. This LabView program controls the system with a feedback loop. First, the program receives the image from the camera and identifies the single particle vertical location in the image with

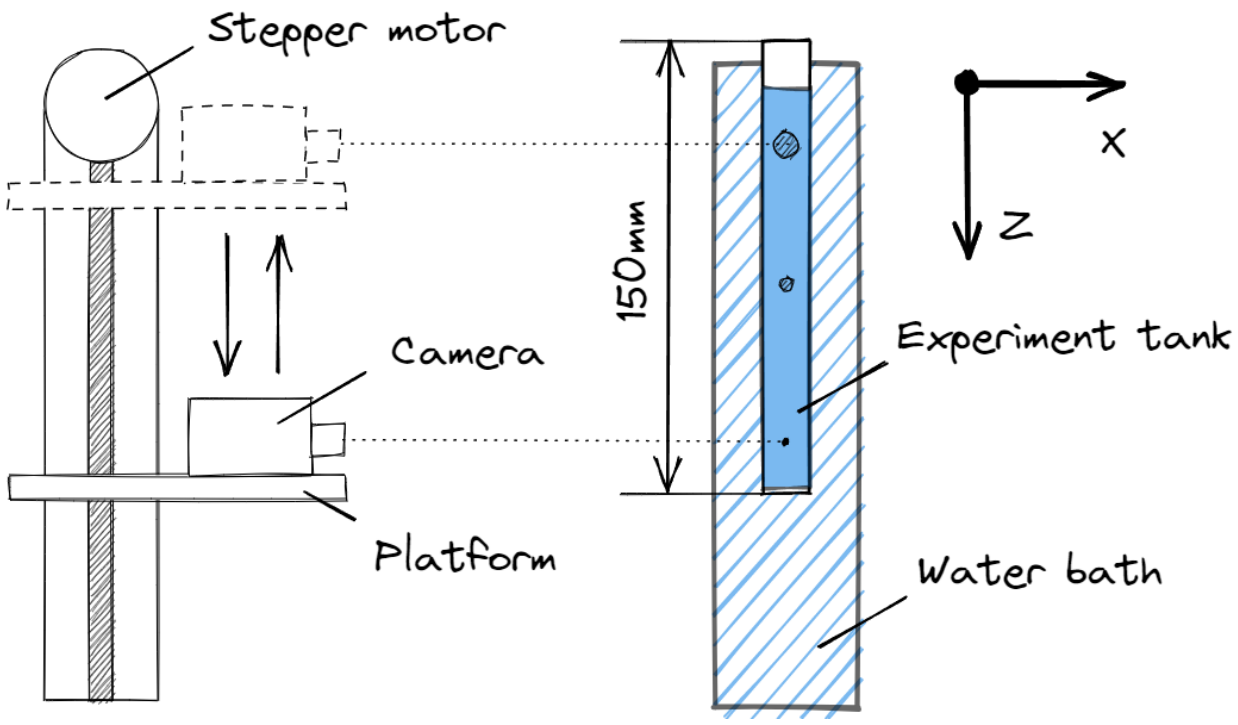

Figure 2.2: The experimental setup schematic for single particle falling.

a threshold. Then the program controls the stepper motor to move up and down to ensure that the particle is always in the middle of the image. By repeating this process, the camera is moving along with the particle at the same velocity in z direction. The maximum frequency of this feedback loop is 10 Hz, so the measurement rate of the camera is set to 10 Hz as well. The maximum velocity of the platform is about 20 mm s^{-1}, which ensures that the camera is always capable to follow the particle sedimentation. The program records images and platform locations simultaneously. By measuring the particle relative position in the image, the particle absolute position in the tank is calculated using the platform location.

2.1.3 Particle injection

For plastic beads, in order to avoid some air bubbles stuck on the particles, they are pre-mixed with water before the injection. As shown on the left panel of Figure 2.3, the tank is filled with

24 °C tap water. The solution with particles inside is injected with a syringe. A 25 mL syringe is fixed on the top of the tank, and connected to the tank with its needle. The top of the needle is just below the water surface. Because the density of the plastic beads is larger than the one of water, the particles in the syringe sediment after fixation of the syringe on the top. The tracking program is launched when a single particle leaves the needle into the tank. The particle is then tracked during its sedimentation.

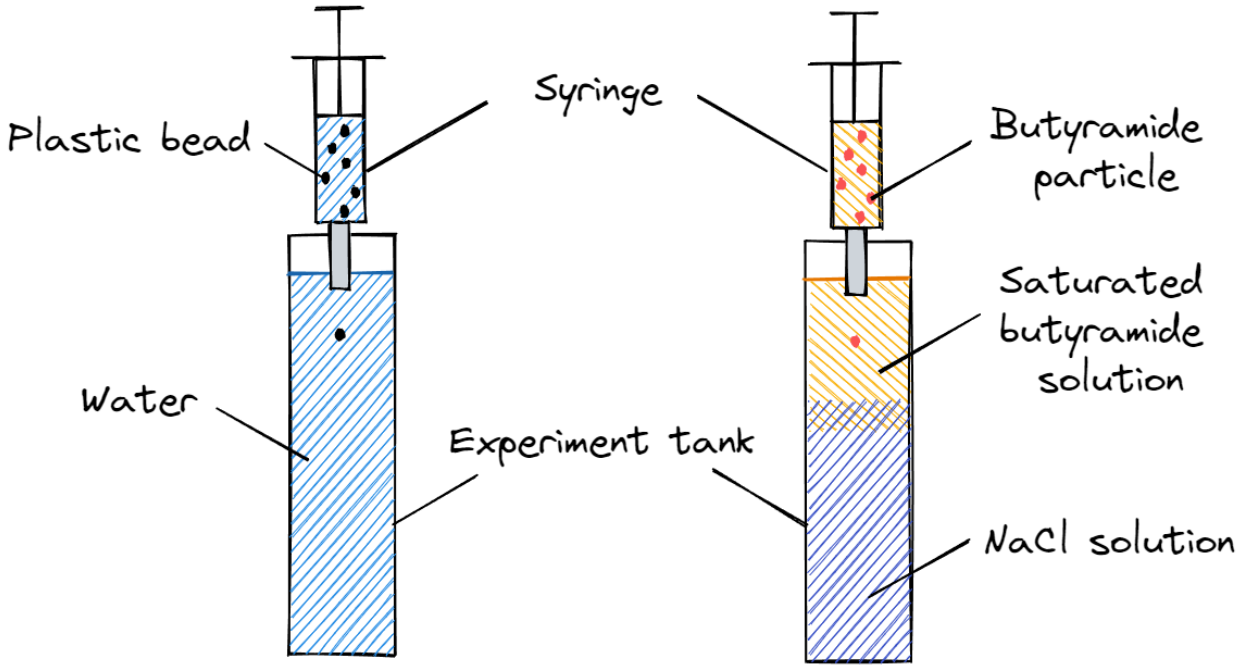

Figure 2.3: The schematic of single particle injection into the tank for different particles, plastic bead (black points) and butyramide (red points).

For butyramide particles, we proceed similarly to the plastic beads. The butyramide particles are pre-mixed with saturated butyramide solution to avoid air bubbles. As shown on the right side of Figure 2.3, the butyramide particle is injected into a stratified system. The top is a saturated butyramide solution, and below is water with a small amount of NaCl to increase its density, at 1.016 g cm^{-3}. The densities are measured using a pycnometer (a glass bottle with a fixed accurate volume of 10.164 cm^3) and an accurate balance (±0.0002 g). The density of NaCl solution is higher to make sure that it stably stays below the saturated butyramide solution.

There are two reasons for using this stratified system. First, the butyramide particle is only dissolving in the bottom layer, which is far away from the needle. This reduces possible noise due to the syringe, like shaking. Second, since the particles are not spheres, estimating its volume by a single projection on the image is not accurate. When butyramide particle is sedimenting in its saturated solution, the volume of the particle is constant. This first part of the sediment motion provides us the possibility to estimate the particle equivalent diameter from the theory, as explained below.

2.2 Theory

2.2.1 Single particle falling in Stokes regime

We consider a solid sphere particle of size d, sedimenting at velocity U in a quiescent fluid of kinematic viscosity η. In Stokes regime, the drag force F acting on this particle is:

$$F = 3\pi\eta dU \tag{2.2}$$

In steady state, the drag force F is balanced by gravity minus buoyancy. The sedimentation velocity U is thus given by:

$$U = \frac{1}{18}\frac{\Delta\rho g d^2}{\eta} \tag{2.3}$$

where $\Delta\rho$ is the density difference between the particle and ambient fluid, $g = 9.8\,\mathrm{m\,s^{-1}}$ is gravity acceleration.

2.2.2 Dissolving particle

We assume that the dissolution process is controlled by diffusion. The concentration of the dissolved salt is c_0 close to the particle, and is zero very far from it. The particle sediments in water

due to gravity. As mentioned above, we assume that the particle Reynolds number is small, but also that the Péclet number is large. The definition of Pe is:

$$\mathrm{Pe} = \frac{Ud}{D} \tag{2.4}$$

Both hypotheses of small Reynolds and large Péclet number are compatible, since the kinematic viscosity of water $\eta = 1 \times 10^{-6}\,\mathrm{m^2\,s^{-1}}$ is much higher than the mass diffusion coefficient $D = 1.07 \times 10^{-9}\,\mathrm{m^2\,s^{-1}}$ at 25 °C (Winkelmann, 2018).

According to the calculation by Levich, 1962, the mass transfer rate $\dot{M}$ is given by:

$$\dot{M} = 3.2 D d c_0 \mathrm{Pe}^{1/3} \tag{2.5}$$

where D is the mass diffusion coefficient of the dissolved salt in water. The coefficient 3.2 is a constant number coming from the integration.

The mass of the particle m_p is given by:

$$m_p = \frac{1}{6}\rho_p \pi d^3 \tag{2.6}$$

where ρ_p is the density of the particle.

Differentiating with respect to t on both sides of Equation 2.6, we obtain the mass transfer rate $\dot{M}$:

$$\dot{M} = \frac{\mathrm{d}m_p}{\mathrm{d}t} = \frac{1}{2}\rho_p \pi d^2 \frac{\mathrm{d}d}{\mathrm{d}t} \tag{2.7}$$

Substituting Equations 2.3, 2.4, and 2.5 into Equation 2.7 and defining the diameter reduction rate $\dot{d} = \frac{\mathrm{d}d}{\mathrm{d}t}$, we have:

$$\dot{d} = \frac{\mathrm{d}d}{\mathrm{d}t} = 3.2 \frac{2}{\pi} \left(\frac{1}{18}\right)^{1/3} \frac{D^{2/3} c_0}{\rho_p} \left(\frac{\Delta \rho g}{\eta}\right)^{1/3} \tag{2.8}$$

where all factors on the right-hand side are constant, which means that the radius d changes

linearly with time t. The diameter reduction rate $\dot{d}$ thus only depends on the parameters of salt and solution. Based on Equation 2.8, for a particle with given diameter d_0, the total time t_b for the particle to dissolve completely can be calculated easily.

Replacing diameter d in Equation 2.3 with $d = -\dot{d}t + d_0$ where d_0 is the particle initial diameter, we have:

$$U = \frac{1}{18}\frac{\Delta\rho g}{\eta}(-\dot{d}t + d_0)^2 \tag{2.9}$$

The particle vertical location z can be calculated by integrating Equation 2.9:

$$z = \int U dt = \frac{1}{18}\frac{\Delta\rho g}{\eta}(\frac{1}{3}\dot{d}^2 t^3 - \dot{d}d_0 t^2 + d_0^2 t) + z_0 \tag{2.10}$$

where the factor z_0 is the initial location of the particle. We can choose it for the origin of z and set it to 0. We also choose this point to start the data fitting. Equation 2.10 means the curve of particle z location changes with time is a cubic curve.

Besides direct measurement, the equation 2.10 provides another way to measure the diameter reduction rate $\dot{d}$. $\dot{d}$ and d_0 are measured by fitting the trajectory curve of the particle, as shown in Figure 2.10 below.

2.2.3 Parameters calculation

Here we list some important parameter values that enter the theoretical predictions in Table 2.2. For butyramide, we use $D = 10^{-9}\,\mathrm{m^2\,s^{-1}}$ (Winkelmann, 2018). The concentration c_0 is the butyramide saturated concentration, $c_0 = 200\,\mathrm{kg\,m^{-3}}$ at 25 °C (Romero and González, 2010). The bulk density of butyramide is $\rho_p = 1030\,\mathrm{kg\,m^{-3}}$, and $\Delta\rho = 14\,\mathrm{kg\,m^{-3}}$. As shown in Table 2.2, our assumptions of a small Reynolds number, and high Péclet number are indeed satisfied. According to Equation 2.8, the diameter reduction rate $\dot{d}$ for butyramide is constant, about $7.8\,\mu\mathrm{m\,s^{-1}}$

The above calculation is based on the assumption that the butyramide particle is a perfect sphere. However, butyramide is a crystalline chemical where the monocrystals are not isotropic,

d_0 (μm)	t_b (s)	z_b (mm)	U_b (mm s^{-1})	Re	Pe
140	18	0.9	0.15	0.021	20.9
200	26	2.6	0.30	0.062	61.0
400	51	20.9	1.22	0.50	488
800	103	167.1	4.88	4.00	3900

Table 2.2: Theoretical characteristic values for butyramide. t_b is the total time for the particle to dissolving completely, and z_b is the total sediment length. U_b is the maximum sediment velocity.

so the particle shape typically shows facet. The shape of the particle influences the sedimentation velocity. The particle orientation also changes its velocity, as illustrated in Figure 2.9.

2.2.3.1 Image processing

Since we are interested in the particle diameter reduction rate $\dot{d}$, the measurement of the particle diameter on the pictures is the key point for the data processing. Figure 2.4 shows the general data process for a single particle image. Figure 2.4(a) is the raw full-colored image with a polycrystal. We first change the image into a gray image, like in Figure 2.4(b). Then the image is converted into a binarized image (Figure 2.4(c)) with a certain threshold. The boundary of the particle is obtained after convex hull (Figure 2.4(d)), which fills the holes inside of particle binarized image. We define the equivalent diameter as the diameter of a disc with the same area as the measured area.

2.3 Result for non-soluble particles

First, we inject the non-soluble plastic beads to test the reliability of the tracking system. One single particle is injected into quiescent water. The camera keeps tracking the particle. The particle diameter is also measured during falling. Figure 2.5 displays the particle Z location (black line) as a function of time during falling. The particle Z location changes with time linearly after about 30 s, which is fitted in red dash line. The particle velocity is a bit larger at the beginning. It maybe due to the influence of the needle, which provides an initial speed to the particle.

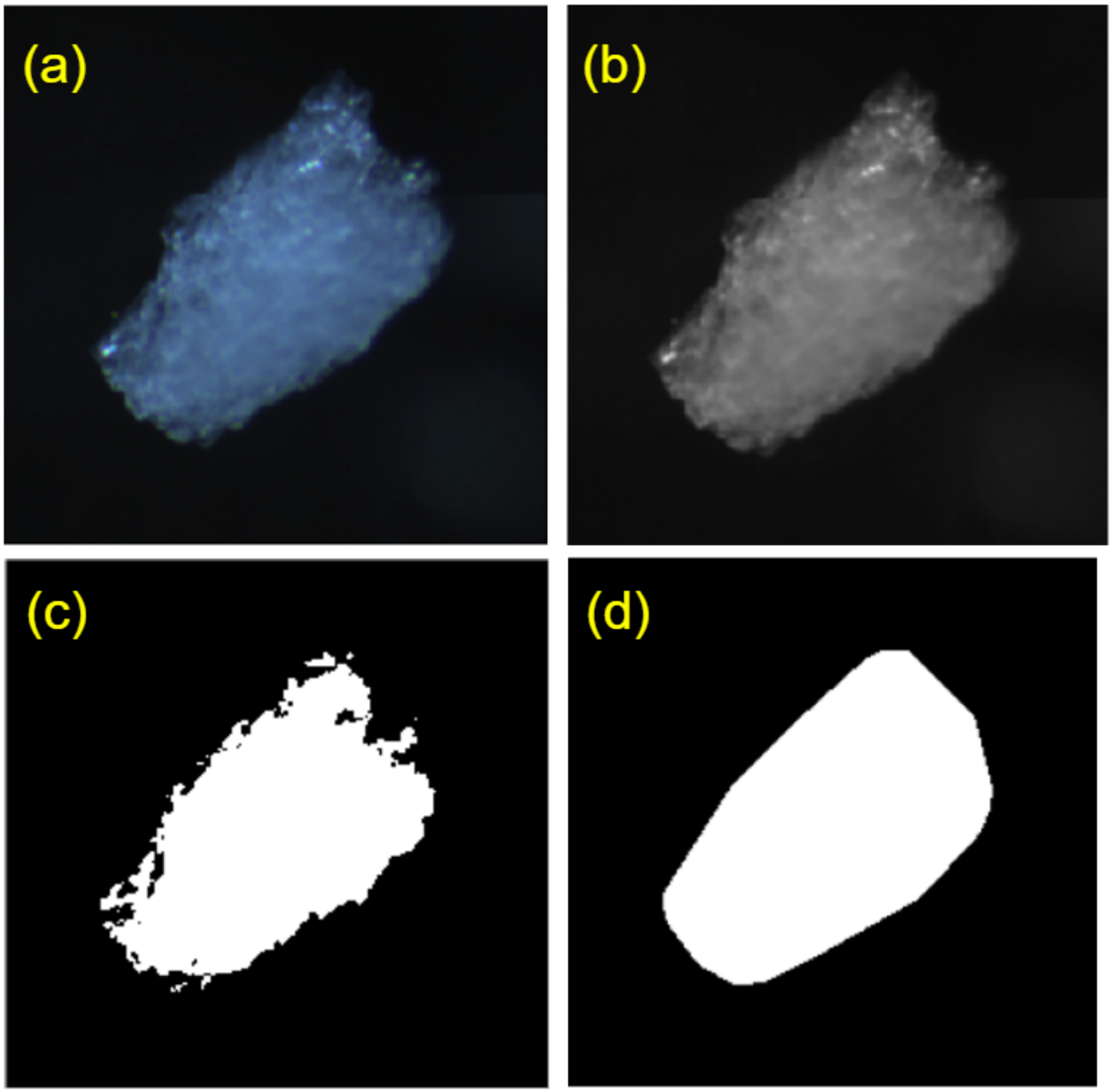

Figure 2.4: The image processing for a single particle. Image for a single Butyramide particle. (a) Raw image; (b) Gray image; (c) Binarization image with a threshold; (d) The image after convex hull.

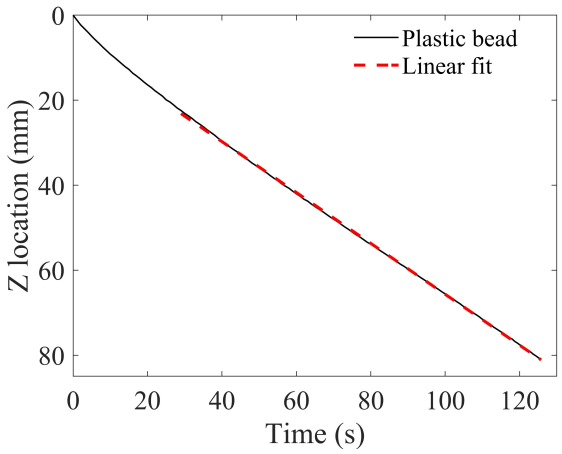

Figure 2.5: The Z location of a single plastic bead ($\rho = 1.066\,\mathrm{g\,cm^{-3}}$) falling in quiescent water.

By repeating this single plastic bead experiment, we have the relationship between the particle diameter d and its sediment velocity U, shown in Figure 2.6. The round circles are the experimental results and the solid lines are the sedimentation velocities calculated with Equation 2.3. Two kinds of plastic beads with different densities are distinguished with red and black. The sedimentation velocities are always found smaller than the theoretical prediction, and only a few have good agreement with the theory. We suspect that this deviation is due to the fact that there is some air stuck with the particle, which changes the equivalent density significantly. Since the particle is hydrophobic, the particle may trap a thin layer of air. In some cases, we see some bubbles stuck on the particle.

2.4 Results for soluble particles

For soluble particles, the butyramide grains are injected into a stratified system, as shown in Figure 2.3. The particle sedimentation velocity vary a lot when particle goes through the transition region between the two layers.

In order to make the stratified layers visible, we add some fluorescein in the bottom layer, with a violet laser on the side. By measuring the light intensity at different heights, two homoge-

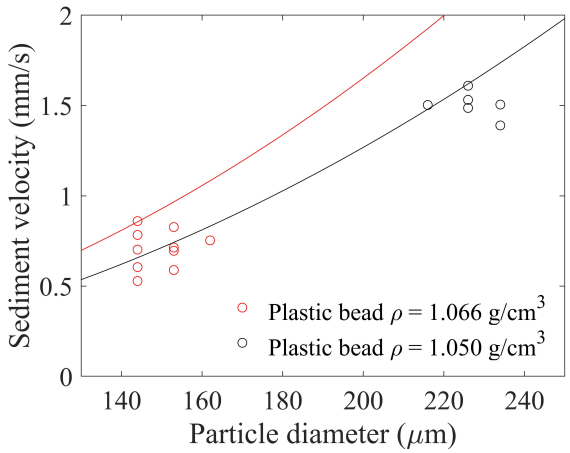

Figure 2.6: Sedimentation velocity for plastic beads. The lines are theoretical sedimentation velocities in Stokes regime. Red for plastic bead 1 ($\rho = 1.066\,\mathrm{g\,cm^{-3}}$), Black for plastic beads 2 ($\rho = 1.050\,\mathrm{g\,cm^{-3}}$). The points are measurement results and the lines are theory productions calculated with Equation 2.3.

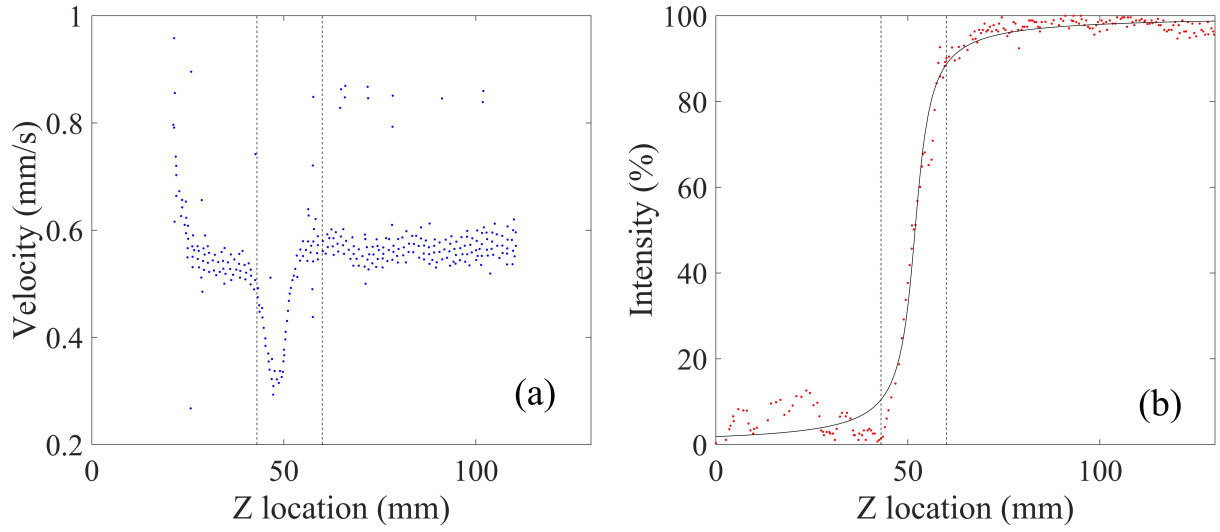

Figure 2.7: Sedimentation of butyramide particles in a stratified fluid (see schematic Figure 2.3). (a) Particle vertical velocity as a function of height; (b) The normalized fluorescent intensity in different heights. The vertical black lines indicate the point where intensity equal to 10% and 90%.

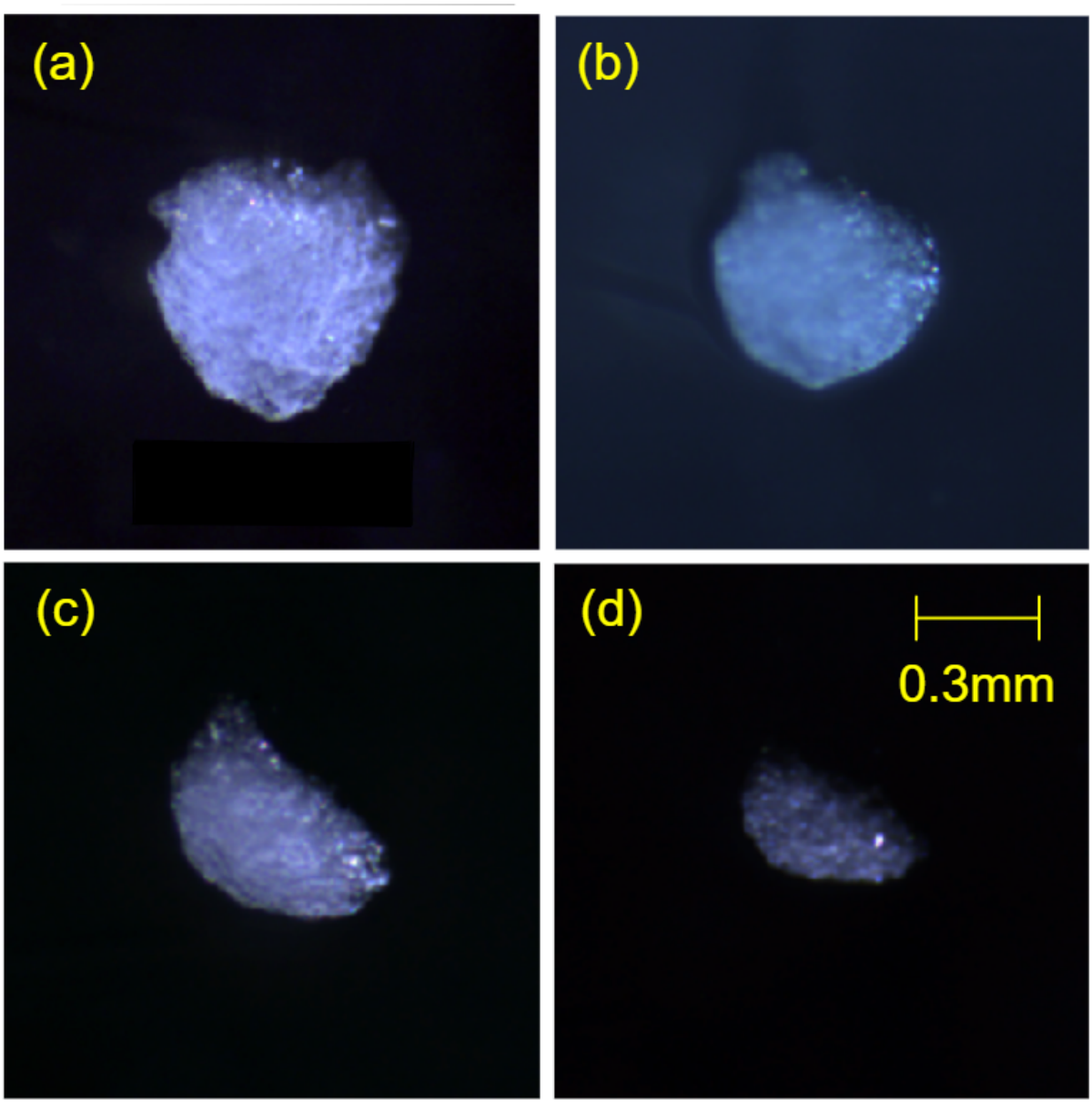

Figure 2.8: Example of tracking of a butyramide particle dissolving during its falling. Photos at different times (a) 10 s; (b) 20 s; (c) 30 s; (d) 40 s.

neous layers and a transition region can be distinguished. The normalized intensity is shown in Figure 2.7(b). Figure 2.7(a) shows the sedimentation velocity of a butyramide particle at different heights. The velocity decreases by a factor of 2 at around 50 mm, in the transition region between the two layers. This phenomenon is in agreement with a result published by (Magnaudet and Mercier, 2020), where the authors find the same type of graph for sedimentation velocity decreasing in a stratification zone.

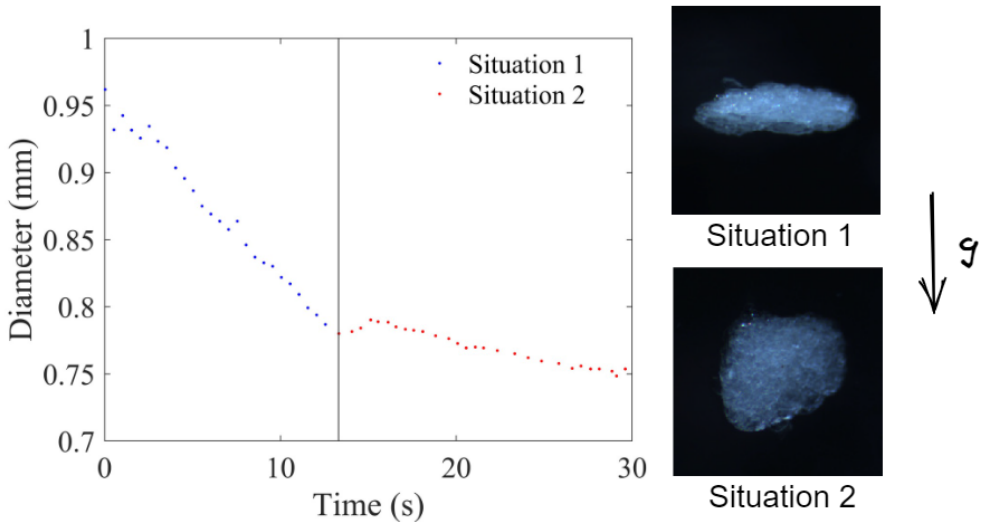

Figure 2.9: The variation of the equivalent diameter due to a change in the orientation of the particle.

When the butyramide particle falls down in the bottom layer, the particle dissolves and slows down, as shown in Figure 2.8. The particle does not dissolve homogeneously and its shape and orientation can change during the falling. Figure 2.9 shows an example of the particle orientation changing. It is a disc-shaped particle that flips of 90° at around 13 s. According to Oehmke et al., 2021, the dissolving rate for disc-shaped particles is higher than for spheres. In particular, the authors determined that the important factor which governs the dissolution is the ratio between the effective surface facing the flow and the volume. As shown in Figure 2.9, the particle equivalent diameter decreases slower after the flip. Since in the theory we assume that the particle is a sphere, for the rest of the results, we preferred to select particles as round as possible.

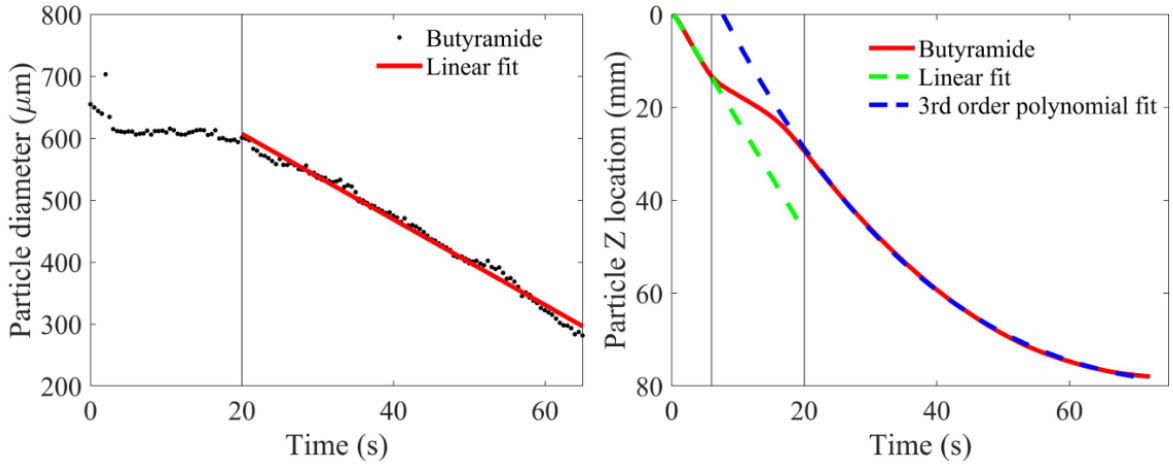

Figure 2.10: Example of measurement during the sedimentation of a butyramide particle. During 7 s to 20 s, the particle is within the transition part. (a) Diameter d as a function of time; (b) Particle Z location as a function of time. The fit curve is expanded outside of the fitting region for the sake of visibility.

Figure 2.10 presents the measurement results for one single round butyramide particle. Figure 2.10(a) shows the particle equivalent diameter, which is directly measured on the image with particle area. The details about the processing are shown in Figure 2.4.

There are three stages to consider. The first stage is the linear regime where the particle sediments with its limit speed, from 0 s to about 8 s. The second is a transition part where the particle evolves in the region stratified in density, between 8 s to 20 s. In this part, the stratification causes a slowing down of the particle. Indeed, one notices on the curve a weaker slope in Figure 2.10(b). In these two stages, the particle does not dissolve, its diameter in Figure 2.10(a) is almost constant for 20 s.

For the third stage, the measurement after 20 s, corresponds to our model (Equation 2.10), where the particle dissolves. A slowdown is observed due to the loss of material. As shown in Equation 2.10, the curve is well fitted with a polynome of degree three. The curve fits the raw data nicely. The fitting is more accurate for the particle that dissolved completely in the measurement. Eventually, we get two independent values for the particle initial diameter d_0 and particle diameter reduction rate $\dot{d}$ based on Figure 2.10(a) and (b).

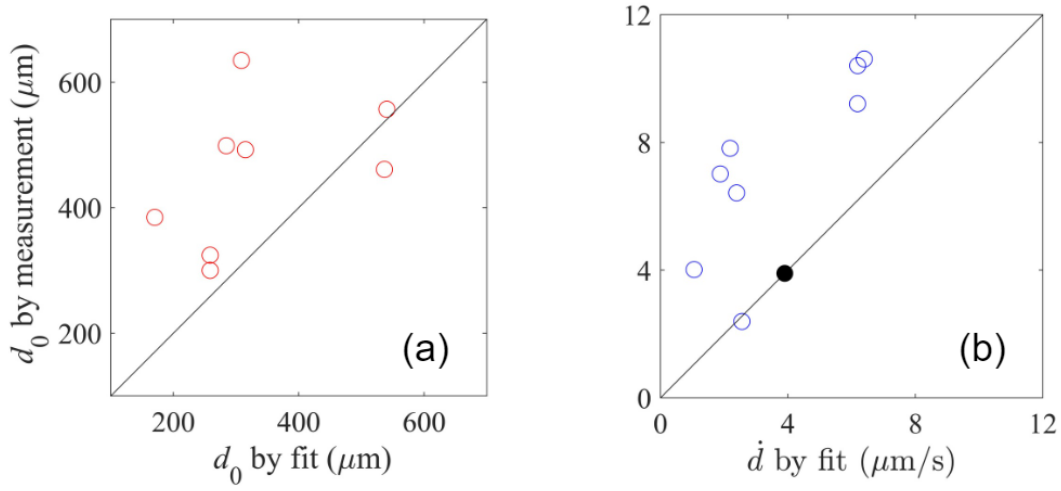

Figure 2.11: Comparison of measurements and fits for (a) Particle equivalent diameter; (b) Particle diameter reduction rate, where the black point is the theoretical value for a sphere. The black lines represent the place where the measurement result for two methods are equal.

By collecting the results for spherical butyramide particles, we compare the direct measurement and fit measurement for two parameters, particle equivalent diameter d, and particle diameter reduction rate $\dot{d}$ in Figure 2.11. The values obtained by fitting are always smaller than those obtained by direct measurement. This may be due to the fact that the convex hull (Figure 2.4) which is performed during the image processing tends to overestimate the equivalent diameter. Moreover, the direct measurement only considers one projection of the particle. Compared to measuring the particle area, measuring the particle location in the image is more accurate. From the model, the particle diameter reduction rate $\dot{d} \approx 3.9\,\mu\mathrm{m\,s^{-1}}$ is constant. The order of magnitude of experimental results agrees with the theoretical prediction.

2.5 Conclusion and perspective

With the help of two engineers in the lab, we have designed and built a lifting platform system, which can track a single salt particle in quiescent water and monitor its dissolving process. This system identifies the real location of a sedimenting particle with a camera fixed on the platform

and adjusts the height of the platform automatically to ensure the particle is always in the image.

The system is tested with steady sedimentation velocity of plastic beads. Two kinds of plastic beads are used. One has the diameter around 230 μm, density 1.050 g cm^{-3}. The other one has the diameter around 140 μm, density 1.066 g cm^{-3}. The experimental results show that the measured velocities are in agreement with the theoretical prediction in some cases. In most cases, the measured velocities is smaller than the theoretical prediction. It is probably due to the fact that the plastic beads used are hydrophobic, so some air bubbles stuck with the beads, are likely to be reducing the sedimentation velocity.

With a diffusion model in Stokes regime, we notice that, for sphere dissolving particle, the particle diameter reduction rate is a constant value. We also derive the vertical location of dissolving particle change with time, which is a third-order polynomial.

We use butyramide for single salt particle dissolving, which is also used for plume experiment in Chapter 5. Since the butyramide particle is not a perfect sphere, the orientation of the particle influences the particle dissolving rate. The particle dissolved quicker with larger effective surface facing the flow. For sphere-like particles, we compare the particle initial diameter d_0 and diameter reduction rate $\dot{d}$ with two different measurement methods. One is direct measurement and the other is fit measurement. The order of magnitude of $\dot{d}$ measured in the experiments agrees with the theoretical estimation. The direct measurement is always higher than the other way, which is probably due to the fact that the image process enlarges the particle a bit.

The experimental preload still needs to be improved, especially regarding the particle preparation. The measurement results are very sensitive to the bubbles attached to the particle, which should be avoided with a suitable preparation, like re-crystallizing the particle with over-saturated solution. Some special treatment is needed to select sphere-like butyramide particles, which can improve the reproducibility of the experiment and the comparison to the theoretical predictions.

3 Experimental setup

3.1 General setup

We have built an experimental setup to investigate the continuous sedimentation of soluble particles inside the water at rest. The two major physical quantities measured are the velocity field and the particle concentration field.

The general experimental setup is shown in Figure 3.1. The solution containing soluble particles is placed within a water bath on a scale. The solution is injected into a 2D tank through a pump. Figure 3.2 shows the experimental setup from the front and back views. The different parts are indicated with different colors in the photos. In a $1000\,\text{mm} \times 600\,\text{mm} \times 18\,\text{mm}$ tank, which is considered as a 2D tank because the width of the tank is relatively small compared to the other dimensions. The solution containing the particles is injected from a localized point at the top.

The characteristics of the particles used in the experiment are shown in Table 3.1. Butyramide is a crystalline solid at room temperature and is soluble in water (Romero and González, 2010). Its density ($1.03\,\text{g}\,\text{cm}^{-3}$) is higher than water but very close. The density of saturated butyramide solution ($0.999\,\text{g}\,\text{cm}^{-3}$) is also close to the one of water, which means that this salt almost does not change the water density after dissolving. Butyramide has also a relatively large latent heat ($395\,\text{J}\,\text{g}^{-1}$), which works its dissolution analogue to the evaporation of droplets and cools the surrounding air. During rain, the rain droplets evaporate and cool the surrounding air.

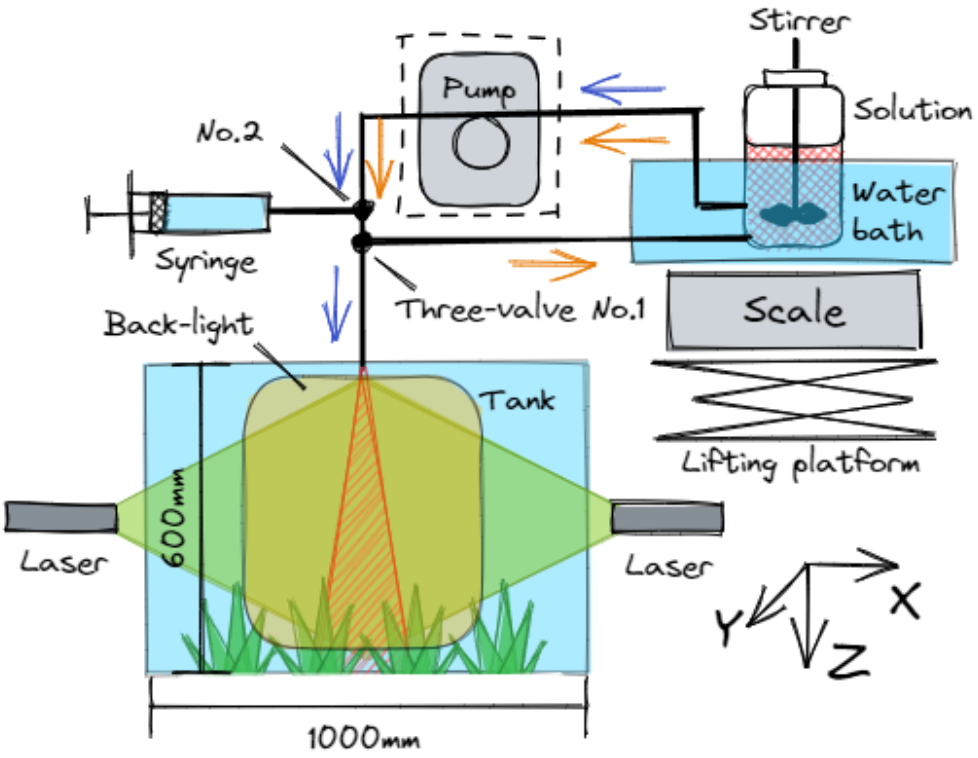

Figure 3.1: Experimental setup schematic. The pump in the dash line box is optional for different injection methods.

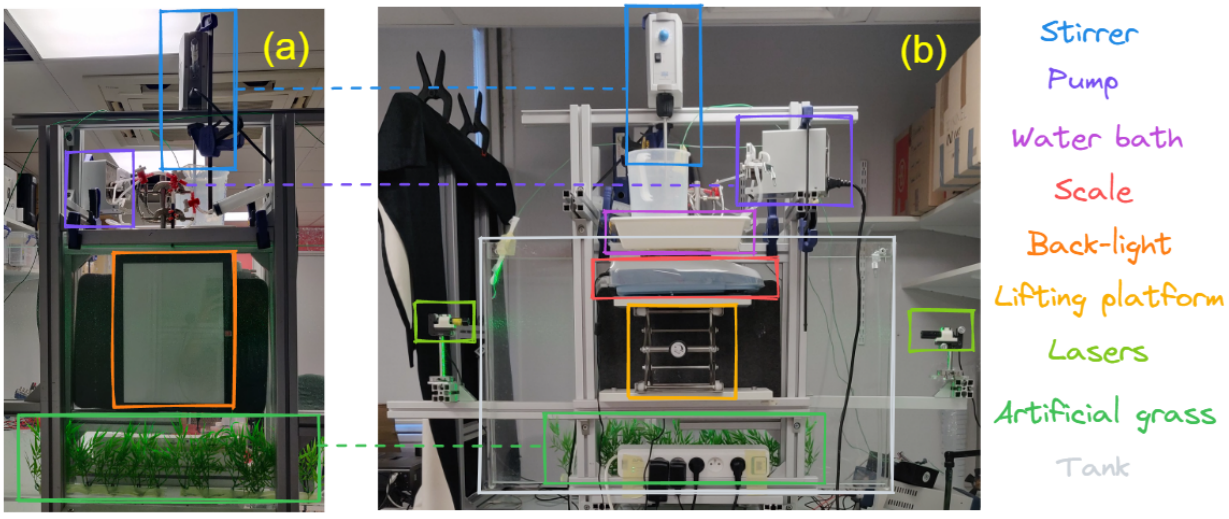

Figure 3.2: Pictures of the experimental setup. (a) front view, and (b) back view.

We compared butyramide with two other particles, plastic beads and KNO_3. The plastic bead is a non-dissolving reference for butyramide. The density of the plastic bead ($1.066\,g\,cm^{-3}$) is also close to water, slighter larger than butyramide. KNO_3 is soluble in water and has a relatively large latent heat of dissolution like butyramide, but it increases the water density after dissolving by 17%. KNO_3 is used as another reference for butyramide.

Particle	Unit	Plastic beads	Butyramide	KNO_3
Density	$g\,cm^{-3}$	1.066	1.03	2.10
Particle size	mm	0.14 - 0.20	0.14 - 0.20	0.14 - 0.20
Latent heat of dissolution	$J\,g^{-1}$	/	395	347
Saturated concentration (25 °C)	$g\,L^{-1}$	/	216	350
Saturated solution density (21.5 °C)	$g\,cm^{-3}$	/	0.999	1.175

Table 3.1: Characteristic of the particles used in experiments (Romero and González, 2010).

As shown in 3.1, the density of particle beads and butyramide is close to and higher than the one of water. One major challenge for this setup is to find how to continuously inject these particles. If we release dry particles directly above the water continuously, they cannot fall down freely through the water surface by gravity. The surface tension holds the particles on the surface where they accumulate. When the accumulated particles become heavy enough, they fall into the tank as a whole part with some trapped air. In order to avoid this problem, the particles are premixed with the saturated solution, and injected into the tank together through a tube as homogeneously as possible. As a reference, the plastic beads are premixed with pure water.

In Figure 3.1, the mixed solution (particles in saturated solution) is in a plastic bottle placed on a weight scale. The total injection rate could be calculated by monitoring the total change of weight on the scale with time. The bottle is in a water bath to keep its temperature similar to the water in the tank. A stirrer mixes the solution to ensure that the particles are suspended homogeneously. In order to avoid particle sedimentation inside the tube before injection, a circulation of the solution in the pipeline is imposed, as indicated by the orange arrows in Figure. 3.1.

There are two ways for continuous injection. One is using a peristaltic pump and the other

one consists in letting the solution fall down freely. For free falling method, the injection is driven by the height difference between the water surface of the solution bottle and that of the tank.

Since there are particles inside of the solution being pumped, a peristaltic pump is used, because the moving parts of the pump are not in contact with the fluid. Also, the pumped fluid is in contact only with the inside surface of the tubing. It is easy to clean the inside surfaces of the tube. In the current setup, the peristaltic pump is suitable for the total injection rate between 0.10 to 1.00 $\mathrm{g\,s^{-1}}$. When the injection rate is under 0.10 $\mathrm{g\,s^{-1}}$, the pulsation of the pump becomes inefficient. On the other hand, 1.00 $\mathrm{g\,s^{-1}}$ is the possible maximum injection rate for the peristaltic pump we used.

The free-falling method is used for total injection rates larger than 0.80 $\mathrm{g\,s^{-1}}$. Due to the friction loss along the tube, it is more difficult to hold the free-falling injection rate when it is smaller than 0.80 $\mathrm{g\,s^{-1}}$. The pump in Fig. 3.1 is removed, and the injection rate is controlled by the lifting platform under the scale. During the experiment, we use the lifting platform to ensure a constant height difference between the water surface in the solution bottle and at the outlet in the tank.

An entrance is fixed in the middle of the tank top. As shown in Figure 3.3, it is a 100 mm long transition part from a 6 mm round cross-section to a 2 mm $\times$ 16 mm rectangle. In order to have a better homogeneous output, there are some passive mixing-enhancing structures in it. The entrance is made by 3D printing with photosensitive resin. The tubes with 6 mm inner diameter connect each part. A three-way valve (No.1) switches the system from recycling to injection. The solution is injected following the blue arrows into the tank. The syringe and valve No.2 are used to empty the air in the entrance each time after replacing the water in the tank.

At the bottom of the tank, there are several artificial grasses with a height of about 18 cm. They provide extra flow resistance to slow down the fluid going through, and stabilize the system during the injection. Without the grass, the plume bumps into the bottom, and leads to two large symmetrical vortices on the sides. The grass reduces this bottom effect.

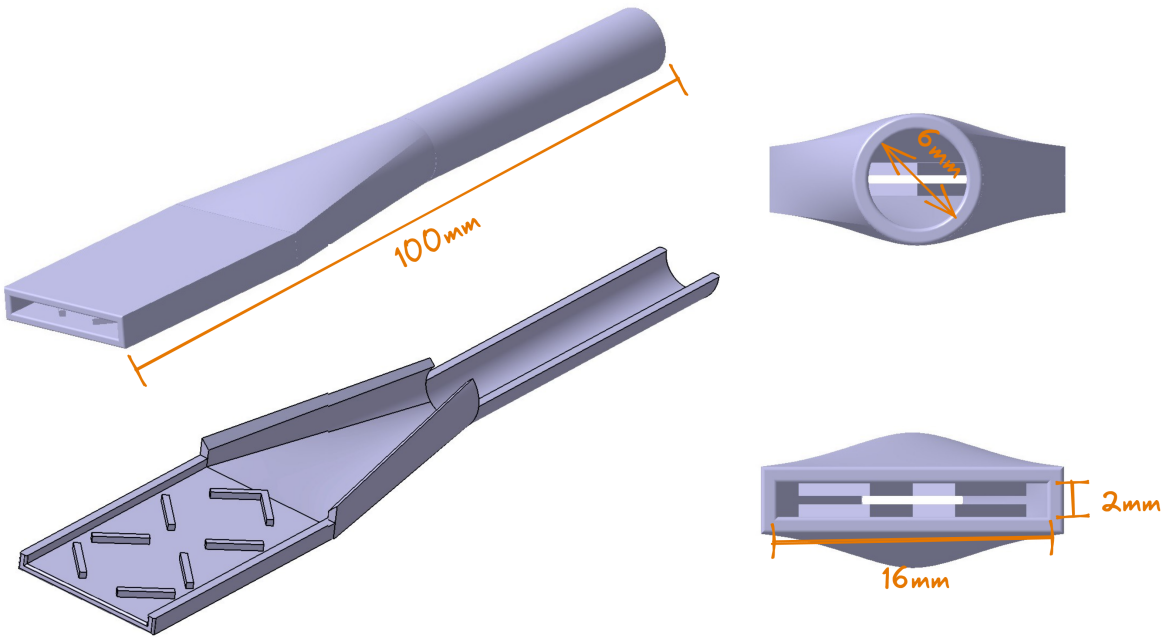

Figure 3.3: The entrance device on the top of the tank.

There are two lasers (LD532-20-24(20X80)-PL-C3000) one on each side of the tank. Both lasers are stable line laser with 532 nm green light, 20 mW, 90° fan open angle. If we use only one laser during the injection, the particles inside of the plume shade the light path of the laser on the other side. These two lasers are fixed on each side with a multi-axis tilt platform. The tilt platform provides accurate rotation on two axes and displacement in one direction. It ensures the overlapping of two laser sheets.

About 1.5 m in front of the tank middle, a 1936 × 1216 pixel color camera (UI-3060CP-C-HQ Rev.2) with a 12.5 mm objective (Myutron HS1214V) is used for imaging. Particle image velocimetry (PIV) is used to measure the velocity field in the middle plate of the tank. The PIV tracer particles used are polyamide seeding particles (50 µm) from DANTEC Dynamic.

A 5 W LED light box (RS PRO 136-3720) is placed in the middle of the tank backboard as a backlight. This light box offers homogeneous illumination from a built-in LED light source, reducing the appearance of shadows and dark spots. During the injection, the particles inside

of the plume shade this backlight when looking from the other side. At first order, the decrease of the light intensity is linear with the particle local concentration. With proper calibration, the particle concentration field is measured. The calibration is further discussed in the following sections.

3.2 Experimental process

In Section 3.2 we discuss the general procedures for all kinds of injected solutions in the experiment, and emphasize two difficult parts, which are solution preparation, and solution injection in detail.

3.2.1 Experimentalw procedures

In Section 3.2.1 we discuss the general procedures for the plastic bead plume experiments first. The procedures for the dissolved NaCl plume, butyramide plume, KNO_3 plume are similar to plastic beads plume, except for some key parts. The differences are discussed in Section 3.2.1.2 to Section 3.2.1.4 in detail.

3.2.1.1 General procedures for plastic beads

Below are the general procedures for the plastic beads plume experiment. For the other particles, they follow similar steps except for the items mentioned below.

1. **Preparation of the water for the tank.** The tank water is prepared in advance with tap water and 50 µm PIV beads. The water is stored in 10 L buckets for more than 24 hours to reach thermal equilibrium. The concentration of the PIV beads is $0.05\,\mathrm{g\,L^{-1}}$ in tank water. $0.05\,\mathrm{g\,L^{-1}}$ of surfactant (handwash) is also added to avoid the clustering of PIV beads. At least 50 L tank water should be prepared, in case of replacements during the experiment.

2. **Preparation of plastic beads.** The size of the plastic beads used is selected with several sieves. Three sieves are used for separating the plastic beads. From top to bottom, the size of sieves are 0.400 mm, 0.200 mm, and 0.140 mm. The plastic beads between 0.140 mm and 0.200 mm are used during the experiment. A Retsch sieve shaker is used for separation for 60 minutes with a strength of 30. This step is repeated 1 to 3 times to have enough plastic beads.

3. **Removing air from solution.** The injected solution is a mixture of water and plastic beads. This solution may contain plenty of air bubbles, due to the air trapped between the dry beads. The air bubbles stick to the particles, because the plastic is hydrophobic. The beads form some clusters in the solution. During the injection, since the density of particles is close to the one of water, these clusters are raising when they get injected into the tank. The air bubbles in the solution disturb the flow field because they change the buoyancy behavior of the plume entirely.

   To minimize the number of bubbles in the solution, the dissolved air in the water has been removed by a vacuum pump before mixing. Moreover, in order to avoid the dilution of PIV beads in the tank by injection, the tank water prepared in step 1 also contain plastic beads. These stocks of water already contrain PIV beads.

   About 2000 mL tank water is added to a graduated beaker with a magnetic mixer. Then the beaker is put into the vacuum chamber (BUCHI vacuum pump V-100). The pressure inside of the chamber is reduced to 60 Pa for about 20 minutes. Below the vacuum chamber is the magnetic stirrer (VMS-C7). It is stirring the liquid to remove the air bubbles at the speed of 1 to 1.5. In order to minimize the temperature change of the solution, the solution cannot stay in the vacuum any longer. Because the vacuum environment enhances the evaporation cooling effect, the solution can be colder for about 0.5 °C after 30 minutes of staying in the vacuum.

4. **Preparation of the mixed solution.** The solution used for injection contains 10% plastic beads. The value of the particle concentration is discussed in the following sections. For one day experiment, we prepare 2000 mL mixed solution. In order to further reduce the number of bubbles in the mixed solution, the mixing process is handled under CO_2 environment. This ensures that the bubbles left in the solution will dissolve immediately, and keep the solution bubble-free.

   The room and solution temperatures are measured before and after the preparation. The bottle used for solution injection is a 2 L graduated beaker which has two holes close to the bottom. For mixing, this bottle is put on the scale. Two water stop clamps are used to close the bottle temporarily. First, 200g plastic beads (0.140 mm to 0.200 mm) is added in the bottle. The bottle is covered with a tissue to slow down the motion of gas coming out. The compressed CO_2 cylinder is connected to the solution bottle through a specific tube and valve. The bottle is filled with CO_2 gently. Since CO_2 is denser than air, CO_2 stays at the bottom of the bottle. The bottle is 1.2 g heavier when it is full. The whole process takes about 3 minutes.

   When the bottle is filled with CO_2, 1800 g tank water without dissolving gas (prepared in step 3) is added slowly to the bottle with the guidance of a glass bar. While adding tank water, we keep mixing to ensure that the mixture is always homogeneous, and that there is no dry cluster in the bottle. The liquid cannot be added at once, otherwise, the air is trapped between the particles. The adding is very slow at first. It takes about 3 minutes of mixing to make the solution homogeneous, and the particles are wet properly. At first, the texture of the solution is just like mud. After adding about a quarter of the liquid, the texture becomes more liquid. After adding the rest of the tank water, a magnetic bar is added for stirring. Similar to step 3, the bottle is put into the vacuum chamber under the pressure of 60 Pa for about 20 minutes. The magnetic stirrer is used to remove the bubbles left.

5. **Setting the lasers.** There are two lasers, one on each side. The laser is fixed on a multi-axis tilt platform. The tilt platform provides accurate rotation on two axes (X-axis and Z-axis) and displacement in one direction (Y-direction). The aluminum profiles structure (Norcan) fixes the tilt platforms which provides the displacement in the other two directions. By adjusting these structures, the two laser sheets overlap each other in the middle of the water tank. The lasers are switched on at least one hour before the formal experiment for warming up.

6. **Setting the back-light.** A 5 W LED light box (RS PRO 136-3720) is placed on the middle of the tank backboard as a backlight. Figure 3.4 shows the size of the LED light box and its spatial location relationships with the tank and the entrance. The light box is fixed on the aluminum profile structures. It is placed 1 cm away from the tank's backboard, to ensure that the water tank is not heated by the light.

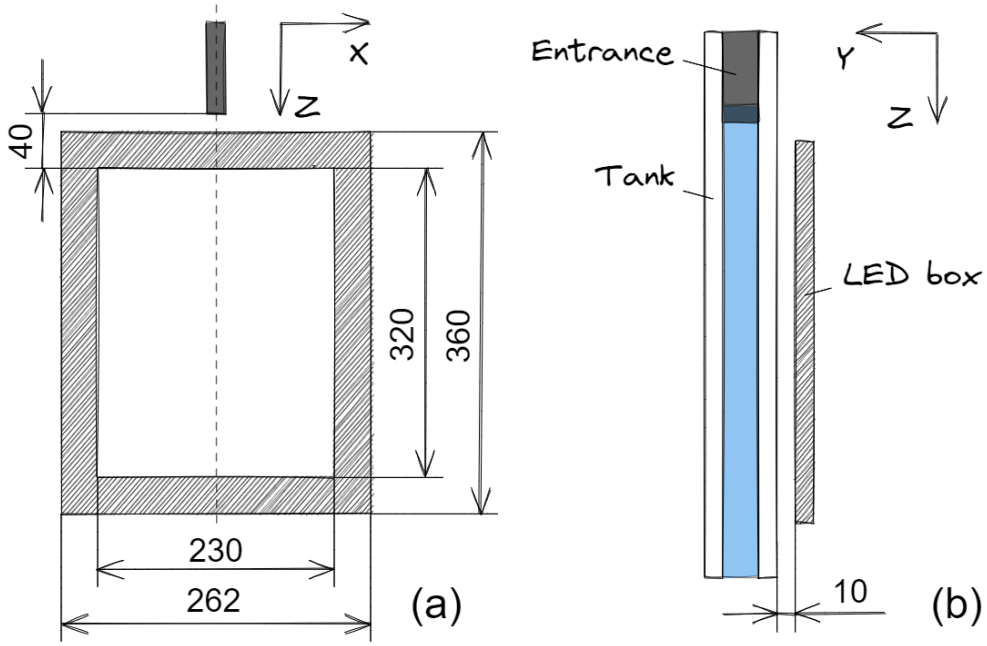

Figure 3.4: The location of the LED light box (RS PRO 136-3720) on the back side of the tank. The sizes are in mm (a) front view; (b) side view.

7. **Setting the camera and its objective.** The camera (UI-3060CP-C-HQ Rev.2) and the ob-

jective (Myutron HS1214V) are placed in front of the tank, about 1.5 m away. The camera is controlled by the computer with uEye Cockpit 4.90. The auto gain control (AGC) for the camera is set as 0 and closed. Otherwise, the AGC will enhance the brightness of the image automatically, which can influence measuring particle concentration. The frame rate is fixed as 10 Hz, but the exposure time is changed for different purposes. The focus of the camera is adjusted after adding tank water.

8. **Preparation of the weight scale.** In order to measure the injection rate, the weight of the solution bottle is monitored by a weight scale (KERN PLJ 6200-2A) with 0.01 g accuracy. As shown in Figure 3.1, the scale is put on the lifting platform and its horizontality is adjusted. A wire (D-sub SC14007) connects the scale to the computer. The weight data from the scale is received on the computer in real time. The lift platform is fixed if the injection is driven by the peristaltic pump. For free-falling injection, the lifting platform is controlled manually with a knob on the lift platform. A wrench is needed to increase the torque to rotate the knob when the solution bottle is full and the lift platform is at the lowest point.

9. **Water bath.** In order to avoid extra thermal effects, the solution bottle is placed in a water bath. The water is tap water which is stored in 10 L buckets for more than 24 hours to reach thermal equilibrium. Its temperature is as same as the tank water. On the top of the scale, a basin with 2 L water at room temperature is placed under the solution bottle. The water in the water bath is changed every 30 minutes during the experiment.

10. **Recycling loop for the solution.** The solution keeps recycling in the circulation tubes which are indicated by orange arrows in Figure 3.1. This recycling avoids particle sedimentation inside the tube before the injection. The impeller of the stirrer (Velp Scientifica LS Overhead Stirrer) is put into the bottle. Its head is below the water surface. The mixing by the stirrer with speed 1.5 to 2 during the injection avoid sedimentation, and make the particle suspension homogeneous. The tubes are connected to the two holes at the bottom

of the solution bottle. The pump is started with its maximum speed for recycling. Most of the air already in the tube is emptied after starting the recycling. There are some bubbles stayed in the valves and connections, which are removed manually by twisting the local part.

11. **Setting of temperature sensors.** Two thermocouples (HSTC-Series) are used to monitor the temperature in the tank and solution bottle. The thermocouples are covered with plastic to avoid contact with water. The one in the tank is fixed at 10 cm below the water surface. The other one is fixed in the solution bottle, close to the outlet. The temperature data is collected through an Arduino card and the corresponding python program and saved in the computer in real-time.

12. **Preparation of the artificial grasses.** As shown in Fig. 3.1, some plastic artificial grass is placed on the tank bottom to minimize the bottom effect from the plume. The artificial grasses are fixed on two 30 cm PMMA bars with wires and tapes. The gap between each grass is about 6 cm. The typical height for the grasses in the tank is about 18 cm. The artificial grasses are cleaned with compressed air and placed in the tank in advance. After adding tank water, the artificial grasses are shaken sufficiently to remove air bubbles stuck on them.

13. **Adding tank water.** Since this experiment is very sensitive to temperature gradients, the convection due to evaporation could influence the experimental results. The tank water is added just before the injection stage. The water is added through a siphon tube. Before adding, the buckets containing tank water are shacked sufficiently to ensure the PIV beads are suspended homogeneously, but not too much to avoid air bubbles. About 10.8L of water is needed to fill the tank.

14. **Removing air in the entrance.** The space between the entrance and three-way valve No.1 is full of air after adding tank water. In order to empty the air here, the recycling loop

is closed with two water stop clips temporarily. The tank and the needle are connected by switching two three-way valves. The water is drawn into the needle until no air is left in the entrance. The recycling is started again, and the whole system is ready for the injection stage. The injection could be started by switching the three-way valve No.1. This step is repeated each time when the tank water is changed.

15. **Experiment.** The entire experiment series in one day takes about 2 to 6 hours (this does not include preparation), including 10 to 30 individual injection runs. The typical process for one individual injection is shown in Figure 3.5. Before starting, the recycling loop runs for more than 10 minutes with the given pump speed, and the water in the tank is at rest.

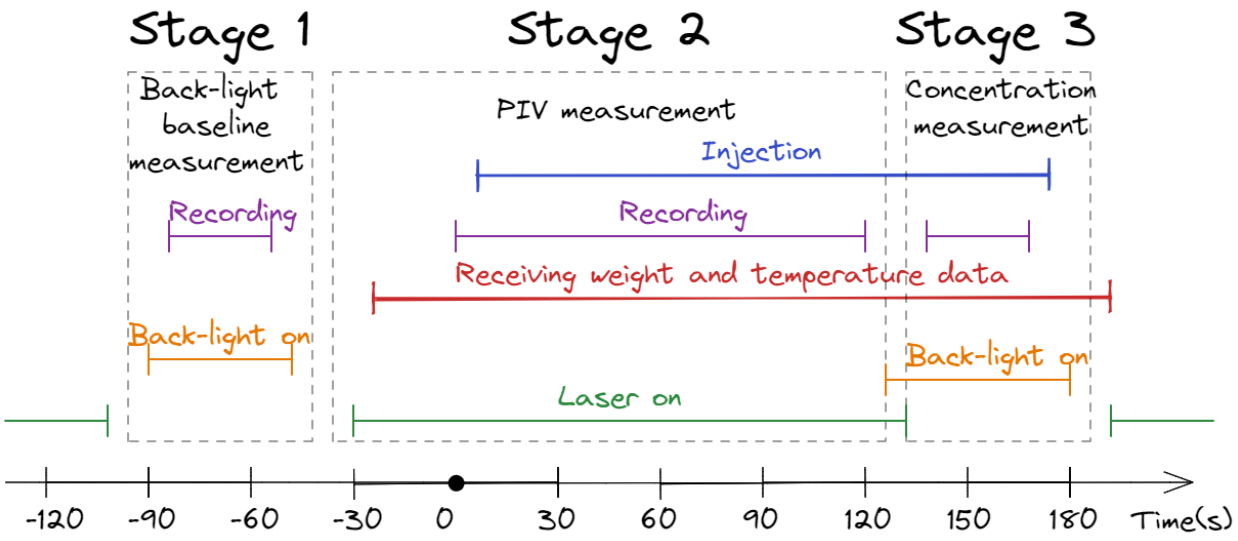

Figure 3.5: Typical experimental process for one individual injection.

The measurement process can be divided into three stages. The first stage is the measurement of the baseline for the backlight. The grey value difference between the baseline and plume image indicates the local particle concentration. The base-line is defined as the average value for 30 s, with frame rate 10 Hz and exposure time 1 ms. The second stage is PIV measurement. The lasers and data-receiving programs are switched on about 30s before the recording. The recording takes 120 s, with frame rate 10 Hz and exposure time 50 ms. It

starts just before the injection. The plume is fully developed after 60 s at most. The injection keeps going when the second stage stops. The third stage, concentration measurement, starts after switching on the backlight, and switching off the lasers. The recording for concentration takes 30 seconds, the camera set is the same as during stage 1. The three-way valve No.1 is switched to stop the injection just after recording.

We use a 1 m and 2 cm thin PMMA stick to mix the tank after the injection. The extra water is drawn out by a needle to ensure the water surface in the tank is just higher than the entrance. The particles left in the entrance keep falling for about 2 minutes. After about 8 minutes, the particles sedimented completely and the tank water became static again. The whole system is ready for the next injection.

After 3 to 4 individual injections, (depending on the injection rate), the water of the tank is changed using a siphon. The artificial grasses are taken out first for cleaning. The particles left at the bottom are cleaned with the siphon. The plastic beads left at the tank bottom are recycled with a sieve at the outlet.

16. **Cleaning.** The experiment is stopped ideally when the water surface of the solution in the solution bottle is lower than the outlet hole. In this situation, the air is entering the tube. The plume is interrupted by the air in the tube.

    The plastic beads remaining in the solution bottle are recycled with a sieve. The artificial grasses are cleaned and dried with compressed air. Since there are some passive mixing-enhancing structures at the entrance, particles may be left in it easily. The three-way valves No.1 and No.2 are switched in order to wash the entrance with the syringe. The solution bottle is filled with fresh water and the pump is running at full speed for more than 10 minutes. After the tubes for the recycling loop are cleaned, every part connected to this loop is disassembled. The tank is emptied with a siphon and washed with tap water by a high-pressure water gun. The particles left at the bottom are also recycled with a sieve.

The dehumidifier (ROHAN0001) is running through the night to dry the whole experiment room to enhance the drying of every part, which maintained the humidity at about 20% in the experiment room. The recycled plastic beads in the sieves are wet. The water between the plastic beads needs natural evaporation for about a week for the next use.

3.2.1.2 Different procedures for one-phase NaCl plume

The dissolved NaCl plume is used for comparison with the plastic beads solution. The dissolved NaCl solution used has the same density as the equivalent density of the plastic bead solution. But the dissolved NaCl solution is homogeneous and one-phase. Here we would like to know whether the solution without particles in it has a similar dynamic behavior to the plastic bead solution, with the same equivalent density.

Using a dissolved NaCl solution means that measuring the velocity field inside of the plume with PIV is possible, because there is no particle in the plume affecting the PIV measurement. Since the solution is transparent, the plume concentration field cannot be measured with backlight. In consequence, the plume is colored with a fluorescent dye, fluorescein ($1.25\,\mathrm{mg\,L^{-1}}$), which is excitated with a violet laser. This technique is also used for concentration measurements in microbursts (Alahyari and Longmire, 1997).

For the dissolved NaCl plume experiment, there are three major differences compared to the plastic beads plume experiment. The solution injected is the salted solution. The backlight is not useful for this plume, and a violet laser is used instead. The experimental part is changed consequently. The details are as follows:

4. **Preparation of the NaCl solution.** The NaCl solution used has a similar density to the plastic beads solution. The density of plastic beads ρ_{plastic} is $1.066\,\mathrm{g\,cm^{-3}}$, and the density of water ρ_w at 21.6 °C is $0.998\,\mathrm{g\,cm^{-3}}$ (ToolBox, 2003). Since the plastic bead mass fraction is 10% in solution, the equivalent density of plastic beads solution is $10\%\rho_{\mathrm{plastic}} + 90\%\rho_w = 1.0048\,\mathrm{g\,cm^{-3}}$. For the NaCl solution, the density is equal to $1.0048\,\mathrm{g\,cm^{-3}}$ when the NaCl

weight concentration is 1% at 21.6 °C (Rowland, 2021). 2000 g of NaCl solution are prepared once. We measure the room and solution temperatures before and after the preparation. A 2 L solution bottle is put on the scale. Two water stop clamps are used to close the bottle temperately. 20 g NaCl, 50 g saturated fluorescein solution (0.05 g per 100 mL in 20 °C) and 1930 g tank water (with PIV beads) are added and mixed with a magnetic stirrer for at least 10 minutes. The density of the NaCl solution prepared is measured with a pycnometer, which is 1.0045 g cm^{-3}.

6. **Setting the violet laser.** For fluorescein, the peak of excitation occurs at 494 nm and the peak of emission at 521 nm (Minta, Kao, and Tsien, 1989). A violet laser (Q-BAIHE Laser Line Module, 405 nm, 50 mW) is used to excite the fluorescein in the plume. Similar to the green lasers, the violet laser is fixed on a multi-Axis tilt platform. With five degrees of freedom, the violet laser sheet overlaps with green laser sheets in the middle of the tank. The laser is switched on at least one hour before the formal experiment for warming up.

15. **Experiment.** The major process is similar to what is sketched in Figure 3.5, but the back-light is changed into the violet laser. Due to chromatic aberration, the focusing plane for different colors is different. The camera cannot get focus both in violet laser and green laser. Fortunately, the peak emission for fluorescein is at 521 nm, similar to the green lasers. There is thus no need to adjust the focus after switching the laser.

    Another difference compared to the plastic bead plume experiment is that the tank water is changed after each injection. Otherwise, the whole tank is colored with fluorescein.

3.2.1.3 Different procedures for butyramide

Butyramide has a similar density to plastic beads. Butyramide is soluble in water, so it needs to be stored in its saturated solution before injection. Moreover, butyramide is relatively expensive, about 400 euros per kilogram, and the supply is limited in the world. We recycle it as much as

possible during the experiment. The major difference with the plastic bead experiment is related to the preparation of the mixed solution.

2. **Preparation of butyramide particles.** The butyramide particles have to be prepared just before the experiment. Due to recrystallization, the shape of the particle may change after 6 hours. Large butyramide crystals are churned with a blender (Moulinex DPA141). 120 g of large butyramide crystals are churned for about 40 s, with a 10 s gap in middle to avoid overheating of the blender.

   Three sieves are used for separating the butyramide particles. From top to bottom, the size of sieves are 0.400 mm, 0.200 mm, and 0.140 mm. The butyramide particles between 0.140 mm to 0.200 mm are used during the experiment. A Retsch sieve shaker is used for separation during 60 minutes with strength 30. Since the butyramide particles could stick together and block the sieves, about 20 g of particles between 0.140 mm to 0.200 mm can be prepared at a time. The sieves are cleaned with compressed air after collecting the butyramide particles. This step is repeated 3 to 5 times to have enough butyramide for one day's experiment. When a sufficient amount of butyramide particles is collected, the bottle of dry butyramide is placed under CO_2 environment to replace the air trapped between particles with CO_2. The particles whose size is below 0.140 mm are added to the over-saturated solution bottle. The particles whose size above 0.200 mm are stored for the next time.

3. **Preparation of saturated butyramide solution without dissolving gas.** One bottle of over-saturated butyramide solution is kept at room temperature. The butyramide particles below 0.140 mm, remaining mixed solution, deionized water, and other butyramide leftovers are added into this bottle. There are always some butyramide crystals floating in the bottle, which ensures that the solution is over-saturated.

   The saturated butyramide solution is obtained by filtering the over-saturated butyramide

solution. The room temperature is measured before and after the preparation. Two layers of filter are used. The upper one is a steel grid of 1 mm, which can separate large crystals. The other one below is a filter paper (VWR No.516-0299, 303), to remove small particles and dust ($> 5 \sim 13\,\mu m$). About 800 g of cleared saturated butyramide solution is prepared at once for a one-day experiment. The butyramide crystals left on the filters are recycled into the over-saturated bottle.

Similar to the plastic bead plume, the saturated butyramide solution is put into the vacuum chamber with a magnetic mixer. The pressure inside of the chamber is reduced into 60 Pa for about 20 minutes. Below the vacuum chamber is the magnetic stirrer. It is stirring the liquid for removing air bubbles at the speed of 1 to 1.5.

4. **Preparation of the mixed solution.** Since the butyramide particles can block the sieves, the amount that can be prepared per day is limited. For about 100 g of particles, it takes about 5 hours (20 g for one hour sieve shaking). Typically, we prepare 800 mL mixed solution for a one-day experiment. It means 80 g of butyramide particles between 0.140 mm to 0.200 mm and 720 g of saturated butyramide solution without dissolved gas. The preparation steps are similar to Section 3.2.1.1, item 4. Due to the hydrophobicity of the butyramide particles, some air is trapped between butyramide particles. To avoid this, the dry butyramide particles are placed in the CO_2 atmosphere for 30 minutes before mixing.

3.2.1.4 Different procedures for KNO_3

KNO_3 is another reference for butyramide. KNO_3 is soluble in water. Unlike butyramide, KNO_3 significantly increases the liquid density after dissolving for about $0.18\,g\,cm^{-3}$ (25 °C). This extra buoyancy effect will modify the dynamic of the plume.

Since the mixture of KNO_3 particles and saturated KNO_3 solution is injected into the tank, the density of tank water is adjusted to be equal to the density of saturated KNO_3 solution. This

ensures that the buoyancy force in the plume only comes from the KNO_3 particles, like in the case of the plastic beads plume. The density of tank water is adjusted with NaCl. NaCl is acid-neutral, and it does not influence the dissolving of KNO_3 in water in a lower concentration. The density of saturated NaCl solution is larger than the density of saturated KNO_3 solution at room temperature. So it is possible to prepare a NaCl solution whose density is equal to that of saturated KNO_3 solution.

1. **Preparation of tank water.** According to the website (Rowland, 2021), the density of saturated KNO_3 solution at room temperature is about $1.17\,\mathrm{g\,cm^{-3}}$. In order to have a NaCl solution with similar density, the mass fraction of NaCl must be about 24.3%. In a 10 L bucket, 10 kg tank water is prepared, which is about 8.47 L. Because of the volume limitation, the salt tablets and clear water for 10 L NaCl water cannot be added into a 10 L bucket at once. For 10 kg tank water, 2.43 kg NaCl is mixed with 7.57 kg water. 0.42 g of 50 µm PIV beads is also added with 0.42 g surfactant. The PIV beads concentration is $0.05\,\mathrm{g\,L^{-1}}$, same as the tank water prepared in Section 3.2.1.1 step 1.

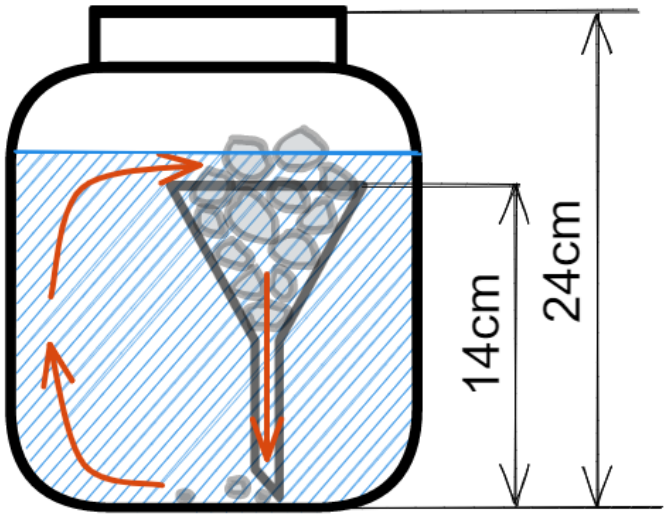

Figure 3.6: Enhancing the dissolution of salt tablets with funnel.

If the salt tablets are simply piled at the bottom of the bucket, only with diffusion, the salt cannot dissolve within 72 hours. As shown in Figure 3.6, in order to enhance this

dissolving process, a funnel is placed in the bucket, with all salt tablets in it. The saturated NaCl solution leaves from the outlet of the funnel. The dissolving of salt at a higher place leads to convection by density difference. With this setup, most of the salt dissolves within 6 hours. Depending on the outlet diameter of the funnel, there is a bit of salt left at the bottom. The electric overhead stirrer is used for finishing mixing for about 40 minutes with a speed of 2 to 3. It helps the dissolution of the remainning solid salt and makes the solution homogeneous. About 50 L tank water is prepared for replacement.

2. **Preparation of KNO_3 particles.** The preparation of KNO_3 particles is similar to the one of butyramide, in Section 3.2.1.3 step 2.

3. **Preparation of saturated KNO_3 solution without dissolving air.** The preparation of saturated KNO_3 solution without dissolving air is similar with butyramide, in Section 3.2.1.3 step 3.

4. **Preparation of the mixed solution.** The preparation of the mixed solution is similar to the one of butyramide, in Section 3.2.1.3 step 4. For plastic beads and butyramide, the density of particles is almost equal to water, slightly heavier. It is not required to distinguish mass fraction and volume fraction. For KNO_3 experiment, the mixed solution is the mixture of 80 g of particles and 720 g of saturated KNO_3 solution. The density of KNO_3 particle (2.10 g cm^{-3}) is much heavier than its saturated solution (1.18 g cm^{-3}), compared with butyramide. The intensity of the stirrer is thus chosen higher for KNO_3.

3.2.2 Solution preparation

Removing the bubbles in the mixed solution is a major challenge in the experimental preparation. In the experiment, the solution injected is a mixture of 10% particles and 90% liquid in mass. In order to minimize the influence of the solution during injection, the mass fraction of the particle should be as large as possible. The mass fraction of the particle in the solution is

set as 10% in the experiment. We try to use a solution with a 15% volume fraction of particles in the experiment. Unfortunately, the particles always block the tube in the peristaltic pump. In consequence, we used the solution with a 10% volume fraction of particles in the following experiments.

The dynamics and falling of the plume are driven by buoyancy due to the particles. So the experiment is sensitive to the bubbles remaining in the solution. During the preparation, CO_2 is used to minimize the number of bubbles. The mixing process is handled under CO_2 atmosphere. It means that in the mixed solution, the air bubbles which are stuck on particles are replaced by CO_2 bubbles. The solubility of O_2 and N_2 in water is $7.6\,\mathrm{mg\,L^{-1}}$ and $20\,\mathrm{mg\,L^{-1}}$ at 100 kPa, 20 °C (Emerson et al., 1999). But the solubility of CO_2 in water is $1.45\,\mathrm{g\,L^{-1}}$ at 100 kPa, 25 °C (Enick and Klara, 1990). As a polar molecule, CO_2 is much more soluble in water compared to O_2 or N_2.

It is difficult to estimate the total volume of the bubbles stuck on the particles directly. We assume that the maximum volume of the gas remaining in the solution is not larger than the volume of the particles in the solution. The particle volume fraction is 10% (except KNO_3 solution for which the particle volume fraction is lower). Considering the density of CO_2, ρ_{CO_2} is $1.87\,\mathrm{g\,L^{-1}}$ at 100 kPa and 15 °C, the maximum concentration C_{CO_2} of CO_2 which needs to be dissolved into the solution is:

$$C_{CO_2} = \rho_{CO_2} \times \frac{V_{(\mathrm{gas})}}{V_{(\mathrm{liquid})}} = 1.977\,\mathrm{g\,L^{-1}} \times \frac{1}{9} \approx 0.220\,\mathrm{g\,L^{-1}} \tag{3.1}$$

This concentration is mush smaller than the maximum solubility of CO_2 in water ($1.45\,\mathrm{g\,L^{-1}}$ at 100 kPa, 25 °C). The bubbles in the solution are furthermore removed by the vacuum pump. So, it is efficient to use CO_2 to minimize the number of bubbles in the solution.

In the discussion above, two points are not considered. One is the solubility changing with a combined effect of several solutes. And the other one is the dissolution time scale of CO_2 in water. Since the CO_2 concentration which needs to be dissolved is over-estimated and still much smaller than the maximum solubility, using CO_2 to reduce the bubbles in the solution is reasonable.

3.2.3 Injection method

In order to have particles sedimenting in quiescent water, the easiest way is to pour the particles directly from the top of the tank. Consequently, the particles sediment into the tank and form a plume. Since the density of the particles used is just a bit heavier than water, and the particle is hydrophobic. The particles cannot get into the tank with gravity properly.

In Figure. 3.7(a), dry butyramide particles are poured into a 28 cm × 28 cm × 14 cm water tank through a 3 cm × 3 cm entrance. The injection rate is controlled by a conveyor belt above to remain constant, $0.06\,\mathrm{g\,s^{-1}}$. After the pouring starts, as shown in Figure. 3.7(b) the particles at first stay on the water surface due to surface tension. While the pouring goes on, the following particles accumulate on the previous particles, as illustrated in Figure. 3.7(c). When the particle accumulation becomes heavy enough, a big particle cluster falls into the tank, Figure. 3.7(d).

This try indicates that due to the particle density just above 1 and the effect of the surface tension, one dry particle cannot get into the tank smoothly with gravity. The injection is not continuous, but is influenced by big particle clusters accumulating on the water surface.

3.2.3.1 Mixing structure

3.2.4 Water surface raising

Due to the solution injected, the water surface in the tank raises during the experiment. If only particles are injected, the raising of the water surface is 10 times smaller than injecting with 10% particle solution. This raising leads to a background vertical velocity. If this background vertical velocity is larger than the particle sediment velocity, the particles cannot sediment properly.

The maximum injection rate is about $I_{\max} = 2\,\mathrm{g\,s^{-1}}$. If we consider that the velocity field is homogeneous, the maximum vertical background velocity $w_{\text{background}}$ is:

$$w_{\text{background}} = \frac{I_{\max}}{\rho L D} = \frac{2\,\mathrm{g\,s^{-1}}}{1\,\mathrm{g\,cm^{-3}} \times 1000\,\mathrm{mm} \times 18\,\mathrm{mm}} \approx 0.11\,\mathrm{mm\,s^{-1}} \tag{3.2}$$

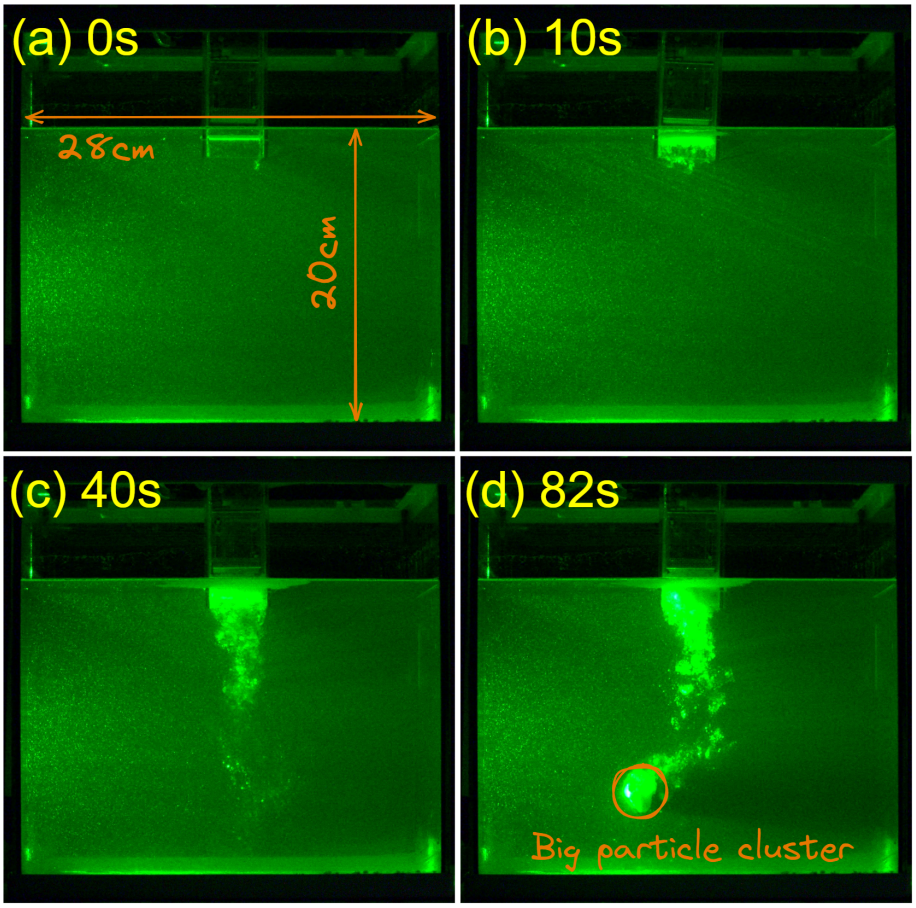

Figure 3.7: Direct pouring the butyramide particle on the water surface in a 28 cm × 28 cm × 14 cm tank through a 3 cm × 3 cm entrance. The particle injection rate is 0.06 g s^{-1}. (a) 0 s; (b) 10 s; (c) 40 s; (d) 82 s.

where ρ is the solution density, which can be approximated by the water density, L is the length of the tank, and D is the width of the tank.

For the single particle falling velocity, the Stokes drag force is balanced with gravity. The falling velocity for a single particle $w_{\text{single}} \approx 0.70\,\text{mm}\,\text{s}^{-1}$ in $140\,\mu\text{m}diameter$, which is about 7 times of $w_{\text{background}}$. It means that even the smallest particle can sediment properly (more calculation is shown in Section 2.2).

As shown in Figure 3.5, the typical injection duration is about 3 minutes. The maximum water

raise in the tank is thus:

$$w_{\text{background}} \times 180\,\text{s} = 0.11\,\text{mm}\,\text{s}^{-1} \times 180\,\text{s} = 19.8\text{mm} \tag{3.3}$$

The distance between the entrance and the top of the tank is about 40 mm, so the water cannot overflow from the tank within one injection.

3.3 Conclusion

An experimental setup to investigate the continuous sedimentation of soluble particles inside of quiescent water is designed and built (Figure 3.1). Some basic parameters for the experiment are shown in Table 3.2. The particles are pre-mixed with their saturated solution and injected into the tank with pump or gravity, and form a particle plume. Some artificial grasses are placed at the bottom of the tank to slow down the plume going through, extending the available measurement time of the system. Two lasers are placed on the sides of the tank for PIV measurement. A constant backlight is placed behind the tank for plume concentration measurement.

Name	Value	Unit	Note
Tank height	600	mm	
Tank length	1000	mm	
Tank width	18	mm	
Entrance width	2	mm	along x direction
Entrance length	16	mm	along y direction
Particle diameter	140 - 200	µm	
Particle fraction	10	%	
Pump injection rate	0.1 - 1.0	$\text{g}\,\text{s}^{-1}$	0.1 - 1.1 for KNO_3
Gravity injection rate	0.6 - 2.5	$\text{g}\,\text{s}^{-1}$	
Back-light height	320	mm	
Back-light width	230	mm	

Table 3.2: Basic parameters for the experiment

Four kinds of solutions are used. Three of them are the mixture of particles and their saturated

solution, plastic bead, butyramide, and KNO_3 (the plastic beads are mixed with water). The last one is a one-phase NaCl solution, which has the same equivalent density as the plastic bead solution.

The major difficulty of the experiment is reducing the number of air bubbles left in the mixed solution. We use a vacuum pump to remove the bubbles in the mixed solution, which is sufficient for the plastic beads. For butyramide, since the particles are hydrophobic and crystalline, some air is trapped between the particles. In order to overcome this problem, the whole preparation process has been done in a CO_2 environment. Compared to air, it is much easier for CO_2 to dissolve in water.

For the NaCl solution, the laser on the side is replaced with a violet laser to excite the fluorescein in the plume. For KNO_3, to avoid extra buoyancy coming from the heavy saturated KNO_3 solution, the density of the water in the tank is adjusted by adding a certain amount of NaCl. When KNO_3 dissolved, it increases the density of surrounding.

4 | Plume theory

In this chapter, we discuss models for two-dimensional buoyancy plumes. In Section 4.1, the governing equations are rewritten for considering the particles in the plume. Some scalings are calculated and will be compared to experimental results in Section 5.2. Then we present the classical framework by B R Morton et al., 1956 and B. R. Morton, 1971, below referred to as the MTT model (Section 4.2). The model is adapted for the 2D geometry situation, which corresponds to our experimental configuration (Chapter 3 and 5). In Section 4.3, we develop a model of entrainment in turbulent plane plumes, where a mixing length approach is used to describe momentum and buoyancy mixing, and from which analytical expressions for transverse profiles can be derived.

4.1 Basic balance equations for top-hat profile

We consider a turbulent plume that develops from an infinitely long slender source of buoyancy flux, into an initially quiescent and homogeneous environment of uniform density. The plume is subjected to the gravitational acceleration g. Here we use the top hat picture, all the variables are constant inside the plume. For a top hat plume profile, similar to B R Morton et al., 1956, the 'plume fluid' is located in this region $|x| < b(z)$, and the 'ambient fluid' is outside of it ($|x| > b(z)$).

The buoyancy for classical plumes comes from the density difference between the ambient

fluid and the plume fluid. For the plume we are interested in, the plume fluid is not a one-phase solution. It is a mixture of particles and liquid, the so-called 'particle plume'. Such plumes have been investigated in recent years (Bordoloi et al., 2020, McConnochie, Cenedese, and McElwaine, 2021). Especially for the plastic bead plumes investigated in Section 5.2, the liquid has the same density as the ambient fluid. The buoyancy of the plume comes from the particles suspended in the plume.

In order to obtain the behaviors of the plume half width b, vertical velocity u_p and buoyancy forces $\tilde{g}$ acting on the plume fluid as functions of height, we write mass, momentum, and buoyancy balances for a control volume in a slice between altitudes z and $z + \mathrm{d}z$ and of dimension $2b$ in the x direction. This is the 'top hat' plume approach, similar to B R Morton et al., 1956. We assume a steady state. The control volume for the following discussion is shown in Figure 4.1.

4.1.1 Mass balance

During the time interval $\mathrm{d}t$, the volume of plume fluid entering the control volume from the top is $2b(z)u_p(z)\mathrm{d}t$, where u_p is the vertical plume fluid velocity. Similarly, what goes out at the bottom of this volume is $2b(z + \mathrm{d}z)u_p(z + \mathrm{d}z)\mathrm{d}t$. Some ambient fluid also enters the volume from the left and right sides: a volume of $2\mathrm{d}zu_e dt$, where u_e is called the entrainment velocity (a horizontal velocity). We take it as a positive quantity here, even if it goes towards the center of the plume. Gathering these different contributions, the mass balance writes as:

$$2b(z + \mathrm{d}z)u_p(z + \mathrm{d}z)\mathrm{d}t = 2b(z)u_p(z)\mathrm{d}t + 2\mathrm{d}zu_e\mathrm{d}t \tag{4.1}$$

that is

$$\frac{\mathrm{d}}{\mathrm{d}z}\left(bu_p\right) = u_e \tag{4.2}$$

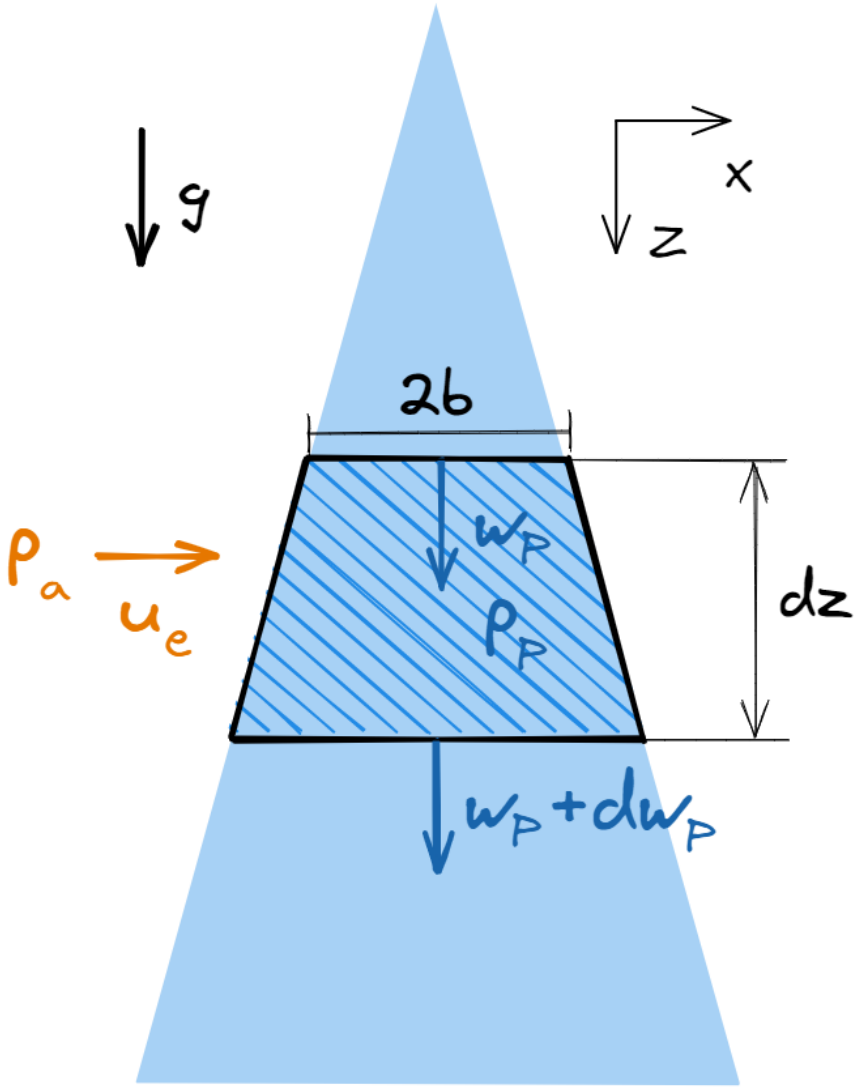

Figure 4.1: The 'top-hat' control volume schematic for plume.

4.1.2 Vertical momentum balance.

During the time interval $\mathrm{d}t$, the vertical momentum of plume fluid entering the control volume from the top is $2b(z)u_p(z)\mathrm{d}t\rho_p u_p(z)$, where ρ_p is the mass density of the plume fluid. Similarly, the vertical momentum of plume fluid getting out of the control volume at the bottom is $2b(z+\mathrm{d}z)u_p(z+\mathrm{d}z)dt\rho_p u_p(z+\mathrm{d}z)$. Because the plume fluid is heavier than the ambient fluid ($\rho_p > \rho_a$), the gravity field gives a vertical force $2b(z)\mathrm{d}z(\rho_p - \rho_a)g$, where g is the gravity acceleration constant. Finally, the vertical force balance writes:

$$\frac{1}{\mathrm{d}t}\left[2b(z+\mathrm{d}z)u_p(z+\mathrm{d}z)\mathrm{d}t\rho_p u_p(z+\mathrm{d}z) - 2b(z)u_p(z)\mathrm{d}t\rho_p u_p(z)\right] = 2b(z)\mathrm{d}z(\rho_p - \rho_a)g \tag{4.3}$$

that is

$$\frac{\mathrm{d}}{\mathrm{d}z}\left(b\rho_p u_p^2\right) = b(\rho_p - \rho_a)g \tag{4.4}$$

A classical approximation here is the Boussinesq assumption, which assumes that ρ_p can be replaced by ρ_a in the left-hand side term of the above equation, so that one obtains

$$\frac{\mathrm{d}}{\mathrm{d}z}\left(bu_p^2\right) = b\tilde{g} \tag{4.5}$$

where $\tilde{g} \equiv g(\rho_p - \rho_a)/\rho_a$ is the buoyancy-reduced gravity.

4.1.3 Buoyancy balance

In order to derive that third balance, it is helpful to think of the plume as being a suspension of particles. As we assume that there is no density difference between the ambient fluid and plume fluid, the buoyancy of the plume only comes from the suspended particles. What is usually presented as buoyancy conservation is here equivalent to the conservation of particle number, which is easier to understand.

We assume that the particles have a mass density ρ_s and all equal volume V_s (or equal diameter d_s). We denote by N their number per unit volume. We consider a volume V of the plume fluid. There are NV particles in this volume, and $NV\rho_s V_s$ their corresponding mass (or NVV_s the corresponding volume they occupy inside V). One can then compute the plume mass density as

$$\rho_p = \frac{NV\rho_s V_s + \rho_a(V - NVV_s)}{V} = \rho_a + NV_s(\rho_s - \rho_a) \tag{4.6}$$

where the fluid inside which the particles are suspended is the same (or has the same density) as the ambient fluid. The link between the buoyancy-reduced gravity and the particle concentration is thus

$$\tilde{g} = gNV_s\frac{\rho_s - \rho_a}{\rho_a} \tag{4.7}$$

Assuming these particles do not dissolve, one can now derive the balance associated with the conservation of their number. During the time interval $\mathrm{d}t$, the number of particles entering the control volume from the top is $N(z)2b(z)u_p(z)\mathrm{d}t$. Similarly, the number of particles that goes out at the bottom of this volume is $N(z+\mathrm{d}z)2b(z+\mathrm{d}z)u_p(z+\mathrm{d}z)\mathrm{d}t$. Nothing enters from the sides, as the ambient fluid is clear of particles. The corresponding balance thus writes:

$$N(z+\mathrm{d}z)2b(z+\mathrm{d}z)u_p(z+\mathrm{d}z)\mathrm{d}t = N(z)2b(z)u_p(z)\mathrm{d}t \tag{4.8}$$

that is

$$\frac{\mathrm{d}}{\mathrm{d}z}\left(bNu_p\right) = 0 \tag{4.9}$$

or equivalently, in terms of buoyancy, using the linear relationship between N and $\tilde{g}$, Equation 4.7,

$$\frac{\mathrm{d}}{\mathrm{d}z}\left(b\tilde{g}u_p\right) = 0 \tag{4.10}$$

Equations 4.2, 4.5 and 4.10 are the 2D-equivalent balance equations of B R Morton et al., 1956

(for an un-stratified environment), when one further assumes the closure $u_e = \alpha u_p$, where α is a constant on the order of 0.1. More details about this closure are discussed in Section .

4.2 Framework by Morton

In their pioneering work on buoyancy-driven flows, Morton proposed a model to describe the vertical variations of volume Q, momentum M, and buoyancy B fluxes. With these quantities, it is possible to derive expressions for the plume half width b, vertical velocity u_p and buoyancy forces $\tilde{g}$ acting on the plume fluid as functions of height away from the plume source. The MTT model is based on a 3D axisymmetric plume, which we adapt here to the two-dimensional case corresponding to our experimental framework.

For top hat profiles, these fluxes write as:

$$Q = \int_{-\infty}^{\infty} u_p \mathrm{d}x = 2bu_p \tag{4.11}$$

$$M = \int_{-\infty}^{\infty} {u_p}^2 \mathrm{d}x = 2bu_p^2 \tag{4.12}$$

$$B = \int_{-\infty}^{\infty} u_p \tilde{g} \mathrm{d}x = 2b\tilde{g}u_p \tag{4.13}$$

Conversely, the expressions for the plume half width b, vertical velocity u_p and buoyancy forces $\tilde{g}$ write as:

$$b = \frac{Q^2}{2M} \tag{4.14}$$

$$u_p = \frac{M}{Q} \tag{4.15}$$

$$\tilde{g} = \frac{B}{Q} \tag{4.16}$$

With these fluxes, for an unstratified environment, the balance equations write as:

$$\frac{dQ}{dz} = 2u_e \qquad \text{(Mass)} \tag{4.17}$$

$$\frac{dM}{dz} = \frac{FQ}{M} \qquad \text{(Momentum)} \tag{4.18}$$

$$\frac{dB}{dz} = 0 \qquad \text{(Buoyancy)} \tag{4.19}$$

To close Equation 4.17 to 4.19, one further closure is needed. MTT model provides a simple but powerful entrainment assumption (see J S Turner, 1986 for a detailed view),

$$\alpha = \frac{u_e}{u_p} \tag{4.20}$$

where the entrainment coefficient α is the proportionality constant relating the entrainment velocity u_e at the edge of the plume to the vertical velocity u_p within the plume. α is a constant on the order of 0.1, which has been measured by many researchers (Parker et al., 2020, Richardson and Gary R. Hunt, 2022). This assumption is also used in many plume model works based on MTT approach. Baines and J. S. Turner, 1969 considered the continuous convection from small sources of buoyancy in a bounded region. They got an asymptotic solution for a stably stratified environment. Paillat and Kaminski, 2014a developed a theoretical model that relates the entrainment coefficient α to the local Richardson number and that explains enhanced entrainment in plumes by the contribution of buoyancy. Paillat and Kaminski, 2014b discuss the relationship between α and the distance from the source under different Reynolds numbers.

We have a simple power-law solution of the flux equations, which corresponds to a self-similar plume (Caulfield and Woods, 1995), as observed in experiments. The plume profile half width b, middle line vertical velocity u_p, and middle line buoyancy $\tilde{g}$ of a turbulent plume from a

line source can be expressed as in the 2D case,

$$b \sim z, \tag{4.21}$$

$$u_p \sim B^{1/3}, \tag{4.22}$$

$$\tilde{g} \sim B^{2/3} z^{-1}. \tag{4.23}$$

The plume half width b is proportional to height, and the plume middle line vertical velocity u_p is independent of z. Considering the closure $u_e = \alpha u_p$, it means the entrainment velocity is constant along z direction, which is indeed observed in the non-dissolved particle plume experiment (Figure 5.13).

4.3 Mixing length approach for two-dimensional plumes

The MTT model provides an interesting framework for buoyancy-driven plumes. The entrainment coefficient α plays a key role in boundary conditions on the side of the plume. We derive here a more general solution for the two-dimensional plumes based on Reynolds-Averaged Navier–Stokes equations, where the entrainment phenomenology is described by a mixing length approach rather than a boundary condition on the side of the plume. We first write the governing equations and then look for self-similar solutions.

4.3.1 Governing equations

Here again, we consider a two-dimensional system. Coordinate z is vertical, oriented downwards. x is transverse. Some heavy fluid is put at the origin $x = z = 0$, which will go down forming a plume. The origin is considered a source of buoyancy.

We assume that the average plume is the solution of the steady-state equations. We work under the assumption that the variations along x are stronger than those along z ($\partial_x \gg \partial_z$). We

also make the Boussinesq assumption that the fluid density can be taken as a constant ρ_a, except in front of the gravity term in the momentum equation. Taking the hydrostatic term out of the pressure $\rho_a g z$, the mass, and vertical momentum balance equations write:

$$\partial_x u_x + \partial_z u_z = 0, \tag{4.24}$$

$$u_x \partial_x u_z + u_z \partial_z u_z = \tilde{g} + \partial_x \left(\nu \partial_x u_z \right), \tag{4.25}$$

where we have introduced the buoyancy reduced gravity $\tilde{g} = g(\rho/\rho_a - 1)$, ν is the viscosity.

Finally, $\tilde{g}$ follows an advection-diffusion equation, which we write

$$u_x \partial_x \tilde{g} + u_z \partial_z \tilde{g} = \partial_x \left(D \partial_x \tilde{g} \right), \tag{4.26}$$

where D is the diffusion coefficient.

A general property of the solution of these equations is that the buoyancy vertical flux is conserved (the particle number flux is conserved). Integrating over the x axis Equation 4.26 under the assumption that $\tilde{g}$ vanishes when $x \longrightarrow \pm\infty$, which is consistent with the picture of a localized plume profile, one obtains that

$$B = \int_{-\infty}^{\infty} \tilde{g} u_z \mathrm{d}x \tag{4.27}$$

is a constant independent of z.

4.3.2 Turbulent viscosity and mixing coefficients

We focus on the turbulent case, for which closures for ν and D are required. The concept of mixing length approach is used (Guyon et al., 2015). We take here an eddy viscosity of the form:

$$\nu = \sigma B^{1/3} \mathcal{N} \left(\frac{x}{\sigma} \right), \tag{4.28}$$

where $\sigma(z)$ is the plume width. With this choice, the mixing length is enforced to be the plume width, and the velocity scale is controlled by the buoyancy vertical flux ($B^{1/3}$ has the dimension of a velocity). The self-similar function $\mathcal{N}$ does not provide any additional scale and will be related to specific velocity and buoyancy profiles.

Similarly, we take for the diffusion coefficient the simple choice:

$$D = \frac{1}{\mathcal{S}}\,\nu, \tag{4.29}$$

where $\mathcal{S}$ is the turbulent Schmidt number, which we take here as a constant of order unity. In other words, momentum and buoyancy are mixed by the same turbulent eddies. Gualtieri et al., 2017 collected literature on the parameterization of the turbulent Schmidt number. For the water system, the vast majority of the values are found between 0.5 and 1.

4.3.3 A self-similar solution

As evidenced by Guillaume, Edouard, and Stephen, 2006, for the plume in the experiment, a certain distance downstream is necessary to reach the self-similar profile. We only consider the part where the plume is fully developed. We introduce the usual stream function ψ

$$u_x = -\partial_z \psi, \tag{4.30}$$

$$u_z = \partial_x \psi, \tag{4.31}$$

so that the incompressibility condition in Equation 4.24 is automatically verified.

We look for a self-similar solution for ψ and $\tilde{g}$. Following Morton's scalings, Equation 4.21 to 4.23 (B R Morton et al., 1956), the plume width must here increase linearly with z, and the

buoyancy must decrease as $1/z$. We then write

$$\sigma(z) = \lambda z, \tag{4.32}$$

$$\psi(x,z) = B^{1/3}\sigma(z)\, f\left(\frac{x}{\sigma(z)}\right), \tag{4.33}$$

$$\tilde{g}(x,z) = B^{2/3}\frac{1}{\sigma(z)}\, h\left(\frac{x}{\sigma(z)}\right), \tag{4.34}$$

where λ is a positive dimensionless constant and the factors $B^{1/3}$ and $B^{2/3}$ ensure the correct dimensionality for ψ and $\tilde{g}$, respectively. $\xi = x/\sigma$ is the scaling variable of the scaling profiles f and h.

The corresponding velocity components are

$$u_x = -B^{1/3}\lambda[f(\xi) - \xi f'(\xi)], \tag{4.35}$$

$$u_z = B^{1/3} f'(\xi). \tag{4.36}$$

As discussed above, this form of the solution shows a vertical velocity at the plume center independent of z and proportional to $B^{1/3}$.

The boundary conditions for the functions f and h must be the following: f' and h (as well as their higher derivatives) vanish when $\xi \to \pm\infty$, associated with a localized plume; for symmetry reasons, $f(0) = 0$, $f''(0) = 0$ and $h'(0) = 0$, associated with a vanishing horizontal velocity as well as flat profiles of the vertical velocity and the buoyancy at the center.

The conservation of the buoyancy vertical flux writes as:

$$B = \int_{-\infty}^{\infty} \tilde{g} u_z \mathrm{d}x = \int_{-\infty}^{\infty} B^{2/3} h(\xi) B^{1/3} f'(\xi) \mathrm{d}\xi \tag{4.37}$$

hence the normalization condition:

$$\int_{-\infty}^{\infty} h(\xi) f'(\xi) d\xi = 1. \tag{4.38}$$

Finally, we can see that u_x tends to infinity to $-B^{1/3}\lambda f(\infty)$, which will allow us to define the plume entrainement velocity u_e, connecting with the entrainment coefficient α introduced in B R Morton et al., 1956 and many followers (Scase et al., 2007, Richardson and Gary R. Hunt, 2022). In our framework, the expression about $\alpha = u_x(\infty)/u_z(0) = \lambda f(\infty)/f'(0)$.

Now, we can derive the differential equations coupling profile f and h. In order to solve them, the first one is the momentum equation (4.25), whose left-hand side terms are

$$u_x \partial_x u_z = -B^{2/3} \frac{1}{z} (f - \xi f') f'', \tag{4.39}$$

$$u_z \partial_z u_z = -B^{2/3} \frac{1}{z} \xi f' f'', \tag{4.40}$$

hence their sum:

$$u_x \partial_x u_z + u_z \partial_z u_z = -B^{2/3} \frac{1}{z} f f''. \tag{4.41}$$

The stress term on the right-hand side is

$$\partial_x \left(\nu \partial_x u_z \right) = B^{2/3} \frac{1}{\lambda z} (\mathcal{N} f'')'. \tag{4.42}$$

Combined two equations above we have:

$$\lambda f f'' + h + (\mathcal{N} f'')' = 0. \tag{4.43}$$

The second one about profile f and h comes from the buoyancy equation (4.26), whose left

hand side are

$$u_x \partial_x \tilde{g} = -B \frac{1}{\lambda z^2} (f - \xi f') h', \tag{4.44}$$

$$u_z \partial_z \tilde{g} = -B \frac{1}{\lambda z^2} (h + \xi h') f', \tag{4.45}$$

hence their sum:

$$u_x \partial_x \tilde{g} + u_z \partial_z \tilde{g} = -B \frac{1}{\lambda z^2} (fh)'. \tag{4.46}$$

On the right-hand side, the diffusion term reads:

$$\partial_x \left(D \partial_x \tilde{g} \right) = \frac{B}{\mathcal{S}} \frac{1}{\lambda^2 z^2} (\mathcal{N} h')' \tag{4.47}$$

This finally gives,

$$\lambda (fh)' + \frac{1}{\mathcal{S}} (\mathcal{N} h')' = 0, \tag{4.48}$$

i.e. integrated once and slightly rearranged:

$$\mathcal{S} \lambda f h + \mathcal{N} h' = 0. \tag{4.49}$$

Typically, we should define a suitable mixing function $\mathcal{N}$ to have the expressions of f and h, but assuming the function f is known brings a lot of convenience during the calculation. Let's consider the case where we know (e.g. by measurements) the velocity profiles, i.e. the function f, and we would like to deduce what is the corresponding turbulent viscosity we need to put in in order to satisfy the equations with that f. It becomes an inverse problem for turbulent viscosity.

For Equation 4.49, it is interesting to define the function $\mathcal{W}(\xi)$ such that $\mathcal{N} \equiv cf\mathcal{W}/\mathcal{W}'$, so that Equation 4.49 integrates into

$$h = \kappa \mathcal{W}^{-\mathcal{S}\lambda/c}, \tag{4.50}$$

where c and κ are positive constants to be adjusted later.

Plugging this expression into (4.43), we obtain

$$\frac{\lambda}{c}\mathcal{F} + \kappa \mathcal{W}^{-\mathcal{S}\lambda/c} + \left(\mathcal{F}\frac{\mathcal{W}}{\mathcal{W}'}\right)' = 0, \tag{4.51}$$

where we have defined $\mathcal{F} = cff''$. This differential equation has an analytical solution when $\lambda/c = 1$ and $\mathcal{S}\lambda/c = 1$, i.e. $\mathcal{S} = 1$. In this particular case, we can see that:

$$\mathcal{W}(\xi) = \frac{1}{\int_0^\xi \frac{\mathcal{F}(\zeta)}{\kappa\zeta + C_1}\, d\zeta + C_2}, \tag{4.52}$$

where C_1 and C_2 are constants, satisfies Equation 4.51.

$\mathcal{N}$ must be an even function of ξ, and because f is an odd function, this imposes $C_1 = 0$. It then gives the density profile h,

$$h(\xi) = \lambda \int_0^\xi \frac{1}{\zeta} f(\zeta) f''(\zeta)\, \mathrm{d}\zeta + \kappa C_2 \tag{4.53}$$

Considering the boundary condition $h(\pm\infty) = 0$, we must have $\kappa C_2 = -\lambda \int_0^\infty \frac{1}{\zeta} f(\zeta) f''(\zeta)\, \mathrm{d}\zeta$.

The expression of eddy viscosity $\mathcal{N} \equiv cf\mathcal{W}/\mathcal{W}'$ becomes:

$$\mathcal{N}(\xi) = -\frac{\xi}{f''(\xi)} \left(\lambda \int_0^\xi \frac{1}{\zeta} f(\zeta) f''(\zeta)\, d\zeta + \kappa C_2\right). \tag{4.54}$$

Based on measurements, the time-averaged cross-stream profiles of velocity and buoyancy are found to have a self-similar Gaussian shape (Rouse, Yih, and Humphreys, 1952, Kotsovinos, 1975, Ramaprian and Chandrasekhara, 1989, Paillat and Kaminski, 2014a, Parker et al., 2020, Richardson and Gary R. Hunt, 2022). Then we illustrate the above analytical solution in the Gaussian case, for which $f(\xi) = a\,\mathrm{erf}(b\xi)$, where a and b are positive constants to be adjusted later. With this

choice for f we have

$$f(\xi)f''(\xi) = -\frac{4}{\sqrt{\pi}}\, a^2 b^3 e^{-b^2\xi^2}\, \xi\, \mathrm{erf}(b\xi). \tag{4.55}$$

Plugging into (4.53), we obtain the density profile as

$$h(\xi) = \lambda a^2 b^2 \left[1 - \mathrm{erf}^2(b\xi)\right] \tag{4.56}$$

where we have computed the constant $\kappa C_2 = \lambda a^2 b^2$ to ensure that h vanishes at infinity. This profile is very close to the Gaussian, though a bit narrower (As shown in Figure 4.2(a)). In our experiment, Figure 5.22 shows that the buoyancy profile h is a bit wider than the velocity profile. A similar tendency is also observed by Ramaprian and Chandrasekhara, 1989, and Richardson and Gary R. Hunt, 2022. Profiles for other (typically smaller) values of $\mathcal{S}$ are clearly needed here to see its effect on the profiles.

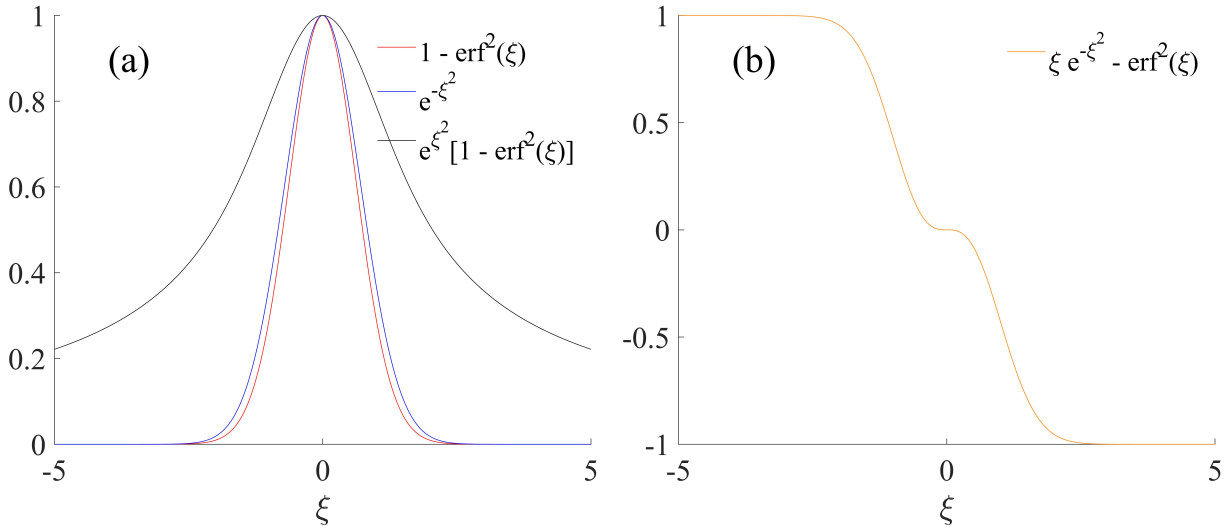

Figure 4.2: The plume profile functions. (a) Vertical velocity profile function $f^* = e^{-\xi^2}$ (blue), buoyancy profile function $h^* = 1 - \mathrm{erf}^2(\xi)$ (red), corresponding eddy viscosity profile function $\mathcal{N}^* = e^{b^2\xi^2}\left[1 - \mathrm{erf}^2(b\xi)\right]$ (black); (b) Horizontal velocity profile function $\left[\xi \exp\left(-\xi^2\right) - \mathrm{ref}\,(\xi)\right]$.

Finally, the eddy viscosity profile is

$$\mathcal{N}(\xi) = \lambda\sqrt{\pi}\,\frac{a}{b}\,e^{b^2\xi^2}\left[1-\mathrm{erf}^2(b\xi)\right]. \tag{4.57}$$

As shown by the black line in Figure 4.2(a), The profile $\mathcal{N}$ is fairly flat at the center, and decreases slowly at infinity: $e^{b^2\xi^2}\left[1-\mathrm{erf}^2(b\xi)\right] \sim \frac{2}{\sqrt{\pi}b|\xi|}$ when $|\xi| \gg 1$.

To set everything, we lastly need to fix the constants a and b (gathered with C_2, κ has scaled out of the solution). we have first the normalization condition, which writes

$$\int_{-\infty}^{\infty} h(\xi)f'(\xi)d\xi = \frac{4\lambda}{3}a^3b^2 = 1. \tag{4.58}$$

Another relation can be obtained from the definition of half-width for the Gaussian profile. We have:

$$a = \left(\frac{3}{4\lambda}\right)^{1/3}, \tag{4.59}$$

$$b = 1. \tag{4.60}$$

The profiles of vertical velocity and buoyancy can be written as:

$$h(\xi) = \left(\frac{3}{4}\right)^{2/3}\lambda^{2/3}\left[1-\mathrm{erf}^2(\xi)\right] \tag{4.61}$$

$$f'(\xi) = \left(\frac{3}{4}\right)^{1/3}\lambda^{-1/3}\exp\left(-\xi^2\right) \tag{4.62}$$

For Equation 4.35, 4.36, and 4.57, we have:

$$u_x(\xi) = B^{1/3}\left(\frac{3}{4}\right)^{1/3}\lambda^{2/3}\left[\frac{2}{\sqrt{\pi}}\xi\exp\left(-\xi^2\right)-\operatorname{erf}(\xi)\right] \tag{4.63}$$

$$u_z(\xi) = B^{1/3}\left(\frac{3}{4}\right)^{1/3}\lambda^{-1/3}\frac{2}{\sqrt{\pi}}\exp\left(-\xi^2\right) \tag{4.64}$$

$$\tilde{g} = B^{2/3}\left(\frac{3}{4}\right)^{2/3}\lambda^{-2/3}\frac{1}{z}\left[1-\operatorname{erf}^2(\xi)\right] \tag{4.65}$$

$$\mathcal{N}(\xi) = \sqrt{\pi}\left(\frac{3}{4}\right)^{1/3}\lambda^{2/3}\exp\left(\xi^2\right)\left[1-\operatorname{erf}^2(\xi)\right] \tag{4.66}$$

The profile shape for u_x is shown in Figure 4.2(b). To simplify, all the pre-factors are set as one. The horizontal velocity profile is almost flat in the middle and becomes constant away from the plume, which converges to the entrainment velocity u_e.

4.4 Conclusion

The MTT model is adapted for 2D particle plumes. We obtain a simple power-law solution based on the top hat profile. The plume half width b is proportional to height, and the plume middle line vertical velocity u_p is independent to z and proportional to $B^{1/3}$. Considering the closure $u_e = \alpha u_p$, it means the entrainment velocity is constant along the z direction.

The MTT model works very well with a simple entrainment assumption. We restart with the Reynolds-average Navier-Stokes equation with a mixing length approach. We solve the profiles when the turbulent Schmidt number is equal to 1. With the assumption of the Gaussian velocity profile (Equation. 4.63), we obtain the buoyancy profile and eddy viscosity profile. The buoyancy profile (Equation. 4.65) is not Gaussian but similar, and slightly narrower than the velocity profile. For the horizontal velocity u_x, we find that u_x is almost equal to zero in the plume. This derivation is still in the preliminary stage. It provides a framework that can calculate the plume profiles without entrainment assumption by B R Morton et al., 1956.

5 Experimental results

In this chapter, we first introduce the parameters characterizing four types of plumes in Section 5.1. Then in Section. 5.2, we focus on the plastic bead plumes to discuss about the data processing. It is based on two types of measurements: concentration of particles within the plume and velocity field by PIV. The reliability of the experimental set-up is shown in Section. 5.3. Two kinds of injection methods are compared to test whether the result is independent of the injection. The result of the plastic bead plume is compared to the result of the homogeneous dissolved NaCl plume to verify the role of particles in the plume. The comparison between the plumes with dissolving or non-dissolving particles is discussed in Section 5.4. Section. 5.5 is for the conclusion.

5.1 Experimental parameters

Three types of particles are used in the experiment, i.e. plastic bead, butyramide, and KNO_3. A homogeneous dissolved NaCl solution is also used for comparison. Butyramide and KNO_3 particles (140 µm to 200 µm) are premixed with their corresponding saturated solution and injected into the tank contained quiescent water. Correspondingly, the plastic beads are premixed with water. After injection, the particles get dispersed and form plumes.

In the experiments, the major variable parameter is the total injection rate, which includes the liquid and the suspended particles in it. The ranges of injection rates for different plumes are shown in Figure 5.1. The range is from $0.1\,\mathrm{g\,s^{-1}}$ to $2.5\,\mathrm{g\,s^{-1}}$. From $0.1\,\mathrm{g\,s^{-1}}$ to $1.0\,\mathrm{g\,s^{-1}}$, the

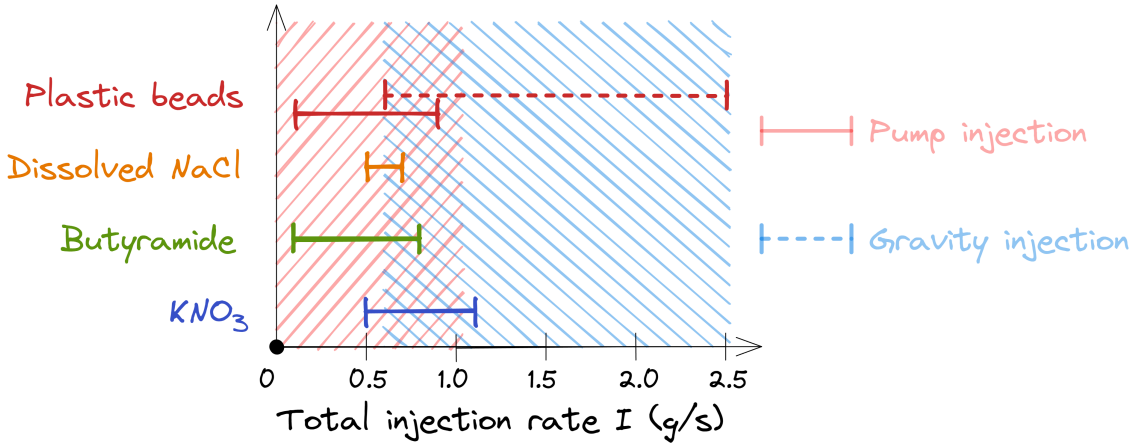

Figure 5.1: Total injection rate I range for different particles. I includes both the suspended particles and the liquid.

solution is injected with a peristaltic pump, shown in pink shadow in Figure 5.1. From $0.7\,\mathrm{g\,s^{-1}}$ to $2.5\,\mathrm{g\,s^{-1}}$, gravity injection is used, as shown in blue in Figure 5.1. For KNO_3, the maximum injection rate with pump is higher than $1.0\,\mathrm{g\,s^{-1}}$. This is due to the fact that the density of KNO_3 solution is higher than the others. The saturated KNO_3 solution is $(1.18 \pm 0.01)\,\mathrm{g\,cm^{-3}}$, which leads to a maximum injection rate for KNO_3 of $1.1\,\mathrm{g\,s^{-1}}$.

In Figure 5.1, for all four plumes, there is a common range between $0.5\,\mathrm{g\,s^{-1}}$ to $0.7\,\mathrm{g\,s^{-1}}$, where the behaviors of the different plumes can be compared. For plastic beads plume, there is an overlap between pump injection and gravity injection, which allows us to test the independence of the results with respect to different injection methods. By comparing the dissolved NaCl plumes and plastic bead plumes, we verified the similarity of buoyancy plumes with or without particles in them. By comparing the plastic bead plume and butyramide plume, we could figure out the role of particle dissolving during the plume development. Comparing KNO_3 plume and butyramide plume shows the influence of density difference between the particle and the ambient fluid. KNO_3 makes heavier the density of ambient fluid after dissolving, but butyramide has almost no influence.

Figure 5.2 shows the development of a plastic bead plume ($I = 0.39\,\mathrm{g\,s^{-1}}$) from the beginning

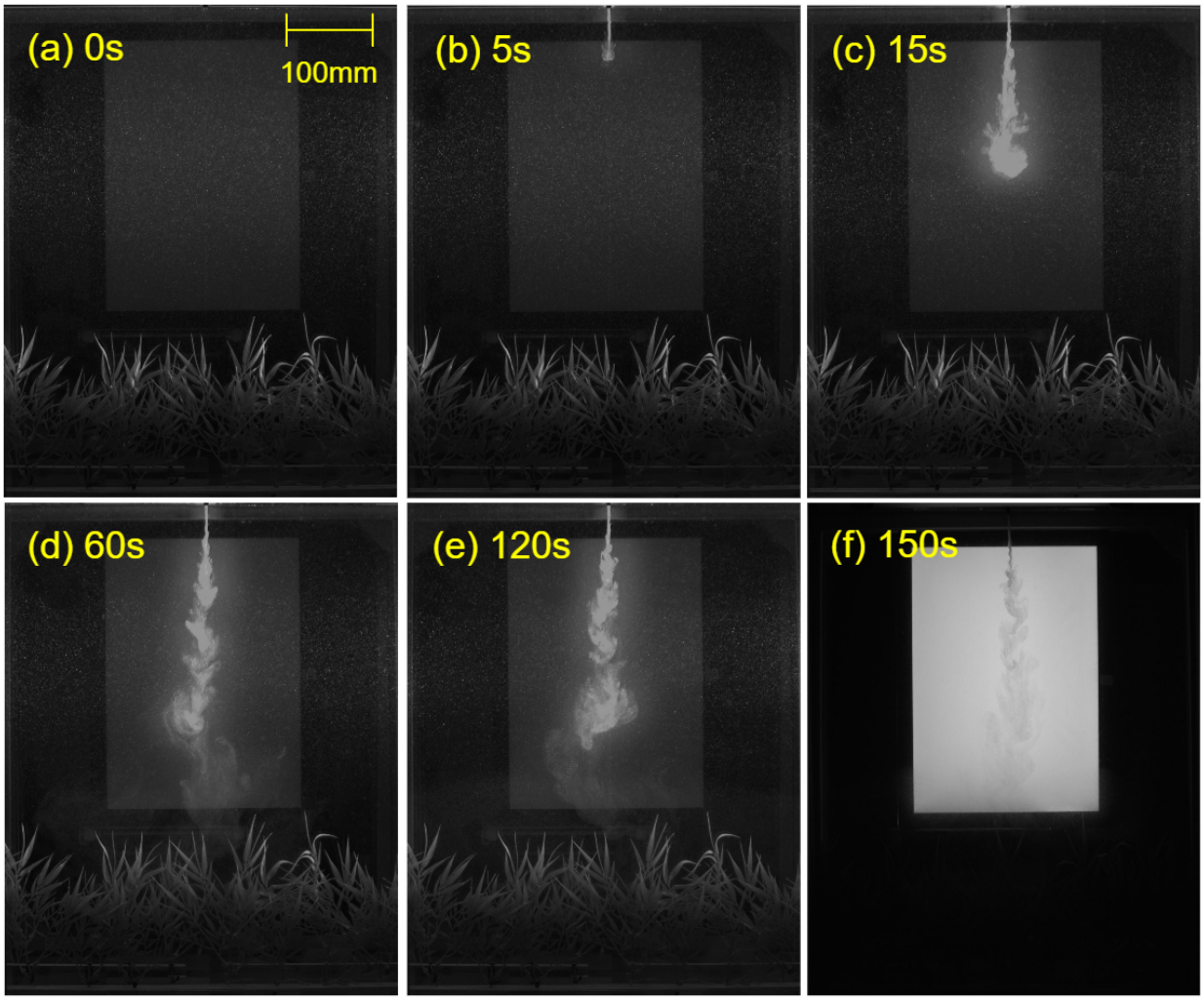

Figure 5.2: Sequence of images of the establishment of a plume generated by the injection of a plastic bead solution. Total injection rate $I = 0.39\,\mathrm{g\,s^{-1}}$. (a-e) Raw images for the plume illuminated by two lasers; (f) The raw image for the plume illuminated by the backlight. After 60 s, the plume is considered fully developed. The discussion about the velocity field in this chapter is mainly focusing between 60 s to 120 s. The plume shape measurement with back-light is performed between 150 s to 180 s.

of the injection. In the beginning, the plume is illuminated with one laser on each side. For Figure 5.2(a), $t = 0$ s is the moment when the front of the plume just gets into the tank. This moment is about 2 s later than when the injection starts (switch on the valve). Because there is no particle at the entrance, the front part that gets into the tank is only liquid. In Figure 5.2(b), there are some particles entering the tank vertically. It looks like a straight line at first, but the front becomes unstable due to Rayleigh–Taylor instability (Sharp, 1984). In Figure 5.2(c), the particles expand during falling and form the plume. Between 60 second and 120 second, shown in Figure 5.2(d-e), the plume is fully developed and statistically steady (As shown in Figure 5.12). The discussion about the velocity field is mainly focusing on this period. After 120 second, the lasers are switched off temporarily and the back-light is turned on. Following the processes shown in Figure 3.5, we record during another 30 s to measure the plume shape with back-light. After about 150 second, the valve is switched off to stop the injection.

Figure 5.3 shows the average shapes for different plumes with similar total injection rates. The backgrounds are removed, and the contrasts of the images are enhanced for better visualization. The average period is 30 s, 300 frames, when the plume is fully developed. Figure 5.3(a, c, d) are illuminated with back-light. For Figure 5.3(b), the plume is lighted with a violet laser. Since there is no particle in the dissolved NaCl plume, it is invisible under the backlight. 1.25 mg L^{-1} fluorescein is mixed in the plume solution for coloring, which emits green light under a violet laser.

With a similar injection rate, the plume shape looks similar to the plastic bead plume (Figure 5.3(a)) and dissolved NaCl plume (Figure 5.3(b)). The solution falls into the tank and expands due to mixing, and shows a symmetrical triangular shape in the image. Close to the bottom, the plume slows down due to the artificial grass at the bottom. On the other hand, when the plume contains soluble particles, butyramide plume (Figure 5.3(c)) and KNO_3 plume (Figure 5.3(d)), the average shapes look more vertical compared to the non-soluble plume.

The volume concentration of KNO_3 is lower than the other particles because the mass con-

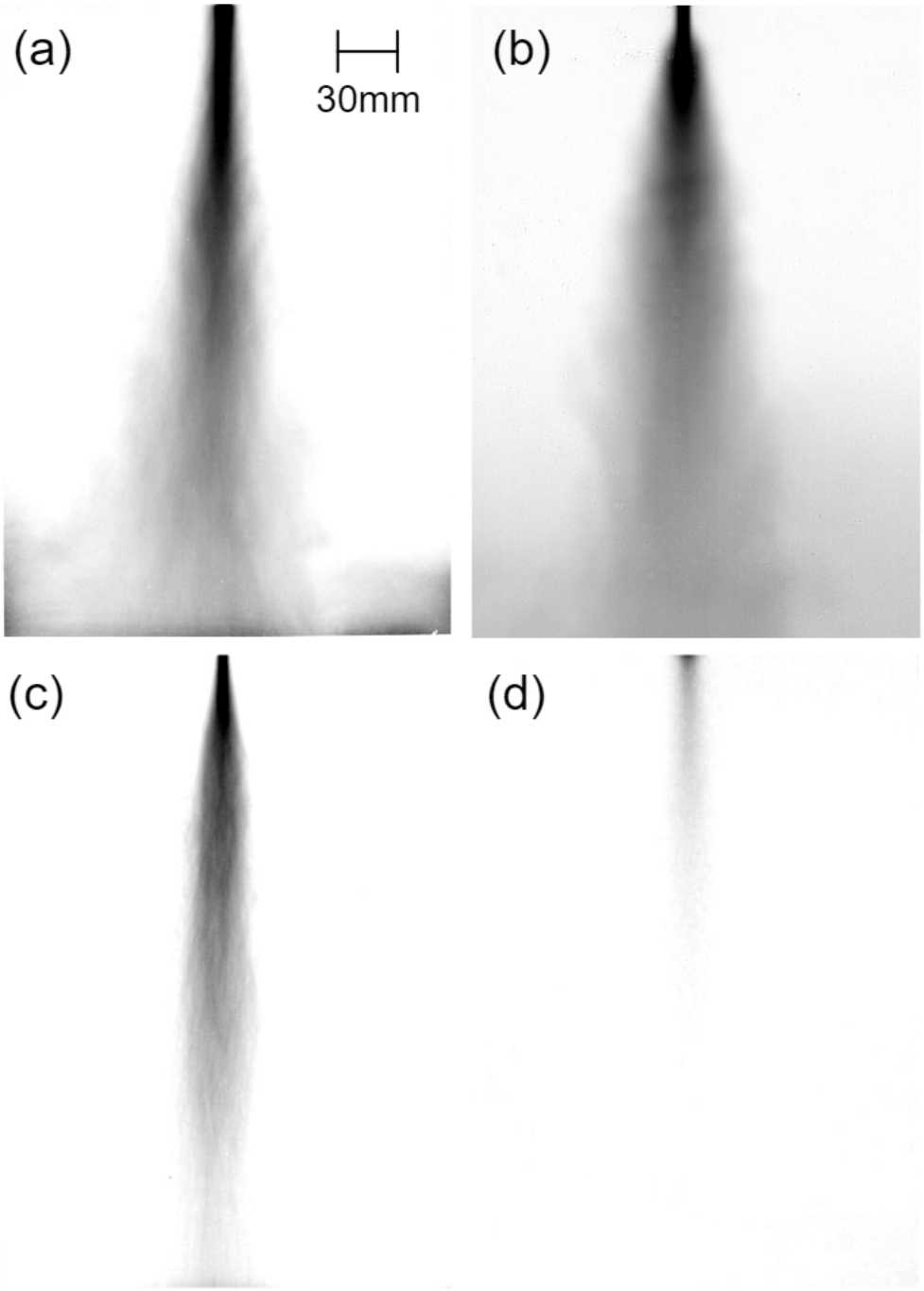

Figure 5.3: Average image for four different plumes with similar injection rate I. The contrasts of images are enhanced and the images are reversed for better visualization. (a) Experiment for plastic bead plume, gravity injection, the total injection rate $I = 0.59\,\mathrm{g/s}$, illuminated with back-light; (b) Experiment for dissolved NaCl plume, pump injection, $I = 0.56\,\mathrm{g/s}$. The image corresponds to the use of the green channel only due to the fact that the fluorescein is used for coloring; (c) Experiment for butyramide, pump injection, $I = 0.53\,\mathrm{g/s}$, illuminated with back-light; (d) Experiment for KNO_3, pump injection, $I = 0.56\,\mathrm{g/s}$, illuminated with back-light.

centration is the same but KNO_3 is much denser. So the average plume image for KNO_3 is much weaker. Since the densities of the plastic bead and butyramide are close to the one of water, and the density of saturated butyramide solution is also close to the one of water, the mass concentration and volume concentration are almost equivalent to 10%. But the density of KNO_3 is $2.10\,\mathrm{g\,cm^{-3}}$, which is much larger than its saturated solution ($1.18\,\mathrm{g\,cm^{-3}}$). The mass fraction of KNO_3 in its solution is calculated as:

$$\frac{m_K}{m_K + m_{KS}} = \frac{\rho_K V_K}{\rho_K V_K + \rho_{KS} V_{KS}} = 10\% \tag{5.1}$$

where the subscript K represents KNO_3, the subscript KS represents the saturated KNO_3 solution. Based on Equation. 5.1, the volume fraction for KNO_3 solution is about 6.6 %.

5.2 Measurement results for plastic bead plumes

In this section, we discuss general data processing, including the plume shape and velocity field. The analysis and discussion are focused on plastic bead plumes.

5.2.1 Average image

The plume shape is measured with a backlight. A constant LED light box is placed on the backside of the tank. During injection, the particles in the solution shade the backlight, which decreases the local intensity on the image. In order to catch this decrease, two average images are obtained. One is obtained before the injection. The image is averaged for 30 s recording of quiescent water and back-light, like Figure 5.4(a). The other one is averaged for 30 s during the injection, when the plume is fully developed, like Figure 5.4(b). The typical time scale for the turbulent structures in a plume is about 3 s, which is 10 times smaller than the averaging period. The relationship between the particle concentration and image intensity is measured for

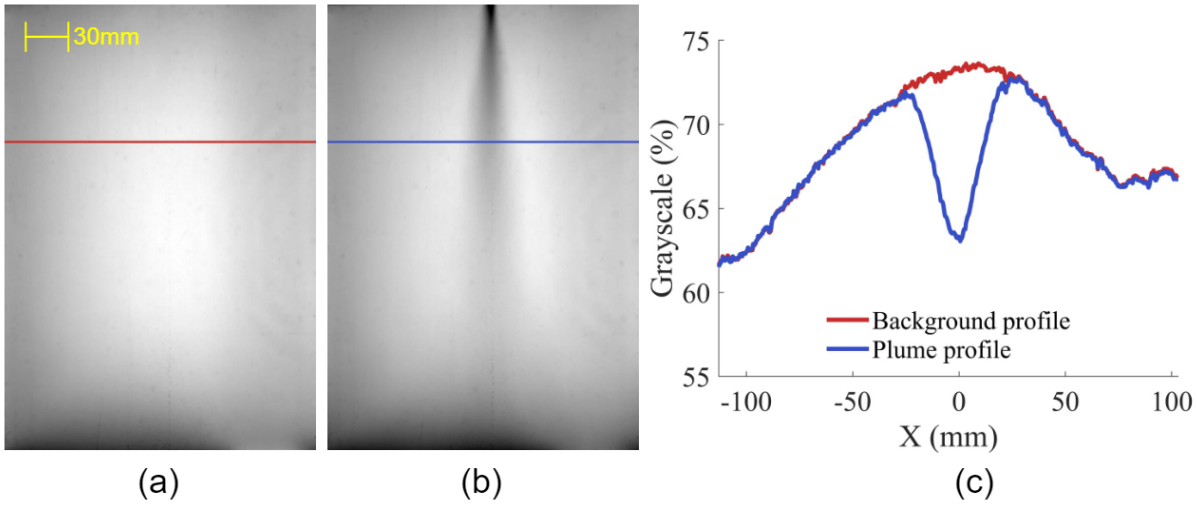

Figure 5.4: Principle of the background removal. (a) Average background image with quiescent water illuminated with backlight. The contrast of the image is enhanced for better visualization; (b) Average image when the plume is fully developed; Experiment with plastic bead, pump injection, the total injection rate $I = 0.77\,\mathrm{g/s}$. (c) The intensity profile on the indicated lines in (a) and (b).

calibration. With a suitable experiment setup, the average particle local concentration is obtained from the plume average image. The details about the concentration measurement are discussed in Section. 5.2.3.

The background image is a baseline for the measurement. The plume shape is obtained by intensity decreasing from the baseline. In Figure 5.4(c) is displayed the intensity profile at the same height in Figure 5.4(a) and (b), the color of the profiles have the same color as the indicated lines. The vertical axis is gray-scale, which is normalized with the maximum value for an 8-bit integer, 255. For these two profiles, most of the curve on the side overlaps each other. Only the part of the plume decreases the grayscale by 10% in maximum, which shows the plume shape numerically.

5.2.2 Horizontal profile

After removing the background image, the average plume image is fitted with Gaussian function on each horizontal line. The intensity difference between the background image and the

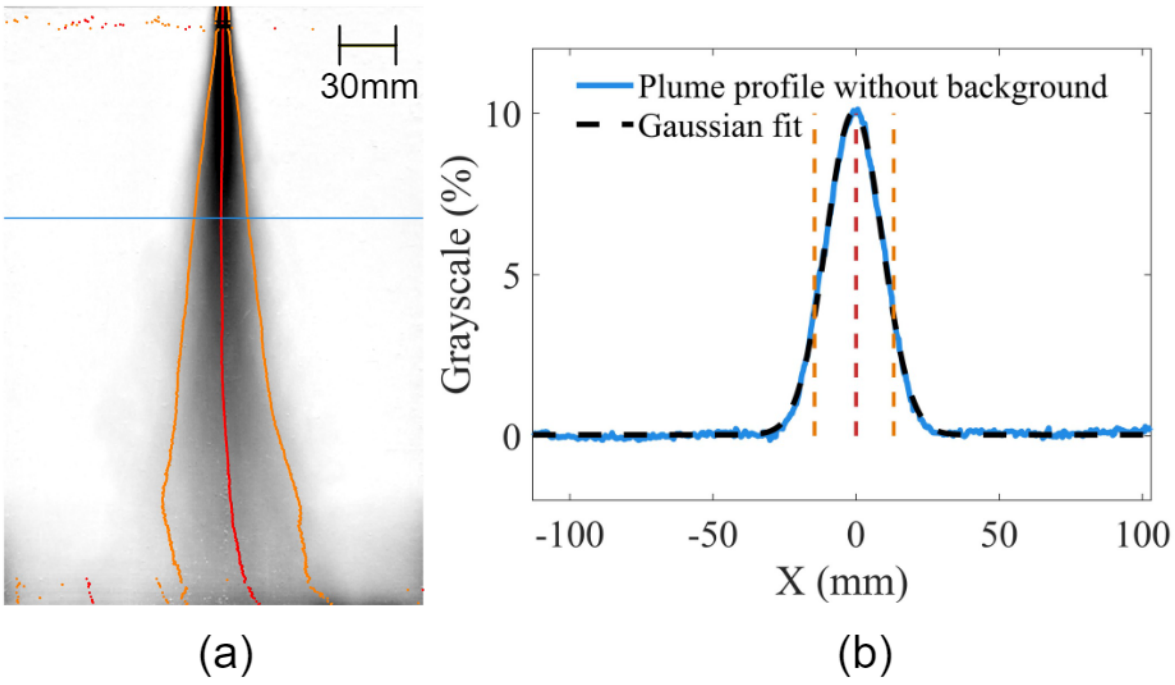

Figure 5.5: Fit of the plume intensity. Experiment with plastic beads, pump injection, the total injection rate $I = 0.77\,\mathrm{g/s}$. (a) Average image illuminated with back-light when the plume is fully developed. The red line corresponds to the maximal intensity on the horizontal line, i.e. it it the middle line of the plume profile. The orange line is the plume half-width by fit, shown in (b). The contrast of the image is enhanced and the image is reversed for better visualization; (b) The intensity profile for the blue line is indicated in (a) with Gaussian fit.

average plume image is linear to the local average concentration of the plume (Figure. 5.10). By fitting the concentration profile with Gaussian, we could have the plume shape parameters, width, and amplitude.

A typical fit curve is shown in Figure 5.5(b). The plume profile (blue) matches well with the Gaussian fit (black). Based on the fit, the plume middle is defined as the point with maximum intensity at each height. And the plume half width is defined as the point where the intensity is 1/e of the maximum intensity. By connecting the middle points and half-width points on each height, the plume middle line and half-width line are plotted in Figure 5.5(a) with red and orange curves. These two lines are continuous in the middle part of the image, which shows that the fit works well for catching the plume shape.

In Figure 5.5(a), there are some breakpoints at the top and bottom of the image, because the profiles there are not Gaussian anymore. Close to the entrance, the plume is not fully developed. Close to the bottom, the plume shape is influenced by artificial grass. In Figure 5.6, the intensity profiles are normalized with their maximum intensity and plume half-width. For the middle part, the normalized curves overlap each other. It proves that the profiles are all Gaussian, and the plume shape is self-similar. For the violet line, as it is very close to the bottom, the profile shape is changed due to the particles accumulated above the artificial grass.

The plume shape characteristics are shown in Figure 5.7. For these four figures, the vertical axis shows the distance to the entrance. The point $Z = 0$ is not shown due to a gap of about 4 cm between the entrance and the top of the backlight. The plume middle line from the fit is almost vertical until $Z = 250$ mm in Figure 5.7(a). The plume half-width is shown in Figure 5.7(b). The half-width is linear with height, consistent with theoretical predictions for one-phase non-dissolving plume in Section. 4.2.

In Figure 5.7(c), we see the decrease of the plume middle line intensity along the vertical direction. According to the theory (Section. 4.2), the plume middle line concentration, and thus the middle line intensity in the experiments, is inversely proportional to height. Figure 5.7(d) shows the integration of the plume intensity over the X direction. The unit of integration of intensity is gray-scale times pixel. Between 130 to 280 mm, the integration of intensity is almost constant with respect to Z. The plume intensity is linear with the particle local concentration (Figure 5.10), and the integration of plume intensity refers to the mass flux along the Z direction. For plastic bead plume, the mass flux is constant over Z.

Figure 5.8 shows the slope of the plume half-width line as a function of the injection rate for plastic beads plume. As predicted by the theory, the half-width of the non-dissolved plume increases linearly along the height direction. From its slope, we measure the entrainment coefficient α, which is forward independent to the injection rate (Figure 5.8).

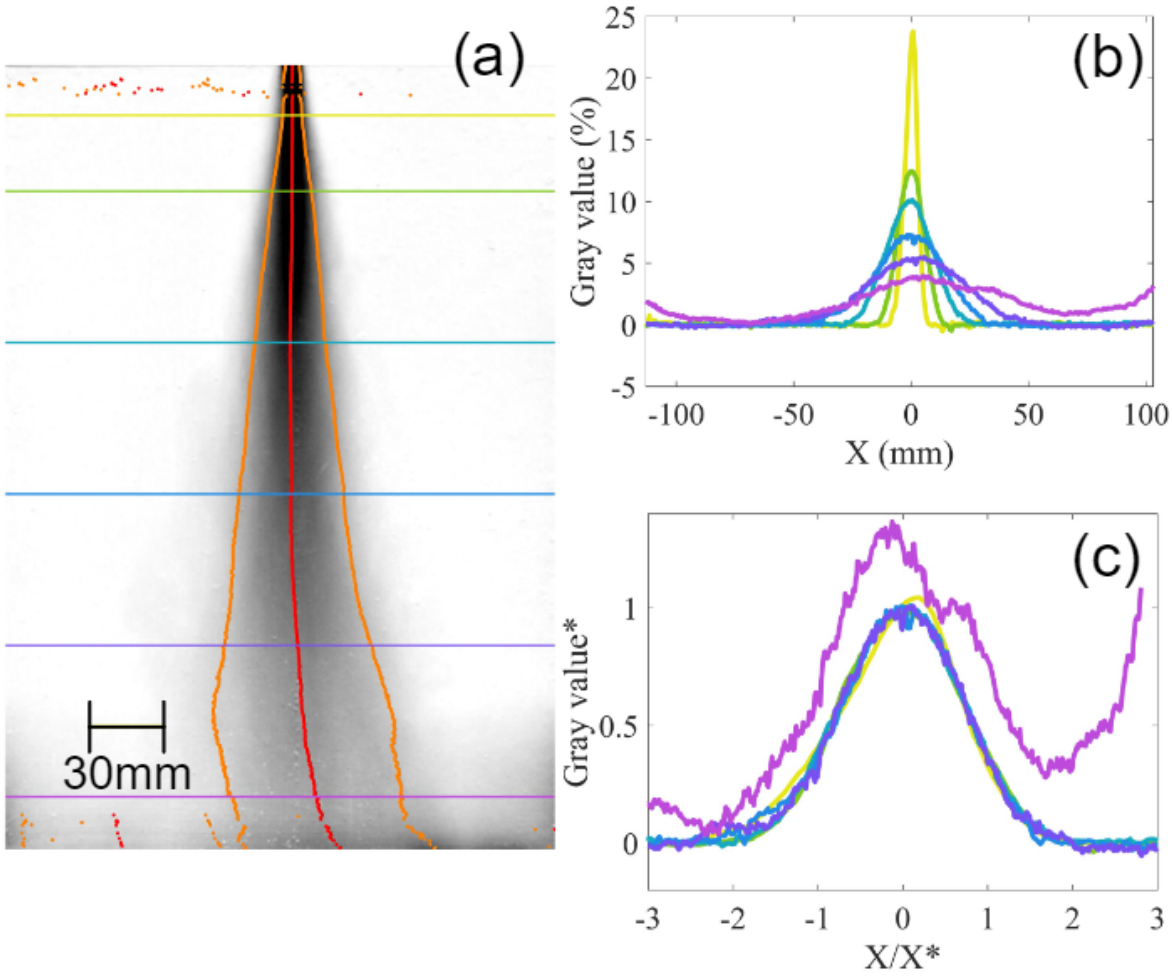

Figure 5.6: Intensity profiles at different heights. Experiment for plastic beads, pump injection, the total injection rate $I = 0.77\,\mathrm{g/s}$. (a) Average image illuminated with back-light when the plume is fully developed. Red and orange lines are the plume middle lines and the plume half-width line shown in Figure 5.5; (b) The intensity profiles in different heights; (c) The normalized intensity profiles in different heights. X^* is the plume half width, as shown in Figure 5.5(b) in orange dashed line.

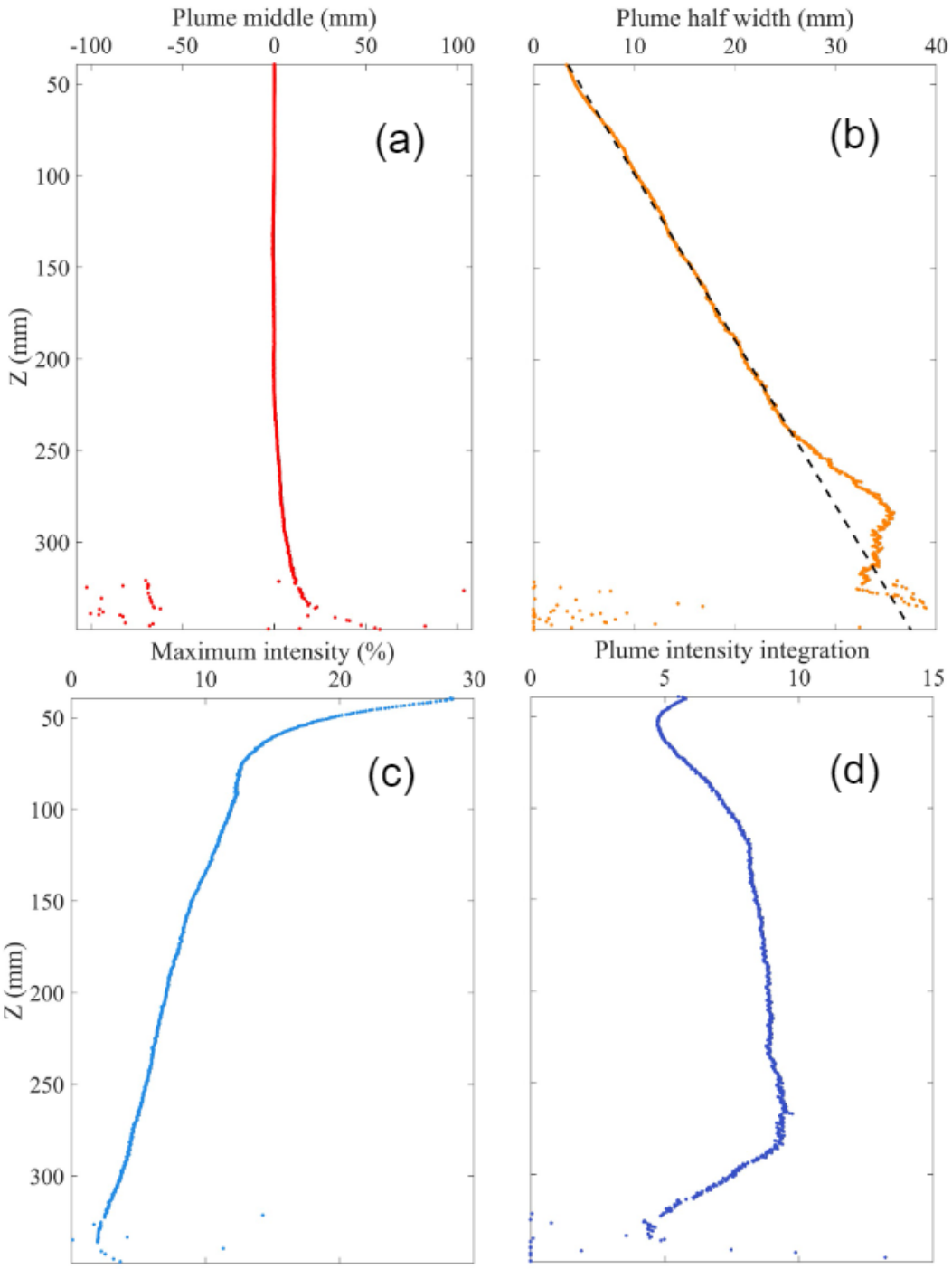

Figure 5.7: The characteristics of the plume shape obtained by fit (see in Figure 5.5). Plastic bead, pump injection, the total injection rate $I = 0.77\,\mathrm{g/s}$. (a) Plume middle line; (b) Plume half-width, the black dashed line for linear fit; (c) Plume middle line intensity; (d) The integration of plume intensity.

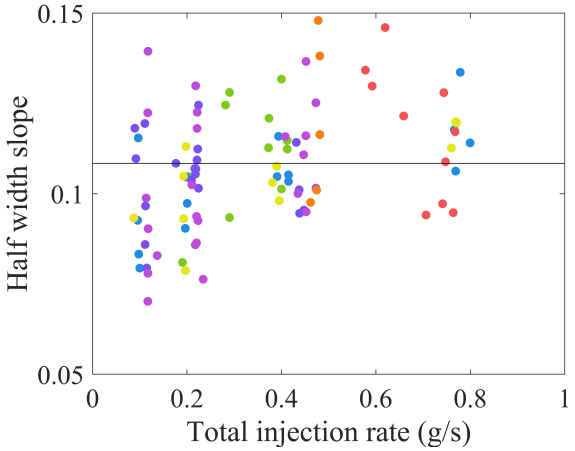

Figure 5.8: The half-width line slope as a function of total injection rate I, for plastic beads plume. The different colors represent experiments in different days. The black line is the average slope for all the cases, where $\alpha = 0.108 \pm 0.017$

5.2.3 Mass flux

The plume shape is obtained as the difference between the plume average image and the background image. With a suitable experimental setup, by choosing the exposure time, the back-light intensity is not saturated but close, to ensure that the intensity is in the linear regime and with enough resolution. The particle local concentration is linear with the image intensity reduction.

For non-dissolving plumes, the mass flux is constant at different heights. Correspondingly, the intensity integration must also be constant at different heights. There are two ways to have mass flux. One is the integration of the fit profile as shown in Figure 5.7(d). The other one is the sum of 'raw data', the image intensity after removing the background. As shown in Figure 5.9, between about 140 mm to 280 mm, the intensity integration is almost constant for both fit and raw data. The raw data is the sum of the intensity difference between the average image and the background image at each height. For the top part, because the concentration in particles is too large, the decrease of the intensity is not linear with the particle local concentration. The intensity integration value is thus lower than in the middle part. For the bottom part, the profile deviates from Gaussian. The Gaussian fit is not suitable, which leads to a decrease in the fit result.

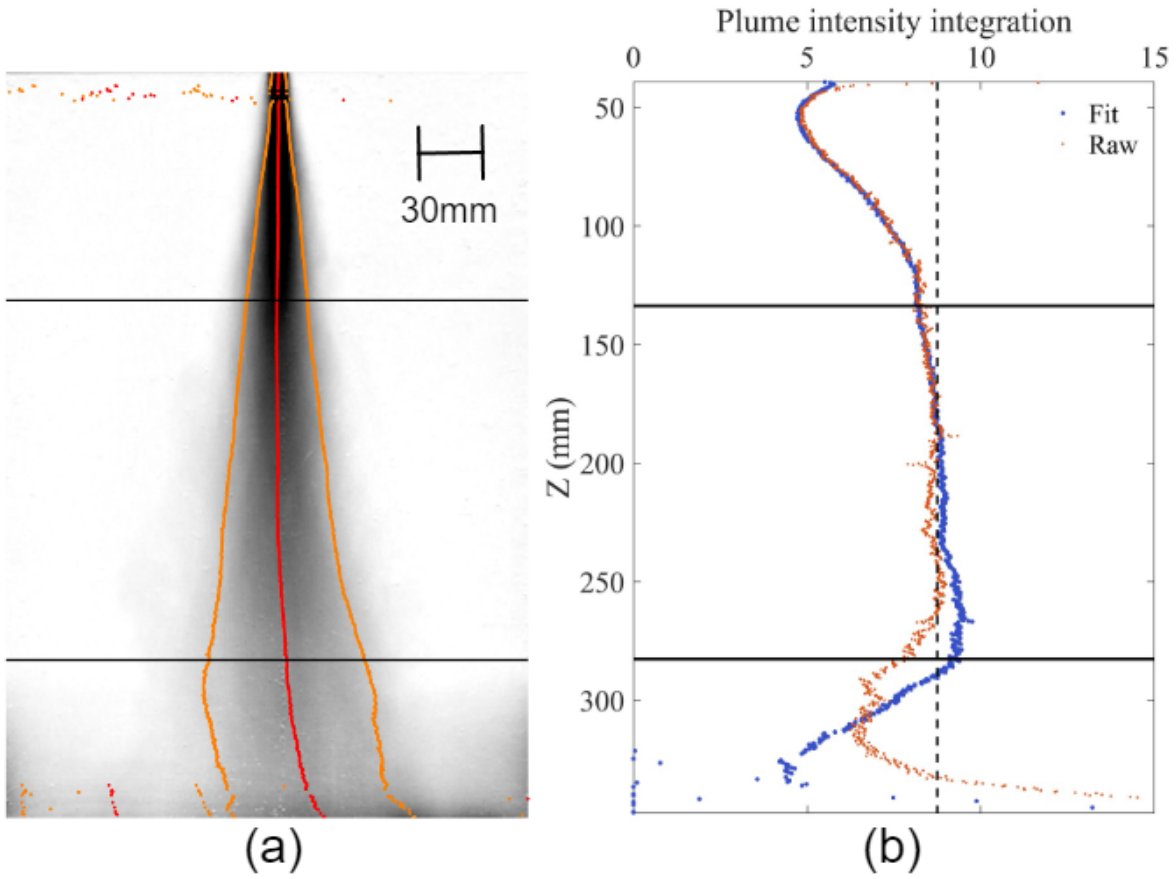

Figure 5.9: The intensity integrated horizontally (X direction) as a function of height Z. Experiment for plastic bead, pump injection, the total injection rate $I = 0.77\,\mathrm{g/s}$. The range between the black lines shows the part where the integrated intensity is almost constant. (a) Average image illuminated with back-light when the plume is fully developed. (b) Intensity integrated over X as a function of height Z. Blue line is the integration of fit result, and the orange line is the sum of raw data (the average intensity after removing the background), black dashed line is the average value in the middle part.

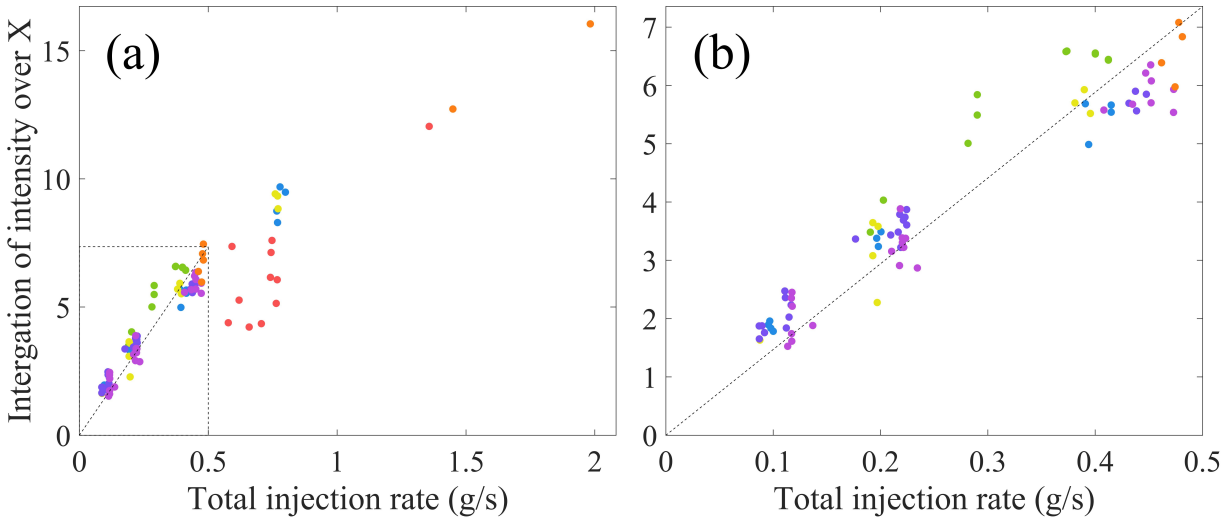

Figure 5.10: The average integration of intensity over X direction in steady state change with injection rate. Different colors for different days of the experiment. (a) Full scale; (b) A localized zoom-in for total injection rate $I < 0.50\,\mathrm{g\,s^{-1}}$

For the sum of raw data, due to the bottom effect, some particles remain at the bottom, which increases the value.

The constant region between 140 mm to 280 mm is the part where the integration of intensity measurement is in the linear region. The intensity integration between this part can be calibrated with plastic bead plume experiments with different injection rates. Figure 5.10 shows the average intensity integration as a function of the total injection rate I. Figure 5.10 shows the injection rate range from 0 to $2.0\,\mathrm{g\,s^{-1}}$, where the different colors represent different days of experiments. For injection rate, $I > 1.0\,\mathrm{g\,s^{-1}}$, the solution can only be injected with the gravity method. For injection rate $I < 0.6\,\mathrm{g\,s^{-1}}$, there are only cases injected by the pump.

In Figure 5.10(a), overall, the integration of intensity increases when the injection rate is larger, as expected. But a linear relationship is more clear when the injection rate $I < 0.5\,\mathrm{g\,s^{-1}}$. A zoom-in view is shown in Figure 5.10(b), with a linear fit for the cases whose injection $I < 0.5\,\mathrm{g\,s^{-1}}$. The linear fit is good with an R-Square equals to 0.88, and the result is repeatable for different days. Based on this fit curve, the mass flux is calibrated when the injection rate is under $0.5\,\mathrm{g\,s^{-1}}$. The red and orange points are more scattered than the other data points. These two

data set comes from gravity injection. It may due to the fact that the injection is not stable for a lower injection rate.

5.2.4 PIV measurement

The velocity field on the sides of the plume can be measured with the PIV method. Since the particles inside of the plume shade the laser, for better illumination, two lasers are placed one on each side of the plume in the same plane. Also due to the presence of the particles, it is impossible to measure the fluid velocity inside of the plume, because the concentration of the particle is too high and we cannot distinguish the PIV beads and the particles. As a consequence, the PIV measurement is limited to the velocity field on the sides of the plume, i.e. the velocity of the clear water entrained into the plume.

The typical plume vertical velocity is about $30\,\mathrm{mm\,s^{-1}}$. For the velocity on the side of the plume, the typical value is about $3\,\mathrm{mm\,s^{-1}}$, one-tenth of the plume vertical velocity. This velocity is relatively low, so the measurement frequency for PIV is set to 1 Hz only to avoid noise.

Figure 5.11 shows a series of images with velocity field in green arrows. 0 s represents the time when the plume starts to get into the tank. In the beginning, as illustrated in Figure 5.11(a), water in the tank is basically stationary. There are some slight convections (local velocity $< 1.5\,\mathrm{mm\,s^{-1}}$) due to slight temperature gradients. The maximum speed of the convection is no more than $1\,\mathrm{mm\,s^{-1}}$ when the experiment room is homogeneous in temperature and waiting for at least 5 minutes. In Figure 5.11(a-d), we see the plume falling into the tank and expanding. The tip of the plume looks like a sphere that pushes away the liquid in front of it. During falling down, the plume is diluted by the entrainment on the side.

In Figure 5.11(e), we see the front of the plume that goes through the artificial grass at the bottom. On the side of the plume, there is a region where the velocities have almost no vertical components. The plume is fully developed after about 60 s. In Figure 5.11(f), we see that there is no significant change in the velocity field far from the plume. The average velocity between 60 s

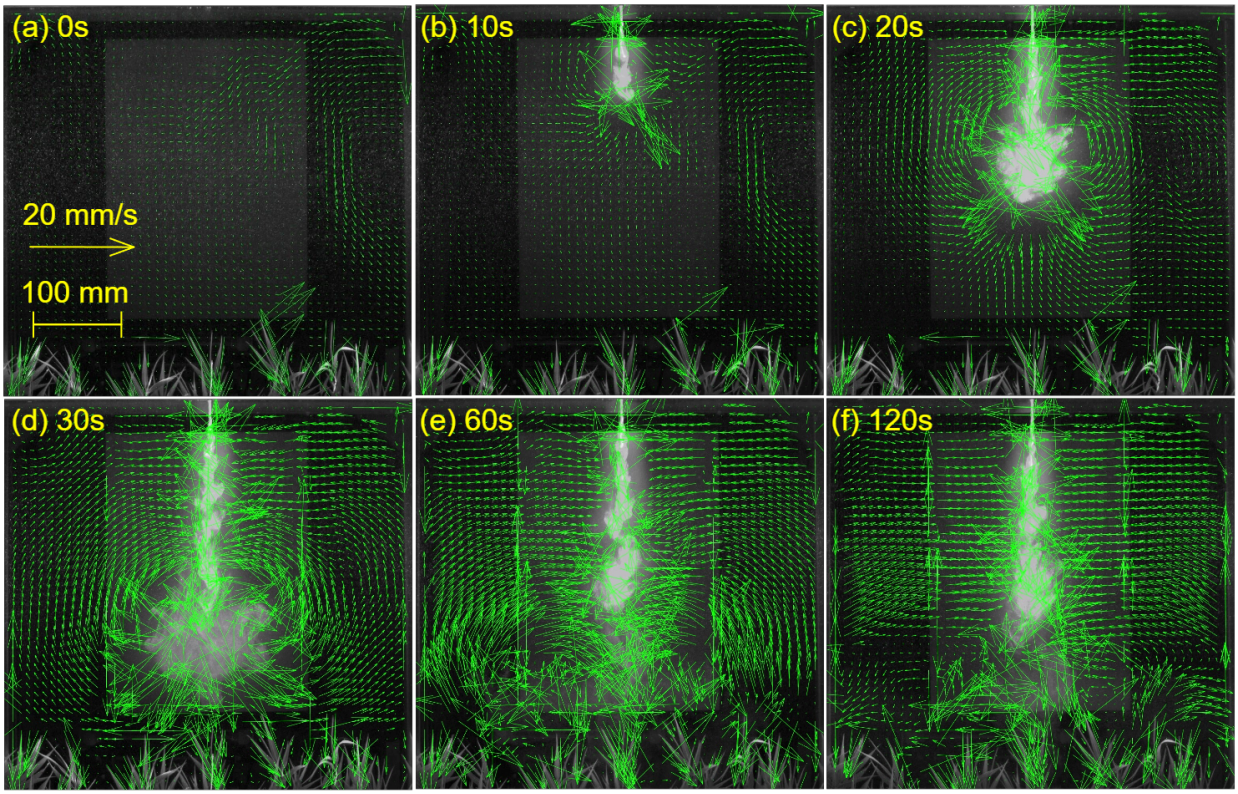

Figure 5.11: PIV velocity field series. The measurement frequency is 1 Hz. 0 s corresponds to the time when the plume starts to get into the tank. Experiment for plastic bead plume, injection rate $I = 0.45\,\mathrm{g\,s^{-1}}$.

to 120 s can be considered as the entrainment velocity of the plume. Note: there are some strange velocity vectors on the side. This is due to the position of the boundary of the backlight, as the PIV algorithm is influenced if the background is not removed perfectly.

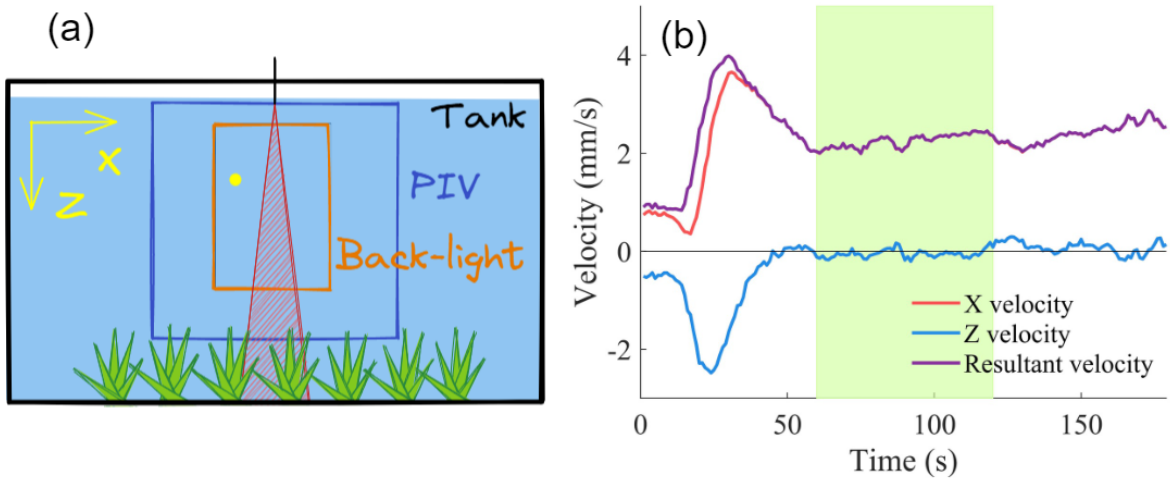

Figure 5.12: Velocity change with time at a single point located outside the plume and its location in the experiment setup. The yellow point is 150 mm below the entrance and 75 mm away from the plume middle line. Experiment with plastic beads plume, pump injection, the total injection rate $I = 0.47$ g/s. (a) The schematic of measurement, the measurement point is indicated with yellow point; (b) The velocity at the yellow point in (a) change with time. Green area is the usual measurement window between 60 s to 120 s

Figure 5.12(b) shows the velocity at the yellow point as a function of time. The experiment is for plastic beads, with $I = 0.47$ g/s. The point location is displayed in Figure 5.12(a). It is a point on the left side of the plume but close to it. The X and Z velocity are shown with the red and blue curves, and the purple curve is the resultant velocity, i.e. the norm of the vectorial sum of the velocity components. When $T = 0$ s, the velocity is not equal to $0\,\mathrm{mm\,s^{-1}}$ due to the initial convection motion in the tank. The curves jump when the front of the plume passes through the yellow point. After about 60 s, both X and Z velocities become constant, and the Z velocity goes to $0\,\mathrm{mm\,s^{-1}}$, and the purple curve overlaps with the red curve. At least until 180 s, the velocities are rather stable. The green area is the period during which we do the average to get the entrainment velocity at this point.

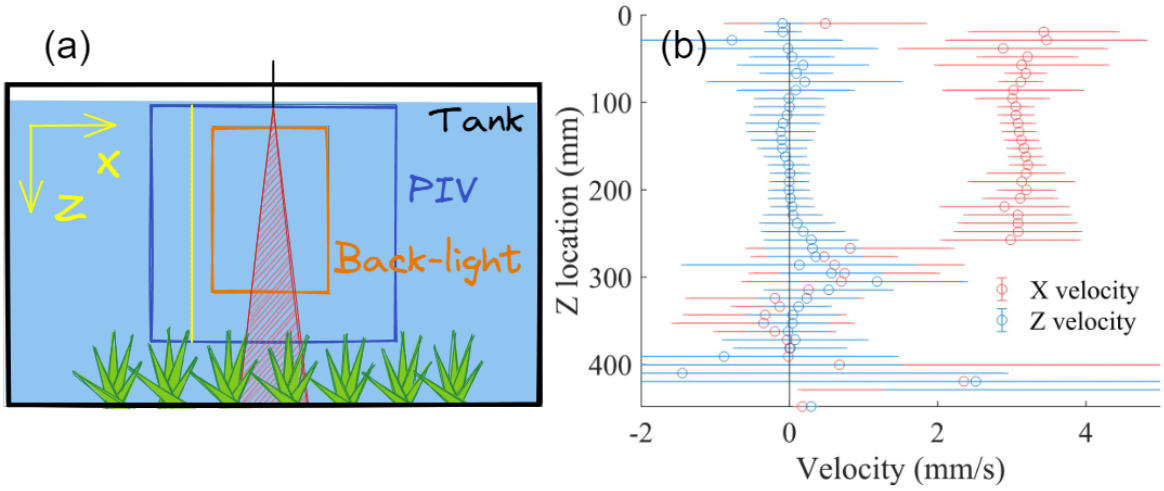

Figure 5.13: The vertical velocity profile out of the plume and the measurement location in the experimental setup. Experiment with plastic bead, pump injection, the total injection rate $I = 0.77\,\mathrm{g/s}$. (a) Schematic of measurement. The measure location is indicated with a yellow line; (b) Vertical velocity profiles along the yellow line in (a) Error bar is the standard deviation.

Based on the averaging interval shown in Figure 5.12(b), the entrainment velocity profiles are plotted in Figure 5.13. The X and Z components are plotted with red and blue points. The error bar is the standard deviation. z location is the distance to the entrance. The Z velocity is almost zero at all heights. The X velocity is almost constant between about 40 mm and 270 mm. This corresponds to the theory for 2D non-dissolving plume, the entrainment velocity being predicted as constant along the z direction (Section 4.2). For below 270 mm, the X velocity goes to zero due to the artificial grass.

Since the entrainment velocity is constant for 2D plumes, gathering the entrainment velocity on the side of the plume, like in Figure 5.13, we have the entrainment velocity for varies total injection rates I for plastic bead plumes. According to the scaling law discussed in Section 4.2, the entrainment velocity only depends on the buoyancy flux B added into the tank. For particle plumes, the buoyancy flux only comes from particles suspended in the fluid. The expression of B can therefore be expressed as:

$$B = \tilde{g}\frac{\epsilon I}{\rho_s l_w} \tag{5.2}$$

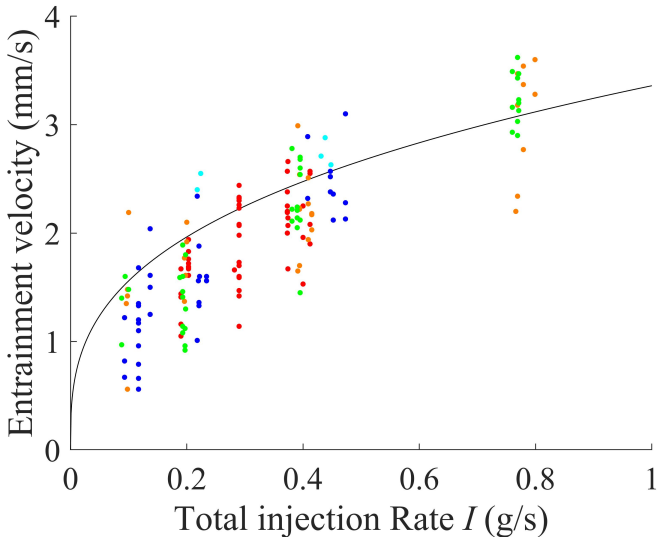

Figure 5.14: Entrainment velocity vs total injection rate, plastic beads plume. The theory is the black line (Equation. 5.3).

where ϵ is the particle mass fraction in the plume solution, which is 10% in our experiments. l_w is the width of the tank. The entrainment velocity

$$u_x = \alpha^{2/3} B^{1/3} \tag{5.3}$$

where $\alpha = 0.108 \pm 0.017$ based on our measurement.

In Figure 5.14, the black line is the theoretical prediction calculated from Equations 5.2 and 5.3, and the colored points are the average entrainment velocity for different injection rate. For the theory calculation, there is no adjustable parameter. There is a relatively large uncertainty for these entrainment velocities for all injection rates, but the tendency is consistent well with the theory prediction.

5.3 Experimental setup verification

In this section, the experimental setup is verified in two aspects. One is checking the independence of the experimental results with respect to the injection method. The measurements are compared between pump injection and gravity injection with similar injection rates. The other check is the comparison of the results for the plastic bead plume and the dissolved NaCl plume with the same equivalent density as the plastic bead solution.

5.3.1 Injection independence verification

In order to extend the injection rate range in the experiment, two different injection methods are used, pump injection and gravity injection. Due to the limitation of tube size and pump rotation speed, the maximum injection rate by the pump is about $1.0\,\mathrm{g\,s^{-1}}$. For gravity injection, the injection rate is controlled by the vertical gap between the solution water level and the entrance. For an injection rate smaller than $0.6\,\mathrm{g\,s^{-1}}$, the gap must be smaller than 10 mm, which is difficult to keep constant during the injection. Moreover, the particles in the tube block occasionally due to friction, which makes the injection rate unstable if too small.

There is an overlap between these two injection methods, $0.6\,\mathrm{g\,s^{-1}} < I < 1.0\,\mathrm{g\,s^{-1}}$, which allows us to verify the independence of the results with respect to the injection methods. In Figure 5.15, we compare the plastic bead plume shape characteristics for the two different injection methods. The pump injection and the gravity injection are indicated with orange and blue curves, respectively. For plume half width (Figure 5.15(a)), these two curves almost overlap each other from about 50 mm to 300 mm. For plume intensity integration, both curves have a plateau from about 120 mm to 250 mm. Based on Figure 5.10, the relationship between injection rate and average intensity integration becomes complicated when total injection rate $I > 0.5\,\mathrm{g\,s^{-1}}$. About 10% difference between the average intensity integration for the two injection methods is reasonable.

For the velocity field, we show in Figure 5.16, the X velocity vertical profiles for the two injec-

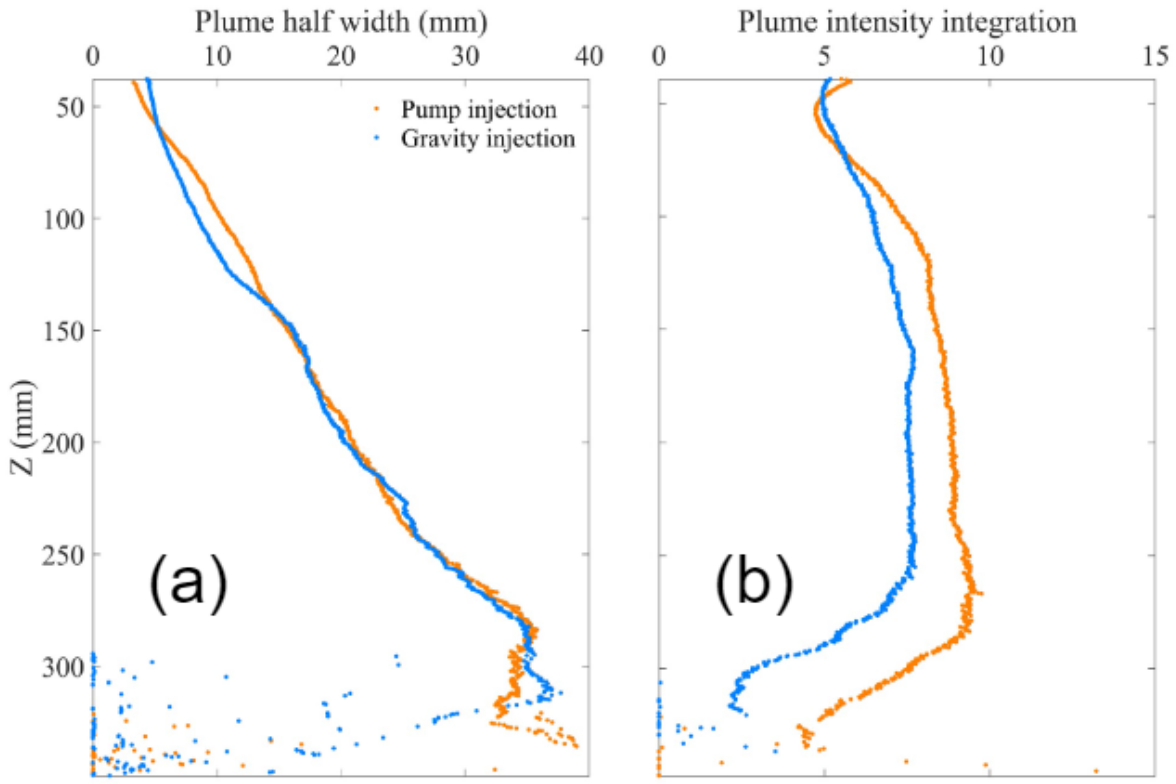

Figure 5.15: Comparison of plume shape characteristics between two injection methods. Orange for pump injection ($I = 0.77\,\mathrm{g\,s^{-1}}$) and blue for gravity injection ($I = 0.75\,\mathrm{g\,s^{-1}}$) . (a) Plume half-width comparison; (b) Plume intensity integration comparison

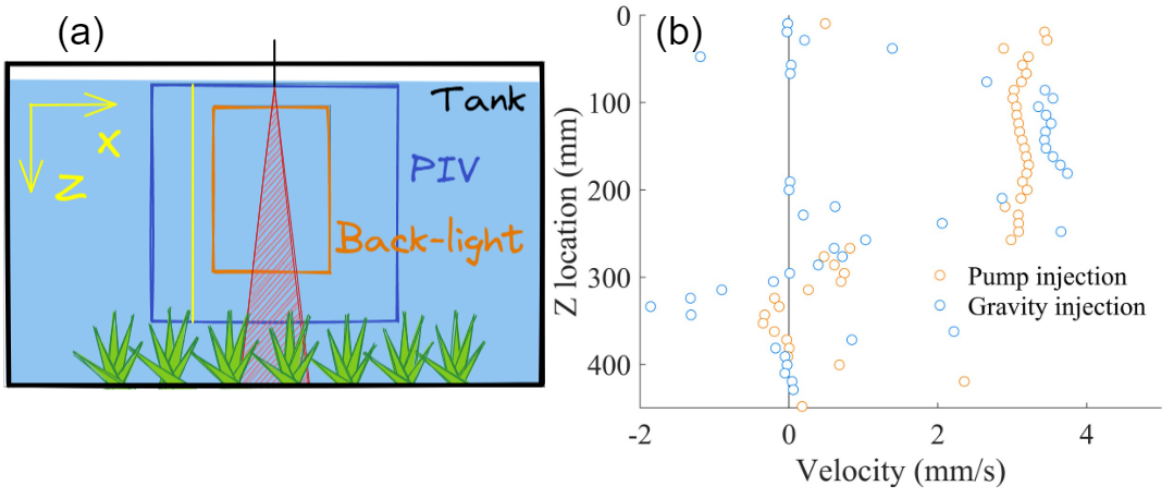

Figure 5.16: The vertical X velocity profile out of the plume and the measurement location in the experimental setup. Experiment with plastic beads. Orange for pump injection ($I = 0.77\,\mathrm{g\,s^{-1}}$) and blue for gravity injection ($I = 0.75\,\mathrm{g\,s^{-1}}$) (a) Schematic of measurement. The measure location is indicated with a yellow line; (b) X velocity vertical profiles along the yellow line in (a).

tion methods at the same place. As for the plume half-width, the two velocity profiles show the same tendency, and have a plateau between 80 mm to 250 mm. Below 250 mm, the entrainment velocity is reduced to 0 mm due to bottom effect.

5.3.2 Dissolved NaCl solution plume

We compare plastic bead plumes with dissolved NaCl solution plumes of the same equivalent density. This section is going to prove that the plastic beads plume is quantitatively comparable to the one-phase plume with the same buoyancy flux.

Since there is no particle inside it, the dissolved NaCl plume is invisible under the backlight. In order to measure the plume shape, We add some fluorescein into the solution. In addition, the laser is replaced with a violet laser. In response to the violet laser, the fluorescein emits green light, which helps us to measure the plume shape. The average image of dissolved NaCl plume ($I = 0.56\,\mathrm{g\,s^{-1}}$) is shown in Figure 5.17. Although there is no back-light for this NaCl plume, the image is cut specifically in the same size and location of the back-light for comparison with

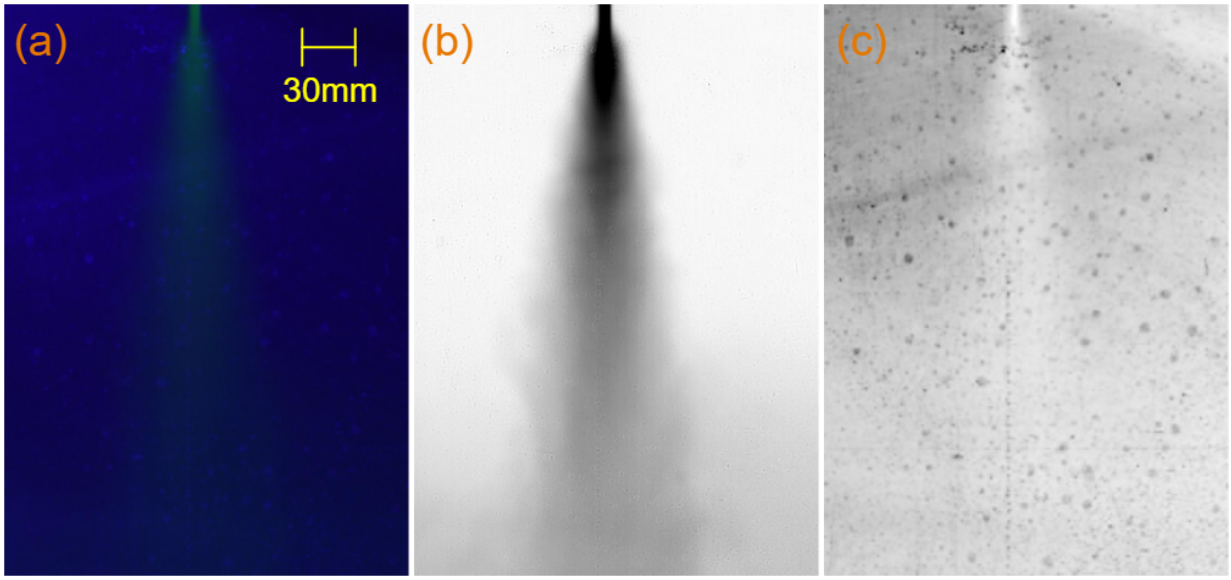

Figure 5.17: Average image for dissolved NaCl plume. Experiment with pump injection, the total injection rate $I = 0.56\,\mathrm{g/s}$. For (b) and (c), the contrast of images is enhanced and the images are reversed for better visualization. (a) Full-colored average raw image under the illumination of a violet laser; (b) The green channel of the average image; (c) The blue channel of the average image.

other particle plumes. Figure 5.17(a) is the full-colored average image. Figure 5.17(b) and (c) show in the grey scale the green and blue channels of the full-colored image. The plume shape is more obvious in the green channel. The plume shape is similar to that of the plastic bead plume with a similar injection rate. The plume shape process is similar to other plume images by using Figure 5.17(b).

For dissolved NaCl plumes, one major benefit is velocity measurement. The velocity inside the plume is measured with PIV without the interference of particles. Figure 5.18 shows the PIV velocity field inside and outside of the plume. To obtain accurate velocity measurements using PIV, it is necessary to have a sufficient displacement of the PIV beads between two neighboring images. However, if the displacement is too large, the PIV beads escape the interrogation windows. The optimum displacement is about one-fourth of the interrogation windows length. For different velocity amplitudes, we use the same image sequence but different measurement frequencies. This led to differences in the velocity field. For velocity inside of plume, the typical

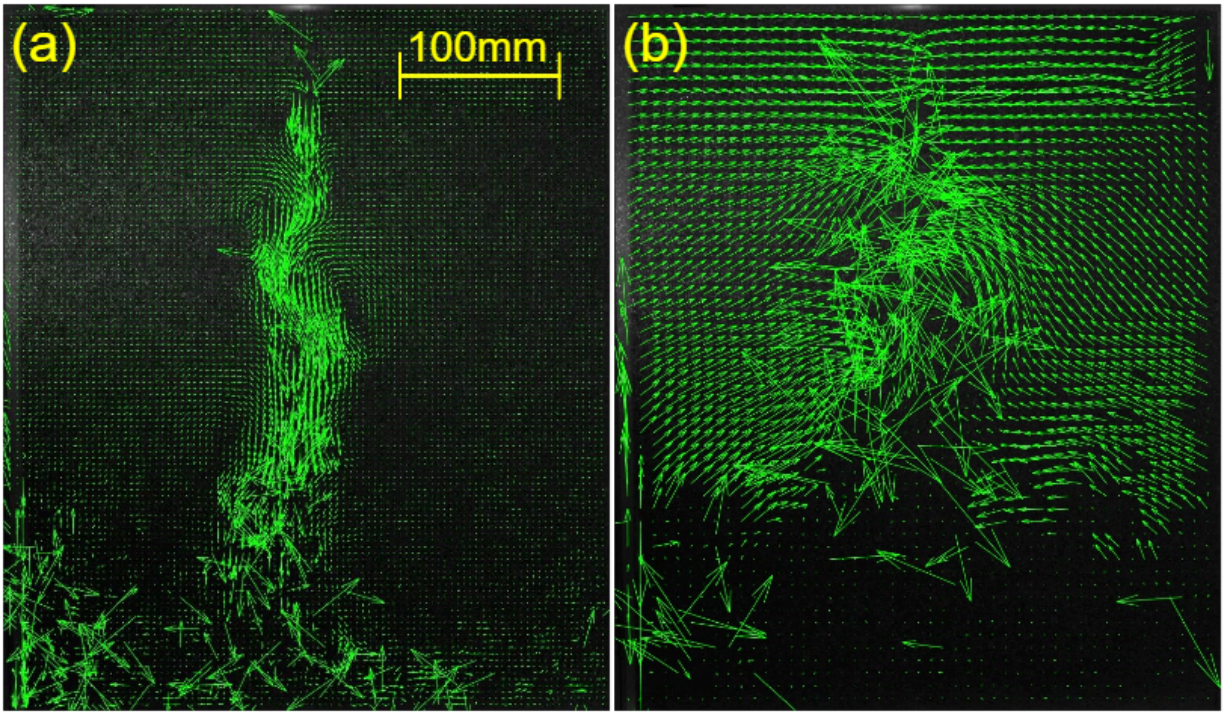

Figure 5.18: PIV velocity field for dissolved NaCl plume. Experiment with pump injection, total injection rate $I = 0.56\,\mathrm{g/s}$. (a) Measurement frequency 10 Hz, focusing on the velocity field inside of the plume; (b) Measure frequency 1 Hz, focusing on the velocity field outside of the plume.

velocity is about 30 mm, referring to about 100 pixels s^{-1}. The measurement frequency is 10 Hz, which ensures that the displacement of PIV beads is 10 pixels between two frames. For the velocity field outside of the plume, The entrainment velocity is only one-tenth of plume vertical velocity. So the measurement frequency for PIV processing is also one-tenth, which is 1 Hz.

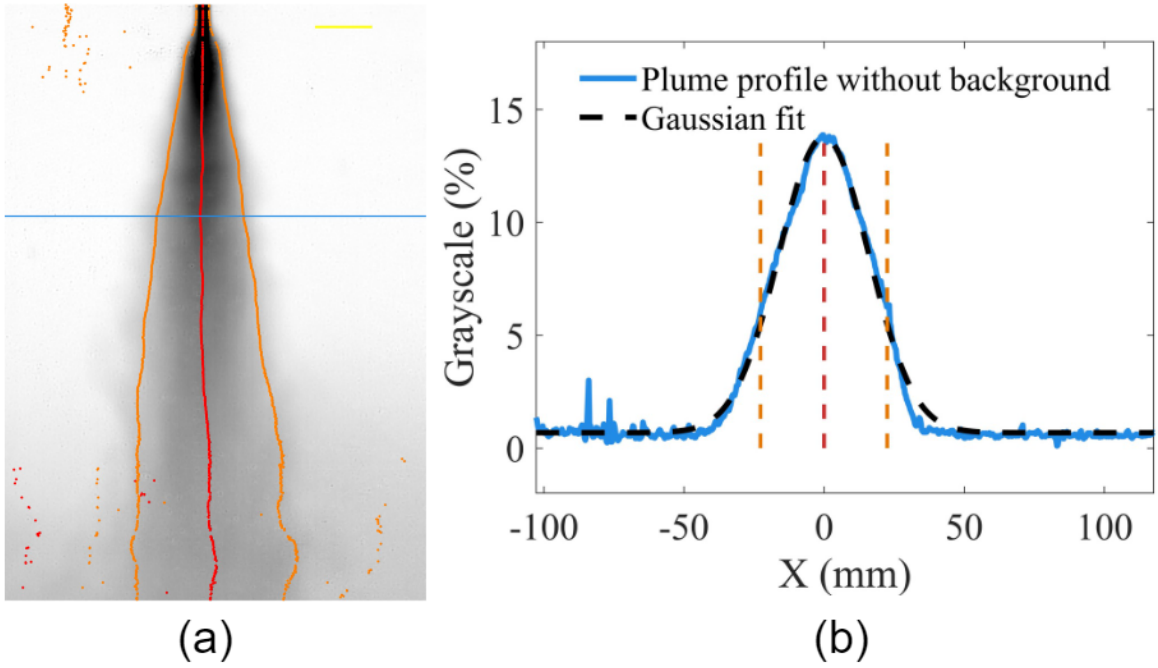

Figure 5.19: Average image intensity profile for dissolved NaCl plume. Experiment with pump injection, the total injection rate $I = 0.56\,g/s$. (a) the green channel of the average image illuminated violet laser when the plume is fully developed. Redline corresponds to the maximal intensity on the horizontal line, i.e. it is the middle line of the plume. The orange line is the plume half-width by fit, shown in (b). The contrast of the image is enhanced and the image is reversed for better visualization; (b) The intensity profile for the blue line is indicated in (a) with Gaussian fit.

Similar to particle plumes, the plume shape for dissolved NaCl plume is measured by fitting with a Gaussian on each horizontal line. Except the image is measured under a violet laser, not back-light. In Figure 5.19, the plume profile (blue line) is well fitted by a Gaussian (black dash line). There is a bit of asymmetry on the right side around 30 mm. This is due to the fact that we have only one violet laser, located on the left, so the laser intensity is reduced after going through the plume. The plume middle line and half-width line by fit are plotted in Figure 5.19(a).

The plume shape is similar to the plastic bead plume (Figure 5.5(a)). For the dissolved NaCl plume, the transition region in the Z direction (the distance between the entrance and the point where the plume is fully developed) is shorter than the plastic bead plume. This phenomenon is shown more clearly in Figure 5.20.

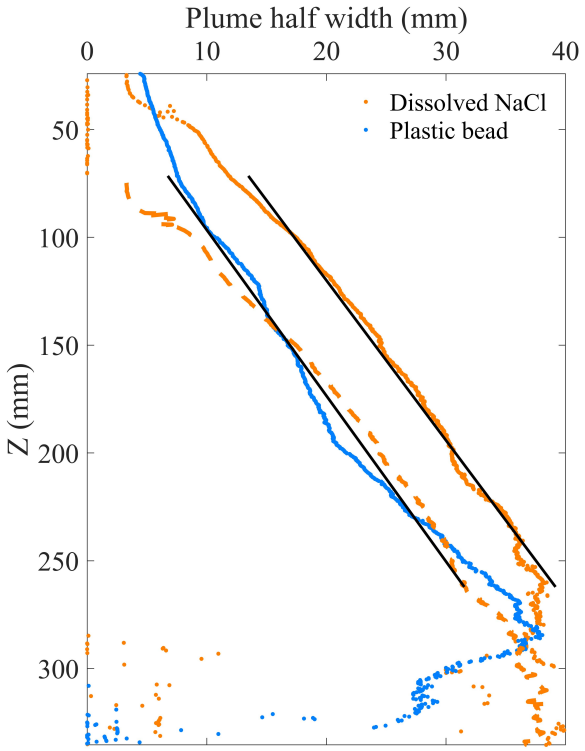

Figure 5.20: Plume half width over Z direction. Orange for dissolved NaCl plume ($I = 0.56\,\mathrm{g/s}$) and blue for plastic beads plume ($I = 0.59\,\mathrm{g/s}$). Black lines are the linear fit for two plumes. The orange dashed line is the curve for dissolved NaCl plume with 50 mm displacement in z direction.

Figure 5.20 compares plume half-width between dissolved NaCl plume and plastic bead plume with a similar injection rate. These two plumes provide a similar amount of buoyancy flux into the tank, and thus for which we expect to have similar plume shapes. The dissolved NaCl plume is wider than the plastic bead plume at the same height. According to the linear fit lines, the two plumes have similar slopes. The orange dash line is the orange line with 50 mm vertical displacement. After this displacement, two half-width lines overlap each other. This illustrates

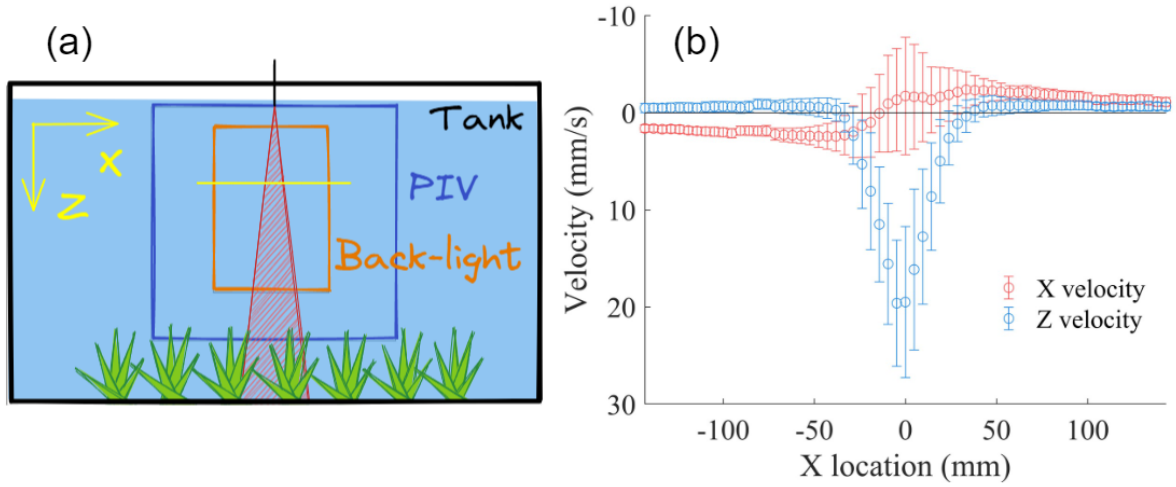

Figure 5.21: Velocity profile over horizontal direction on a certain height for dissolved NaCl plume. Experiment with pump injection, the total injection rate $I = 0.56\,\mathrm{g/s}$. (a) The schematic of measurement. The measure location is indicated with a yellow line. The yellow line is 150 mm below the entrance; (b) Horizontal and vertical velocity profiles along the yellow line of (a), the error bar is the standard deviation.

that the particles in the plume do not influence the shape when the plume is fully developed, but they expand the transition region just below the entrance.

Figure 5.21 shows the velocity profiles for dissolved NaCl plume when it is fully developed. The Z velocity profile (blue) is symmetric, and looks similar to the intensity profile, with a Gaussian shape. Far away from the plume, the z velocity is slightly higher than $0\,\mathrm{mm\,s^{-1}}$, which is about $0.5\,\mathrm{mm\,s^{-1}}$. This is the background velocity due to the raising of the water surface in the tank, which has the same order of magnitude as Equation 3.2. For the X velocity profile, it is asymmetric and has an almost constant value outside plume of about $2.0\,\mathrm{mm\,s^{-1}}$ (Section 4.2). For X velocity inside of the plume, the error bar is very large due to a strong noise inside of the plume. Since the velocity profiles are self-similar, averaging the re-scaled profiles (with plume half width) over the Z direction could be a way to obtain a more precise profile.

The normalized Z velocity profile and intensity profile at the same height are compared in Figure 5.22. Both profiles can nicely be fitted by a fit with Gaussian function, but the half widths are quite different. The velocity profile is narrower than the intensity profile. This difference is

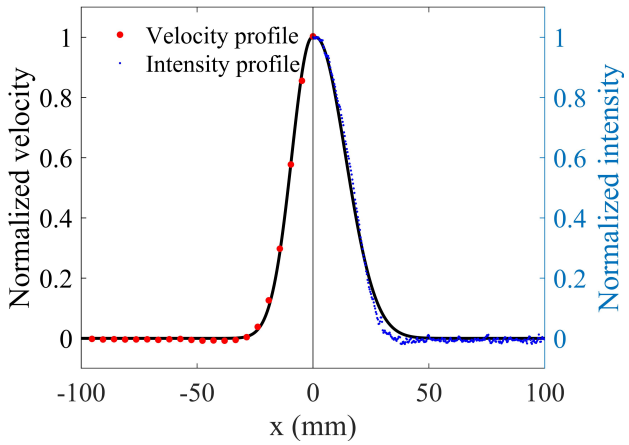

Figure 5.22: Comparison between normalized intensity profile and velocity profile. Experiment for dissolved NaCl plume, pump injection, the total injection rate $I = 0.56\,\mathrm{g/s}$. The red and blue points are normalized Z velocity profile and intensity profile. The black lines are Gaussian fit for each profile.

also observed in many other plume experiments (Richardson and Gary R. Hunt, 2022).

5.4 Comparison with dissolving plume

In this section, we compare the plastic bead plume with two dissolving particle plumes, butyramide and KNO_3. We discuss the influence of particle dissolution on plume shape and velocity field.

5.4.1 Plume shape

Similar to the processing for plastic bead plumes, we average the images illuminated with back-light when the plume is fully developed. After removing the background image, each horizontal line of the image is fitted with a Gaussian function to catch the plume shape, as shown in Figure 5.23(a). Figure 5.23(b) shows the intensity profiles at different heights indicated in Figure 5.23(a) with the same color. In Figure 5.23(c), these profiles are normalized and overlapped with each other. It means that with dissolving particles, the plume is still self-similar. Compared with the plastic bead plume (Figure 5.5), the dissolving plume is much narrower in x direction,

and almost vertical on the side.

Figure 5.24 shows the plume half width and intensity integration as a function of height for three different particles with similar injection rates. For KNO_3 (pink), because the volume concentration is almost half compared with other plumes, the signal is too low to have the plume shape after 150 mm.

For plume half-width, displayed in Figure 5.24(a), before about 140 mm, the three plumes show similar tendency and value, increase with height linearly. Below Z = 140 mm the half-width of the butyramide plume increases with depth, but the slope is smaller than the one of the plastic bead plume, accociated with the dissolving of butyramide due to the entrainment of ambient fluid.

Figure 5.10 showed that the intensity integration is linear with mass flux when the total injection rate is $I < 0.5\,\mathrm{g\,s^{-1}}$. But in Figure 5.24(b), we do not convert the plume intensity integration into mass flux, because the calibration curve in Figure 5.10 is only for plastic bead plume, which is not exactly suitable for Butyramide and KNO_3. This means that comparing the absolute value between different curves is not relevant, but within one curve, we can know how much of the salt has been dissolved.

In Figure 5.24(b), we see that the intensity integration for plastic bead plume is almost constant between 120 mm to 280 mm. For butyramide, intensity integration decreases to half as its maximum, which infers that half of the butyramide particles are dissolved within this 160 mm. For KNO_3, most of the particles are dissolved completely below 200 mm.

5.4.2 Entrainment velocity profile

The PIV setup for butyramide and KNO_3 is the same as for the plastic beads, with a 1 Hz measurement frequency and focusing on the sides a bit away from the plume. In contrast with the cases of non-dissolving plumes, the entrainment velocity for dissolving plumes is not constant along the vertical direction.

Figure 5.25 shows the average velocity profiles for three particle types with similar injection

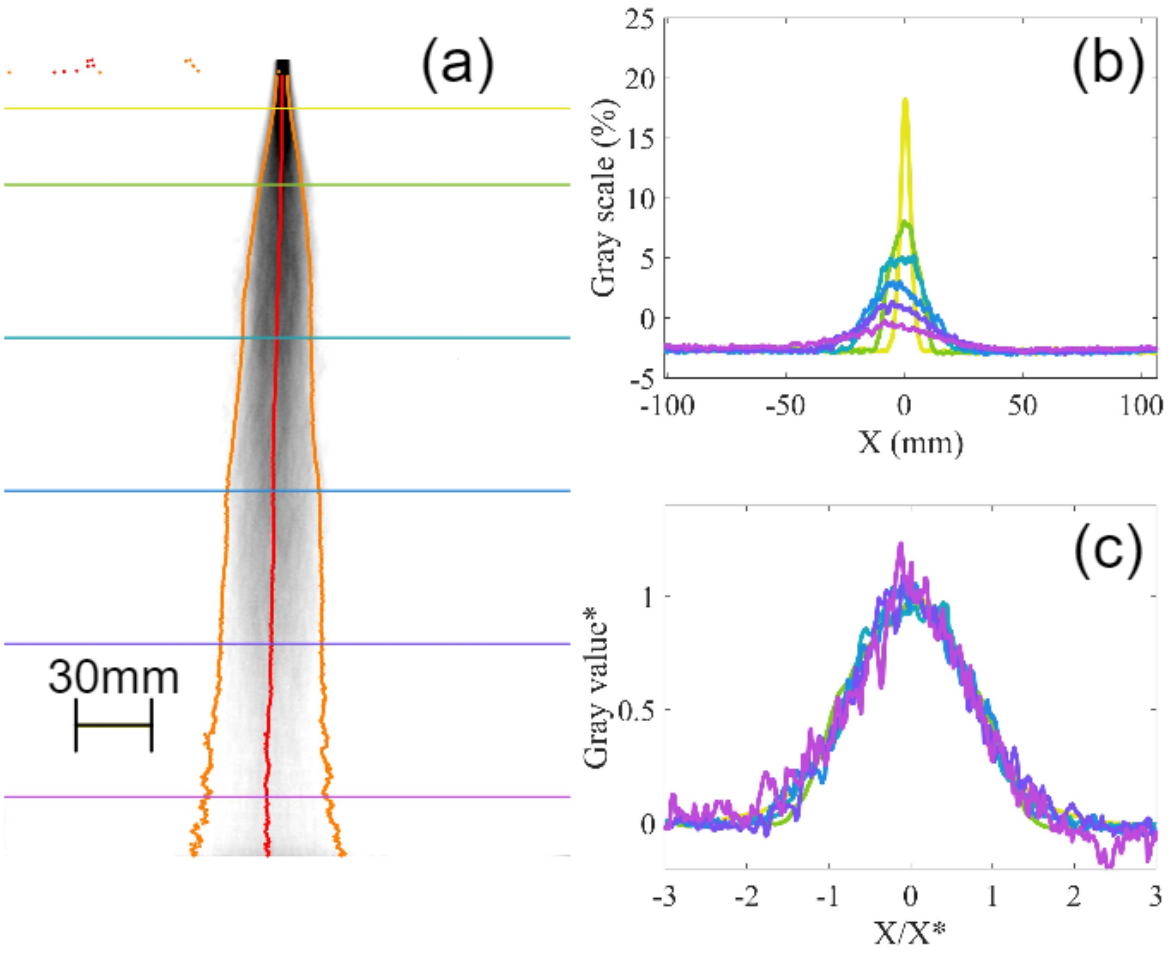

Figure 5.23: Intensity profiles at different heights. Experiment for butyramide, pump injection, the total injection rate $I = 0.53\,\mathrm{g/s}$. (a) Average image illuminated with back-light when the plume is fully developed. Red and orange lines are the plume middle lines and plume half-width lines shown in Figure 5.5; (b) The intensity profiles at different heights; (c) The normalized intensity profiles at different heights.

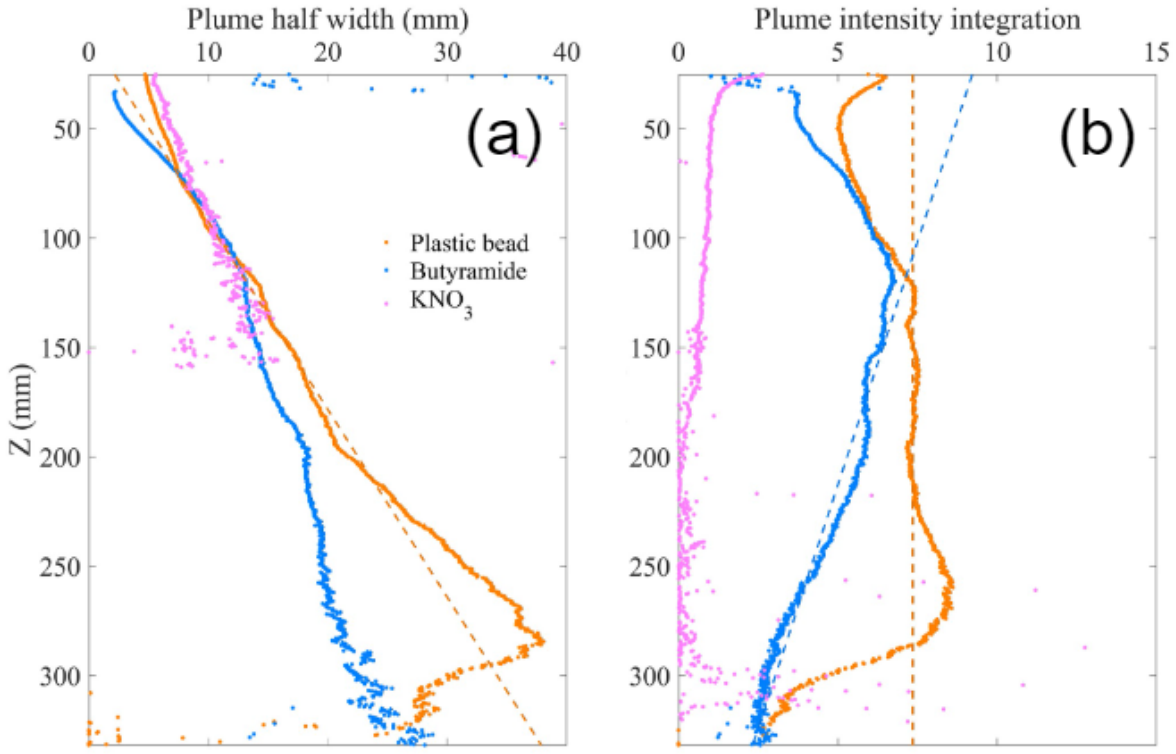

Figure 5.24: Plume shape characteristics change with height for different particles in similar injection rates. Orange line, plastic bead ($I = 0.59\,\mathrm{g/s}$); Blue line, butyramide ($I = 0.53\,\mathrm{g/s}$); Pink line, KNO_3 ($I = 0.56\,\mathrm{g/s}$). (a) Plume half width; (b) Plume intensity integration.

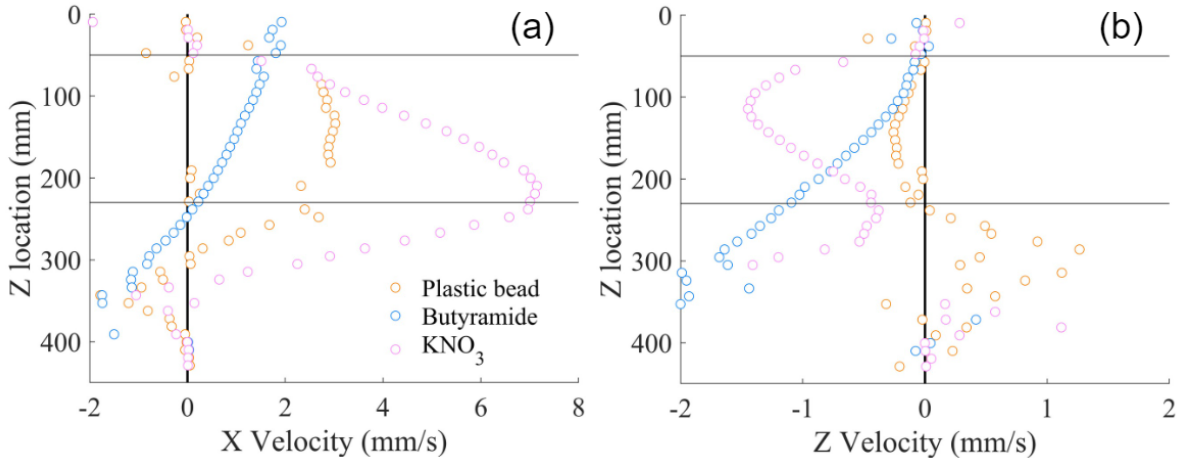

Figure 5.25: The average velocity profile outside of the plume (Figure 5.16(a)) for different particles with similar injection rate. Orange, plastic bead ($I = 0.59\,\mathrm{g/s}$); Blue, butyramide ($I = 0.53\,\mathrm{g/s}$); Pink , KNO_3 ($I = 0.56\,\mathrm{g/s}$). (a) Velocity in x direction; (b) Velocity in z direction.

rates. The measurement location is as same as the yellow line in Figure 5.16(a). For the entrainment velocity (Figure 5.25(a)), the profile for plastic bead plume is almost constant between 80 mm to 200 mm. For butyramide, the x velocity decreases along with height, even becomes negative below 250 mm. For KNO_3, due to the density increase of the ambient water, KNO_3 provides much more buoyancy flux into the tank, which leads to a much higher entrainment velocity around 200 mm and decreases suddenly. We think this is due to the fact that the tank height scale limits the plume development.

For Z velocity in Figure 5.25(b), if the velocity field is in steady state, the Z velocity should be zero at all heights. Since the experiment is done in a tank, the water surface raises during the injection. The Z velocity is negative and much smaller than the vertical velocity, like for plastic bead plume between 0 mm to 240 mm. For butyramide plume, the Z velocity increase along the Z direction. The amplitude of the maximum valve is similar to the X velocity. For KNO_3 plume, the Z velocity varies in the Z direction.

5.5 Conclusion

In Chapter 5 we discuss the plume experiment with four kinds of injected solutions and two kinds of injection methods (Figure 5.1). Three of the injection solutions are mixtures of particles and their corresponding saturated solutions (plastic beads with water). The last one is a one-phase dissolved NaCl solution. The measurement results come from two parts, the particle localized concentration measurement with back-light, and the velocity field measurement with PIV.

The particle localized concentration is measured by using the feature that with suitable exposed time, the particle concentration is proportional to the decreasing of back-light intensity. After calibration with plastic bead plumes, we have the linear relationship between total injection rate ($I = 0 \sim 0.5\,\mathrm{g\,s^{-1}}$) and integration of intensity over x direction (Figure 5.10). The plume profiles in the fully developed region are self-similar to Gaussian-like profiles. For measurement of plume shape during steady state, after removing the background for the average image, the concentration profile on each height can be fitted with a Gaussian, from which we have the plume shape parameters, plume half-width, middle line location, and local concentration, etc. With the slope of the plume half-width line, we measured the entrainment coefficient α for the plastic bead plume (Figure 5.8). The measurement result is scattered between 0.07 and 0.15, and becomes a bit higher for large injection rates. The average $\alpha = 0.11 \pm 0.02$ agrees well with the measurement of one-phase plumes.

We compared the plastic bead plume with a one-phase dissolved NaCl plume, which has the same equivalent density. The slope of the plume half-width curve is similar, but there is a vertical displacement for about 50 mm. The plastic bead plume needs more distance to develop compared to the dissolved NaCl plume.

For plumes with soluble particles, the plume half-width is almost vertical on the side due to the entrainment and dissolving, which is much narrower than a plastic bead plume. The plume concentration profiles are still self-similar and Gaussian-like in the fully developed regions. The

plume particle flux decreases linearly along the Z direction.

For the velocity measurement, the entrainment velocity profile on the side of the plastic bead plume is constant over height (Figure 5.16) and agrees well with theoretical predictions (Figure 5.14). The velocity profile of the soluble particle plume is rather different. For butyramide, since the dissolution of particles does not change the density of the surrounding fluid, the entrainment velocity decreases along the z direction and even becomes negative below a certain height. On the contrary, KNO_3 enhances the entrainment a lot by increasing the ambient fluid density after dissolving. These results on velocity vertical profiles need to be consolidated.

In the future, it will be interesting to compare the butyramide plume results with the observations of real localized rains. As a step further, clouds could be mimicked by releasing an over-saturated butyramide solution at the bottom of a tank filled with quiescent water.

6 | Conclusion

This thesis was motivated by the modeling of rain and clouds, which are an essential part of the Earth climate. I mainly investigated plumes of soluble particles in water through experiments. This configuration comes from the similarities between the partial evaporation of rain droplets and the dissolution of the salt particles in water.

To study the dissolution dynamics at the scale of single-particle, we have designed and built a lifting platform system, which can track in real time a single salt particle in quiescent water. This system identifies the location of a particle with a camera fixed on the platform and adjusts the height of the platform automatically to ensure the particle is always in the image. With this setup, we have a fairly large magnification of the particle to see the detail of the particle dissolving, and we can track the particle for a long time until it dissolves completely.

The system has been verified with steady sedimentation velocity of plastic beads. For soluble spherical particles, with an advection-diffusion model at low Reynolds number and high Péclet number, we have shown that the particle diameter reduction rate $\dot{d}$ is a constant value. We could also derive the vertical location of the dissolving particle as a function of time, which is a 3rd order polynomial curve.

Butyramide is used for single-particle dissolving experiments. For rather spherical particles, we compare the particle initial diameter d_0 and diameter reduction rate $\dot{d}$ with two different measurement methods. The order of magnitude of the measured value of $\dot{d}$ agrees with the theoretical estimation. A further step of this experiment would be to select more efficiently particles with a

spherical shape, which can improve the reproducibility of the experiments and the comparison to the theoretical predictions.

The widely recognized MTT model for plumes B R Morton et al., 1956 has been adapted for 2D particle plumes. We derived the general scaling behaviors of the plume based on the top hat profile. In order to avoid the simple entrainment assumption at the plume side, we used the Reynolds-average Navier-Stokes equation with a mixing length approach for momentum and buoyancy mixing. The velocity and buoyancy profiles are solved analytically when Schmidt number is equal to 1. In the case of a Gaussian velocity profile, that of buoyancy is found to be not exactly Gaussian but close. Also, we could relate the entrainment coefficient to the mixing laws. These calculations must be further developed to account for dissolution.

An experimental setup to investigate the continuous sedimentation of soluble particles inside quiescent water is designed and built. The particles are pre-mixed with the corresponding saturated solution and injected into the tank with a pump or gravity, which forms a particle plume. Some artificial grasses are placed at the bottom of the tank to slow down the plume going through them. Two lasers are placed on the sides of the tank for PIV measurement. A constant backlight is placed behind the tank for plume concentration measurements.

Four types of solutions are used. Three of them are the mixture of particles and the corresponding saturated solution, plastic bead, butyramide, and a salt KNO_3 (the plastic beads are mixed with water). The plastic bead plume is the reference case without dissolution for the particle plume, and also serves as setup validation. The density of the saturated solution of butyramide is close to water, which means that butyramide does not change the surrounding density when dissolving, unlike usual salts, such as KNO_3. The last studied case is a homogeneous dissolved NaCl solution, which has the same equivalent density as the plastic bead solution. The NaCl solution is used as a control to compare the common buoyancy plume with the particle plume, and to allow for PIV measurement within the plume.

A major difficulty for the experiment is to reduce the air bubbles trapped between the parti-

cles, because the density of the particles is close to the one of water, air bubbles on the particle can modify their effective density significantly. We use a vacuum pump to remove the bubbles in the mixed solution, and the whole preparation process has been done within CO_2 surrounding and CO_2 dissolved well in water, which ensures that there is no air bubble in the mixed solution.

The particle concentration field is measured using the feature that with suitable exposure time, the particle location concentration is proportional to the decrease of back-light intensity. With corresponding calibration using plastic bead plumes, we have a linear relationship between total injection rate ($I = 0 \sim 0.5\,\mathrm{g\,s^{-1}}$) and integration of intensity over x direction.

The plume profiles in the fully developed region are self-similar and Gaussian-like. For measurement of plume shape during steady state, after removing the background for the average image, the concentration profile on each height is fitted with a Gaussian function, from which we have the plume shape parameters, plume half-width, middle line location, and local concentration, etc. With the slope of the plume half-width line along Z, we measured the entrainment coefficient α for the plastic bead plume (Figure 5.8). The average $\alpha = 0.11 \pm 0.02$, agrees well with the measurement of one-phase buoyancy plumes.

We compared the plastic bead plume result with the one-phase dissolved NaCl plume, which has the same equivalent density. The slope of the plume half-width curve is similar, but there is an offset of the average plume shape for about 50 mm along the Z direction. The plastic bead plume needs more distance to expand and develop compared to the NaCl plume.

In the case of soluble particles, the plume half-width is almost vertical on the side due to the entrainment and dissolving, and is much narrower than the plastic bead plume. The plume concentration profiles are still self-similar and Gaussian-like in the fully developed region. The plume particle flux for buoyancy plume decreases linearly along z direction.

The entrainment velocity profile on the side of the plastic bead plume is constant over height (Figure 5.16) which agrees with theoretical predictions (Figure 5.14). The velocity profile of the soluble particle plume is very different. For butyramide, since the dissolving of butyramide does

not change the density of the surrounding fluid, the entrainment velocity decreases along z direction, and even becomes negative below a certain height. On the contrary, KNO_3 enhances the entrainment a lot by increasing the plume density. In the future, it will be interesting to compare the butyramide plume results with the observations of real localized rains. As a step further, clouds could be mimicked by releasing an over-saturated butyramide solution at the bottom of a tank filled with quiescent water.

Bibliography

Alahyari, Abbas A. and Ellen K. Longmire (Mar. 1997). "Concentration Measurements in Experimental Microbursts". In: *AIAA Journal* 35.3, pp. 569–571. ISSN: 0001-1452. DOI: 10.2514/2.136.

Arias, P.A. et al. (2021). "Technical Summary". In: ed. by V. Masson-Delmotte et al., 33144. DOI: 10.1017/9781009157896.002.

Baines, W. D. and J. S. Turner (June 1969). "Turbulent buoyant convection from a source in a confined region". In: *Journal of Fluid Mechanics* 37.1, pp. 51–80. ISSN: 0022-1120. DOI: 10.1017/S0022112069000413.

Beals, Matthew J et al. (Oct. 2015). "Holographic measurements of inhomogeneous cloud mixing at the centimeter scale". In: *Science* 350.6256, pp. 87–90. ISSN: 0036-8075. DOI: 10.1126/science.aab0751.

Berhanu, M. et al. (Mar. 2007). "Magnetic field reversals in an experimental turbulent dynamo". In: *Europhysics Letters (EPL)* 77.5, p. 59001. ISSN: 0295-5075. DOI: 10.1209/0295-5075/77/59001.

Bhaganagar, Kiran and Sudheer R. Bhimireddy (Oct. 2020). "Numerical investigation of starting turbulent buoyant plumes released in neutral atmosphere". In: *Journal of Fluid Mechanics* 900, A32. ISSN: 0022-1120. DOI: 10.1017/jfm.2020.474.

Bordoloi, Ankur D. et al. (Aug. 2020). "Turbulence statistics in a negatively buoyant multiphase plume". In: *Journal of Fluid Mechanics* 896, A19. ISSN: 0022-1120. DOI: 10.1017/jfm.2020.326.

Bretherton, Christopher S. and Peter N. Blossey (Mar. 2014). "Low cloud reduction in a greenhouse-warmed climate: Results from Lagrangian les of a subtropical marine cloudiness transition". In: *Journal of Advances in Modeling Earth Systems* 6.1, pp. 91–114. ISSN: 19422466. DOI: 10.1002/2013MS000250.

Brient, Florent and Sandrine Bony (May 2013). "Interpretation of the positive low-cloud feedback predicted by a climate model under global warming". In: *Climate Dynamics* 40.9-10, pp. 2415–2431. ISSN: 0930-7575. DOI: 10.1007/s00382-011-1279-7.

Burridge, H.C., J.L. Partridge, and P.F. Linden (Aug. 2016). "The Fluxes and Behaviour of Plumes Inferred from Measurements of Coherent Structures within Images of the Bulk Flow". In: *Atmosphere-Ocean* 54.4, pp. 403–417. ISSN: 0705-5900. DOI: 10.1080/07055900.2016.1175337.

Buttlar, Jannis von et al. (Mar. 2018). "Impacts of droughts and extreme-temperature events on gross primary production and ecosystem respiration: a systematic assessment across ecosystems and climate zones". In: *Biogeosciences* 15.5, pp. 1293–1318. ISSN: 1726-4189. DOI: 10.5194/bg-15-1293-2018.

Carazzo, G., E. Kaminski, and S. Tait (2008). "On the rise of turbulent plumes: Quantitative effects of variable entrainment for submarine hydrothermal vents, terrestrial and extra terrestrial explosive volcanism". In: *Journal of Geophysical Research: Solid Earth* 113.9, pp. 1–19. ISSN: 21699356. DOI: 10.1029/2007JB005458.

Caulfield, Colm-Cille P. and Andrew W. Woods (Aug. 1995). "Plumes with non-monotonic mixing behaviour". In: *Geophysical & Astrophysical Fluid Dynamics* 79.1-4, pp. 173–199. ISSN: 0309-1929. DOI: 10.1080/03091929508228996.

Charru, François, Bruno Andreotti, and Philippe Claudin (Jan. 2013). "Sand Ripples and Dunes". In: *Annual Review of Fluid Mechanics* 45.1, pp. 469–493. ISSN: 0066-4189. DOI: 10.1146/annurev-fluid-011212-140806.

Clement, Amy C., Robert Burgman, and Joel R Norris (July 2009). "Observational and Model Evidence for Positive Low-Level Cloud Feedback". In: *Science* 325.5939, pp. 460–464. ISSN: 0036-8075. DOI: 10.1126/science.1171255.

Dai, Z., L.-K. Tseng, and G. M. Faeth (May 1994). "Structure of Round, Fully Developed, Buoyant Turbulent Plumes". In: *Journal of Heat Transfer* 116.2, pp. 409–417. ISSN: 0022-1481. DOI: 10.1115/1.2911413.

Davaille, Anne and Judith Vatteville (July 2005). "On the transient nature of mantle plumes". In: *Geophysical Research Letters* 32.14, n/a–n/a. ISSN: 00948276. DOI: 10.1029/2005GL023029.

Deike, Luc et al. (Jan. 2018). "Dynamics of jets produced by bursting bubbles". In: *Physical Review Fluids* 3.1, p. 013603. ISSN: 2469-990X. DOI: 10.1103/PhysRevFluids.3.013603.

Dutta, Urmi et al. (July 2014). "Ascent modes of jets and plumes in a stationary fluid of contrasting viscosity". In: *International Journal of Multiphase Flow* 63, pp. 1–10. ISSN: 03019322. DOI: 10.1016/j.ijmultiphaseflow.2014.02.007.

Emerson, Steven et al. (1999). "Accurate measurement of O2, N2, and Ar gases in water and the solubility of N2". In: *Marine Chemistry* 64.4, pp. 337–347.

Enick, Robert M and Scott M Klara (1990). "CO2 solubility in water and brine under reservoir conditions". In: *Chemical Engineering Communications* 90.1, pp. 23–33. DOI: 10.1016/S0304-4203(98)00090-5.

Ezzamel, A., P. Salizzoni, and G. R. Hunt (Feb. 2015). "Dynamical variability of axisymmetric buoyant plumes". In: *Journal of Fluid Mechanics* 765.2015, pp. 576–611. ISSN: 0022-1120. DOI: 10.1017/jfm.2014.694.

Fischer, HUGO B. et al. (1979). "Turbulent Jets and Plumes". In: *Mixing in Inland and Coastal Waters*. Vol. 14 , M. Va. Elsevier, pp. 315–389. ISBN: 0 8243 0714 3. DOI: 10.1016/B978-0-08-051177-1.50013-1.

Fourel, Loïc et al. (2017). "The Earth's mantle in a microwave oven: thermal convection driven by a heterogeneous distribution of heat sources". In: *Experiments in Fluids* 58.8. ISSN: 07234864. DOI: 10.1007/s00348-017-2381-3.

Frame, David J. et al. (Sept. 2020). "Climate change attribution and the economic costs of extreme weather events: a study on damages from extreme rainfall and drought". In: *Climatic Change* 162.2, pp. 781–797. ISSN: 0165-0009. DOI: 10.1007/s10584-020-02729-y.

Gualtieri, Carlo et al. (2017). "On the values for the turbulent schmidt number in environmental flows". In: *Fluids* 2.2. ISSN: 23115521. DOI: 10.3390/fluids2020017.

Guillaume, Carazzo, Kaminski Edouard, and Tait Stephen (Jan. 2006). "The route to self-similarity in turbulent jets and plumes". In: *Journal of Fluid Mechanics* 547.-1, p. 137. ISSN: 0022-1120. DOI: 10.1017/S002211200500683X.

Guyon, Etienne et al. (2015). *Physical hydrodynamics*. Oxford University Press.

Hartmann, Dennis L. and Kristin Larson (Oct. 2002). "An important constraint on tropical cloud - climate feedback". In: *Geophysical Research Letters* 29.20, pp. 12–1–12–4. ISSN: 00948276. DOI: 10.1029/2002GL015835.

Hosannah, N. et al. (June 2019). "Impacts of Local Convective Processes on Rain on the Caribbean Island of Puerto Rico". In: *Journal of Geophysical Research: Atmospheres* 124.12, pp. 6009–6026. ISSN: 2169-897X. DOI: 10.1029/2018JD029825.

Hunt, G. R. and H. C. Burridge (2015). "Fountains in industry and nature". In: *Annual Review of Fluid Mechanics* 47, pp. 195–220. ISSN: 00664189. DOI: 10.1146/annurev-fluid-010313-141311.

Kotsovinos, Nikolas Evangelos (1975). *A study of the entrainment and turbulence in a plane buoyant jet*. California Institute of Technology.

Levich, Veniamin Grigorevich (1962). "Physicochemical hydrodynamics". In.

Li, Chao et al. (June 2019). "Larger Increases in More Extreme Local Precipitation Events as Climate Warms". In: *Geophysical Research Letters* 46.12, pp. 6885–6891. ISSN: 0094-8276. DOI: 10.1029/2019GL082908.

Lopez-Cantu, Tania, Andreas F. Prein, and Constantine Samaras (May 2020). "Uncertainties in Future U.S. Extreme Precipitation From Downscaled Climate Projections". In: *Geophysical Research Letters* 47.9. ISSN: 0094-8276. DOI: 10.1029/2019GL086797.

Magnaudet, Jacques and Matthieu J. Mercier (Jan. 2020). "Particles, Drops, and Bubbles Moving Across Sharp Interfaces and Stratified Layers". In: *Annual Review of Fluid Mechanics* 52.1, pp. 61–91. ISSN: 0066-4189. DOI: 10.1146/annurev-fluid-010719-060139.

Manabe, Syukuro and Richard T. Wetherald (May 1967). "Thermal Equilibrium of the Atmosphere with a Given Distribution of Relative Humidity". In: *Journal of the Atmospheric Sciences* 24.3, pp. 241–259. ISSN: 0022-4928. DOI: 10.1175/1520-0469(1967)024<0241:TEOTAW>2.0.CO;2.

Mason, B. J. and J. B. Andrews (July 1960). "Drop-size distributions from various types of rain". In: *Quarterly Journal of the Royal Meteorological Society* 86.369, pp. 346–353. ISSN: 00359009. DOI: 10.1002/qj.49708636906.

McConnochie, Craig D., Claudia Cenedese, and Jim N. McElwaine (Dec. 2021). "Entrainment into particle-laden turbulent plumes". In: *Physical Review Fluids* 6.12, p. 123502. ISSN: 2469-990X. DOI: 10.1103/PhysRevFluids.6.123502.

Mellado, Juan Pedro (2017). "Cloud-Top Entrainment in Stratocumulus Clouds". In: *Annual Review of Fluid Mechanics* 49.June, pp. 145–169. ISSN: 00664189. DOI: 10.1146/annurev-fluid-010816-060231.

Minta, Akwasi, Joseph PY Kao, and Roger Y Tsien (1989). "Fluorescent indicators for cytosolic calcium based on rhodamine and fluorescein chromophores". In: *Journal of Biological Chemistry* 264.14, pp. 8171–8178. DOI: 10.1016/S0021-9258(18)83165-9.

Mitchell, Daniel et al. (July 2016). "Attributing human mortality during extreme heat waves to anthropogenic climate change". In: *Environmental Research Letters* 11.7, p. 074006. ISSN: 1748-9326. DOI: 10.1088/1748-9326/11/7/074006.

Morton, B R et al. (1956). "Turbulent gravitational convection from maintained and instantaneous sources". In: *Proceedings of the Royal Society of London. Series A. Mathematical and Physical Sciences* 234.1196, pp. 1–23. ISSN: 0080-4630. DOI: 10.1098/rspa.1956.0011.

Morton, B. R. (Oct. 1971). "The choice of conservation equations for plume models". In: *Journal of Geophysical Research* 76.30, pp. 7409–7416. ISSN: 01480227. DOI: 10.1029/JC076i030p07409.

Muller, Caroline et al. (2021). "Spontaneous Aggregation of Convective Storms". In: *Annual Review of Fluid Mechanics* 54, pp. 133–157. ISSN: 00664189. DOI: 10.1146/annurev-fluid-022421-011319.

Narasimha, Roddam et al. (Sept. 2011). "Laboratory simulations show diabatic heating drives cumulus-cloud evolution and entrainment". In: *Proceedings of the National Academy of Sciences* 108.39, pp. 16164–16169. ISSN: 0027-8424. DOI: 10.1073/pnas.1112281108.

Needham, Michael R. and David A. Randall (July 2021). "Linking Atmospheric Cloud Radiative Effects and Tropical Precipitation". In: *Geophysical Research Letters* 48.14, pp. 1–9. ISSN: 0094-8276. DOI: 10.1029/2021GL094004.

Norris, Joel R. et al. (Aug. 2016). "Evidence for climate change in the satellite cloud record". In: *Nature* 536.7614, pp. 72–75. ISSN: 0028-0836. DOI: 10.1038/nature18273.

Oehmke, Theresa et al. (Jan. 2021). "Mass Transfer from Non-Spherical Particles in Turbulence". In: *APS Division of Fluid Dynamics Meeting Abstracts*. APS Meeting Abstracts, M27.004, p. M27.004.

Paillat, S. and E. Kaminski (Sept. 2014a). "Entrainment in plane turbulent pure plumes". In: *Journal of Fluid Mechanics* 755, R2. ISSN: 0022-1120. DOI: 10.1017/jfm.2014.424.

— (Apr. 2014b). "Second-order model of entrainment in planar turbulent jets at low Reynolds number". In: *Physics of Fluids* 26.4, p. 045110. ISSN: 1070-6631. DOI: 10.1063/1.4871521.

Parker, D. A. et al. (Jan. 2020). "A comparison of entrainment in turbulent line plumes adjacent to and distant from a vertical wall". In: *Journal of Fluid Mechanics* 882, A4. ISSN: 0022-1120. DOI: 10.1017/jfm.2019.790.

Philippe, Pierre et al. (May 2005). "Penetration of a negatively buoyant jet in a miscible liquid". In: *Physics of Fluids* 17.5, p. 053601. ISSN: 1070-6631. DOI: 10.1063/1.1907735.

Ramaprian, B. R. and M. S. Chandrasekhara (Mar. 1989). "Measurements in Vertical Plane Turbulent Plumes". In: *Journal of Fluids Engineering* 111.1, pp. 69–77. ISSN: 0098-2202. DOI: 10.1115/1.3243602.

Richardson, James and Gary R. Hunt (2022). "What is the entrainment coefficient of a pure turbulent line plume?" In: *Journal of Fluid Mechanics* 934, pp. 1–34. ISSN: 14697645. DOI: 10.1017/jfm.2021.1070.

Rieck, Malte, Louise Nuijens, and Bjorn Stevens (Aug. 2012). "Marine Boundary Layer Cloud Feedbacks in a Constant Relative Humidity Atmosphere". In: *Journal of the Atmospheric Sciences* 69.8, pp. 2538–2550. ISSN: 0022-4928. DOI: 10.1175/JAS-D-11-0203.1.

Romero, Carmen M. and María E. González (June 2010). "Solubility of Acetamide, Propionamide, and Butyramide in Water at Temperatures between (278.15 and 333.15) K". In: *Journal of Chemical & Engineering Data* 55.6, pp. 2326–2327. ISSN: 0021-9568. DOI: 10.1021/je9007475.

Rouse, Hunter, C. S. Yih, and H. W. Humphreys (Jan. 1952). "Gravitational Convection from a Boundary Source". In: *Tellus* 4.3, pp. 201–210. ISSN: 0040-2826. DOI: 10.3402/tellusa.v4i3.8688.

Rowland, Darren (2021). *Advanced Thermodynamics*.

Sayler, Bentley J. and Robert E. Breidenthal (Apr. 1998). "Laboratory simulations of radiatively induced entrainment in stratiform clouds". In: *Journal of Geophysical Research: Atmospheres* 103.D8, pp. 8827–8837. ISSN: 01480227. DOI: 10.1029/98JD00344.

Scase, M. M. et al. (2007). "Local implications for self-similar turbulent plume models". In: *Journal of Fluid Mechanics* 575, pp. 257–265. ISSN: 00221120. DOI: 10.1017/S0022112007004740.

Schiermeier, Quirin (Apr. 2015). "Climatologists to physicists: your planet needs you". In: *Nature* 520.7546, pp. 140–141. ISSN: 0028-0836. DOI: 10.1038/520140a.

Semin, B. et al. (Sept. 2018). "Nonlinear saturation of the large scale flow in a laboratory model of the quasibiennial oscillation". In: *Physical Review Letters* 121.13, p. 134502. ISSN: 0031-9007. DOI: 10.1103/PhysRevLett.121.134502.

Sharp, D. H. (1984). "An overview of Rayleigh-Taylor instability". In: *Physica D: Nonlinear Phenomena* 12.1-3, pp. 3–18. ISSN: 01672789. DOI: 10.1016/0167-2789(84)90510-4.

Siebert, H. et al. (2015). "High-resolution measurement of cloud microphysics and turbulence at a mountaintop station". In: *Atmospheric Measurement Techniques* 8.8, pp. 3219–3228. ISSN: 18678548. DOI: 10.5194/amt-8-3219-2015.

Smalley, Kevin M. and Anita D. Rapp (May 2021). "The impact of rain rate, raining patch size, and spacing on southeastern Pacific cloud fraction transitions". In: *Environmental Research Communications* 3.5, p. 051001. ISSN: 2515-7620. DOI: 10.1088/2515-7620/abf9ad.

Stevens, Bjorn and Sandrine Bony (June 2013). "Water in the atmosphere". In: *Physics Today* 66.6, pp. 29–34. ISSN: 0031-9228. DOI: 10.1063/PT.3.2009.

Sutherland, B.R. et al. (Oct. 2021). "Plumes in rotating fluid and their transformation into tornados". In: *Journal of Fluid Mechanics* 924, A15. ISSN: 0022-1120. DOI: 10.1017/jfm.2021.618.

Suzuki, Kentaroh, Graeme L. Stephens, and Matthew D. Lebsock (Jan. 2013). "Aerosol effect on the warm rain formation process: Satellite observations and modeling". In: *Journal of Geophysical Research: Atmospheres* 118.1, pp. 170–184. ISSN: 2169897X. DOI: 10.1002/jgrd.50043.

Suzuki, Yujiro J. (2005). "A numerical study of turbulent mixing in eruption clouds using a three-dimensional fluid dynamics model". In: *Journal of Geophysical Research* 110.B8, B08201. ISSN: 0148-0227. DOI: 10.1029/2004JB003460.

ToolBox, Engineering (2003). *Water - Density, Specific Weight and Thermal Expansion Coefficients.*

Turner, J S (Dec. 1986). “Turbulent entrainment: the development of the entrainment assumption, and its application to geophysical flows”. In: *Journal of Fluid Mechanics* 173, pp. 431–471. ISSN: 0022-1120. DOI: 10.1017/S0022112086001222.

Weart, Spencer (Feb. 2013). “Rise of interdisciplinary research on climate”. In: *Proceedings of the National Academy of Sciences* 110.supplement_1, pp. 3657–3664. ISSN: 0027-8424. DOI: 10.1073/pnas.1107482109.

West, Harry, Nevil Quinn, and Michael Horswell (2019). “Remote sensing for drought monitoring & impact assessment: Progress, past challenges and future opportunities”. In: *Remote Sensing of Environment* 232.November 2018, p. 111291. ISSN: 00344257. DOI: 10.1016/j.rse.2019.111291.

Winkelmann, Jochen (2018). “Diffusion coefficient of butyramide in water”. In: *Diffusion in Gases, Liquids and Electrolytes*. Springer, pp. 567–567.

Wood, Robert (Aug. 2012). “Stratocumulus Clouds”. In: *Monthly Weather Review* 140.8, pp. 2373–2423. ISSN: 0027-0644. DOI: 10.1175/MWR-D-11-00121.1.

Yu, Shuang et al. (Jan. 2019). “Loss of work productivity in a warming world: Differences between developed and developing countries”. In: *Journal of Cleaner Production* 208.9, pp. 1219–1225. ISSN: 09596526. DOI: 10.1016/j.jclepro.2018.10.067.

Zelinka, Mark D., Kevin M. Grise, et al. (Oct. 2018). “Drivers of the Low-Cloud Response to Poleward Jet Shifts in the North Pacific in Observations and Models”. In: *Journal of Climate* 31.19, pp. 7925–7947. ISSN: 0894-8755. DOI: 10.1175/JCLI-D-18-0114.1.

Zelinka, Mark D., David A. Randall, et al. (Oct. 2017). “Clearing clouds of uncertainty”. In: *Nature Climate Change* 7.10, pp. 674–678. ISSN: 1758-678X. DOI: 10.1038/nclimate3402.

Zhao, Ming (Mar. 2014). “An Investigation of the Connections among Convection, Clouds, and Climate Sensitivity in a Global Climate Model”. In: *Journal of Climate* 27.5, pp. 1845–1862. ISSN: 0894-8755. DOI: 10.1175/JCLI-D-13-00145.1.